BIOSENSING TECHNIQUES IN SURFACE PLASMON RESONANCE MICROCHIPS: CHEMICAL SIGNAL PROCESSING FOR ANALYTE BINDING

by

Tridib Ghosh

A dissertation submitted to the faculty of
The University of Utah
in partial fulfillment of the requirements for the degree of

Doctor of Philosophy

Department of Bioengineering

The University of Utah

August 2014

The University of Utah Graduate School

STATEMENT OF DISSERTATION APPROVAL

The following faculty members served as the supervisory committee chair and members for the dissertation of________________Tridib Ghosh__________________. Dates at right indicate the members' approval of the dissertation.

_________Carlos Mastrangelo_______________, Chair __04/21/2014_____
Date Approved

_________Vladimir Hlady__________________, Member __04/24/2014_____
Date Approved

_________ Richard Rabbit__________________, Member __04/25/2014_____
Date Approved

_________James N. Herron________________, Member __04/25/2014_____
Date Approved

_________Bruce K. Gale __________________, Member __04/25/2014_____
Date Approved

The dissertation has also been approved by_________Patrick Tresco____________ Chair of the Department/School/College of___________Bioengineering____________ and by David B. Kieda, Dean of The Graduate School.

ABSTRACT

A majority of the functions in biological systems are mediated by specific interactions of cellular proteins. Such interactions also involve other biomolecules like antibodies, RNA and DNA, small molecules sometimes referred to as drugs, etc. A detailed understanding of functional proteomics necessitates the need for detection and quantification of such specific biochemical reactions with greater speed and precision. The primary biosensing technology that is employed for detecting these biological interactions optically and with good sensitivity and reproducibility is based on Surface Plasmon Resonance (SPR).

In this work, we aim at utilization of chemical signal processing techniques in microfluidic chips to produce SPR measurements with higher signal-to-noise ratio (SNR), shorter measurement times, and lower reagent volumes than those of conventional SPR systems like BIAcore, ProteOn, etc. The drawbacks of conventional methods are discussed and schemes based on signal processing in frequency domain are applied to minimize the influence of spurious signals that affect the measurement accuracy. With the choice of applied excitation signal, a 100-fold improvement in SNR has been achieved. Similarly, with alteration of signal postprocessing methodology, we have reported a 10-fold faster dual-slope method that can be employed for a variety of

high-throughput applications, especially in drug-discovery industry. To further optimize the microchip that uses less than a hundred nanoliter of reagent volume for bio-characterization. Discrete liquid droplets are synthesized in an ordered fashion to carry out the bioreaction that conventionally utilizes reagent volumes ranging from a few hundred microliters to a few milliliters.

I dedicate this thesis to my mother and the Lord almighty for the strength and encouragement I have found in them.

TABLE OF CONTENTS

Chapters

ACKNOWLEDGEMENTS

The author thanks the guidance and support of Dr. Carlos H. Mastrangelo, who introduced me to the field of microfluidics and integrated microchips for biosensing applications. I also thank Dr. Vladimir Hlady for his assistance with understanding and working knowledge of surface science and surface interactions, a crucial aspect of my research work. I also received valuable inputs and suggestions on fabrication of SPR microchips from Dr. Layne D. Williams. From the standpoint of fabrication of biosensing devices in general, the discussions I have had with staffers in the Microfabrication Facility of University of Utah, especially Brian Baker and Tony Olsen, made a strong impact on my research. I would also like to thank my lab members and fellow researchers, in particular Dr. Yan Xie and Dr. Farouq Azizi, for their assistance with the research experiments and device fabrication steps. Finally, I deeply thank my beloved mother, my grandmother, and late grandfather for lending me their support and patience, without which none of this would have been possible.

CHAPTER 1

INTRODUCTION

Proteomic and similar other kinds of bio-molecular interactions require a sensitive and preferably label-free sensing tool to characterize the interaction kinetics. The information is important for understanding the development of events such as cell adhesion, viral infection, and rational drug design. The most popular label-free sensing mechanism suited to this kind of biosensing is based on an optical phenomenon called Surface Plasmon Resonance (SPR). SPR is noninvasive and is capable of real-time sensing and quantification. In this chapter, we introduce the working principles of SPR-based transducers, the SPR system configurations, and its various tradeoffs for detection limit and speed.

1.1 Surface Plasmon Resonance (SPR)

Surface Plasmon Resonance (SPR) is an optical phenomenon based on excitation of surface plasmons (SPs) at the interface of a noble metal and a dielectric layer. The electrons on a metal surface collectively oscillate and are called surface plasma waves or surface plasmons. These oscillations of charge density are localized in z-direction within the Thomas-Fermi screening length of around 0.1 nm. SPs, however, cannot be

---

Certain portions of this chapter are reproduced with permission from the article "Low Noise Detection of Biomolecular Interactions with Signal-Locking Surface Plasmon Resonance", Williams, L.; Ghosh, T.; Mastrangelo, C. *Anal. Chem.*, 2010, 82, 6025-6031. Copyright [2010] American Chemical Society.

transformed into light and vice-versa but can be excited optically or by electrons.

In this work, we have used optical excitation-based SPR transducers. When excited optically, SPs couple with the exciting photons and form a standing electromagnetic wave that propagates along the metal/dielectric surface and decay exponentially perpendicular to the surface with a characteristic decay length. Two different SP excitation (optically) configurations exist, namely Kretschmann and Otto, for coupling photons with SP. Figure 1.1 shows a typical Kretschmann configuration. In this configuration, a thin metal layer of gold or silver is sputtered on top of this prism and photons from an incident source of wavelength λ (usually a laser) are coupled to SP through a prism.

When the angle of incidence θ_i is greater than the critical angle θ_c, total internal reflection (TIR) conditions exist in the prism where most of the light at prism face is reflected back and an evanescent wave is formed. Under these conditions, the evanescent wave penetrates through the metal and couple with the SPs, exciting them. The evanescent wave vector K_I at the prism/metal interface is given by

$$K_I = \left(\frac{\omega_0}{c}\right)\sqrt{n_0}\sin\theta_i \tag{1.1}$$

where ω_0 is the wave frequency in vacuum, c is speed of light in vacuum, and n_0 is the refractive index (R.I.) of the prism. Resonance conditions for SPs occur at the interface between metal and exiting dielectric layer when at a particular θ_i,

$$\sqrt{\frac{\varepsilon_1(\omega)}{\varepsilon_1(\omega)+1}}=\sqrt{n_0}\sin\theta_i \tag{1.2}$$

where $\varepsilon_1(\omega)$ is the frequency-dependent dielectric permittivity constant of the metal satisfying the condition Real $[\varepsilon_1] < 0$ and $|\varepsilon_1| > \varepsilon_2$ where ε_2 is the dielectric constant for the

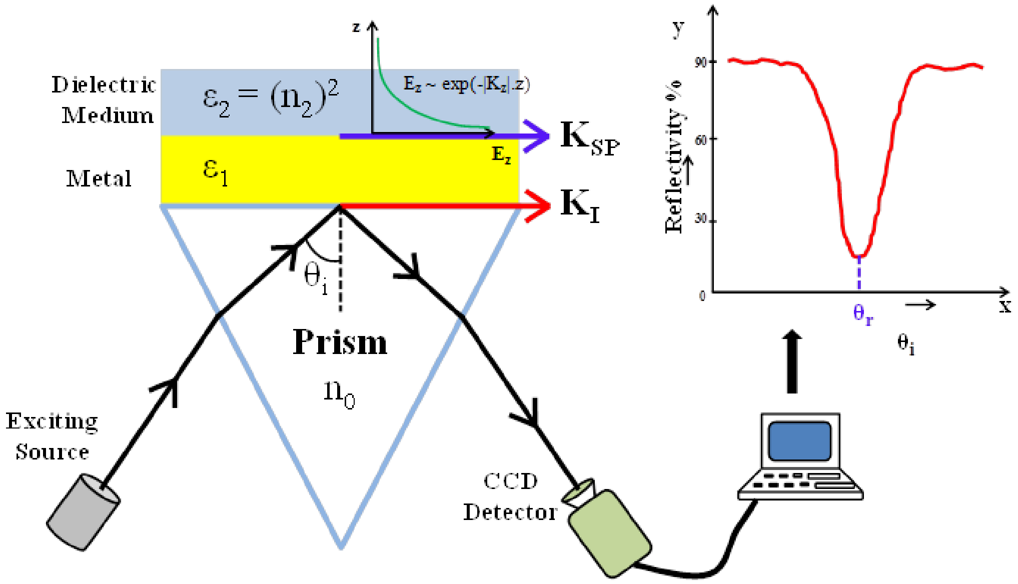

Figure 1.1. A general Kretsschmann configuration of SPR sensing. The real-time sensing in this scheme and also for our system is carried out at a constant resonance angle θ_r.

dielectric. For the overlying exiting medium, ε_2 is calculated as square of R.I. (ε_2 is 1 for air and 2.25 for fused silica). At this resonance condition, the photons that are reflected from the prism/metal interface undergo destructive interference with the photons that are emitted by the excited SPs and the reflectance curve captured by a sensing devise shows a narrow dip in intensity. This phenomenon occurring at the interface is referred to as SPR [1,2]. The angle of incidence at this resonating condition is denoted by θ_r, as shown in Figure 1.1. Wave vector K_{SP} of Figure 1.1 equals $2\pi/\lambda_p$ where λ_p is the wavelength of plasma oscillations. Wave vector in the perpendicular z-direction is denoted by K_Z, the field amplitude of which (denoted by E_Z) decays exponentially from the metal surface and is extremely sensitive to R.I. changes within a shallow region of this metal/dielectric interface. For metal/dielectric system, wave vector used in all equations and derivations is related to its frequency by the dispersion relation given by

$$K_x = \frac{\omega_x}{c}\sqrt{\frac{\varepsilon_1(\omega)\cdot\varepsilon_2}{\varepsilon_1(\omega)+\varepsilon_2}} \tag{1.3}$$

1.2 SPR-based Biosensing

For a fixed angle of incidence and R.I. of the prism, the angle of resonance shift with change of local R.I. of the overlying exiting medium [3,4]. This dependence of reflectance minima around resonant condition is utilized by SPR-based biosensors.

1.2.1 Sensing of Biological Interactions

Biological interactions can be sensed using SPR (Figure 1.2) if a biomolecule of interest (we refer to this as a ligand) is immobilized on top of the metal layer (40~50 nm) and an analyte is transported over the metal surface. Since biological interactions with

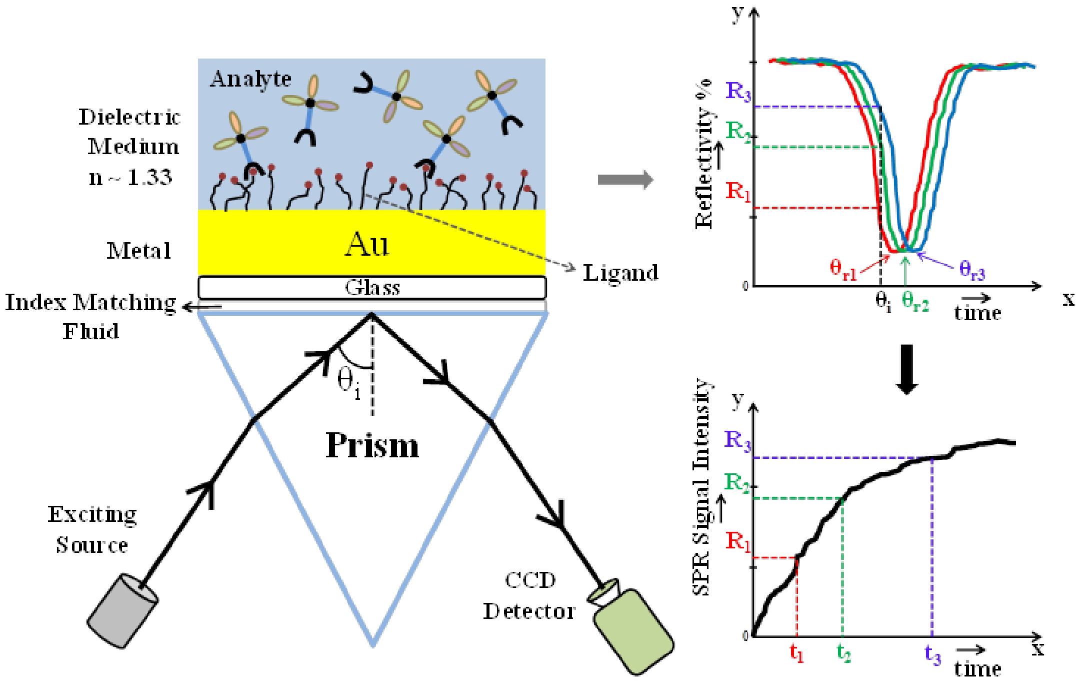

Figure 1.2. Biosensing scheme of SPR.

SPR require surface modification prior to surface anchoring of the ligand, Au is preferred over other metals as it offers a wide range surface chemistry options. We will assume the metal layer to be Au henceforth. The use of Au and procedures of its surface modification will be explained in greater details in the next chapter.

Chemical binding interaction and complex formation between the analyte and the ligand produces a mass change right at the surface, resulting in change of local R.I. Consequently, the angle of plasmon resonance shifts in a direction (increases with R.I. and vice-versa) corresponding to a shift of R.I. which manifests as a change in reflectance intensity. As shown in Figure 1.2, this reflectance change around the minima is monitored in real-time, producing a SPR signal intensity that is directly proportional to the accumulation of bio-mass on a gold surface. It must be noted that some SPR systems are calibrated to monitor the shift of θ_r in real-time as against the reflectance intensity (in our case); the SPR signal curve though remains linearly proportional to a change in either. Since the electric field amplitude decays exponentially in z-direction, SPR-based biosensors are able to sense R.I. changes that occur 300~400 nm from the gold surface. SPR devices have been reported to sense R.I. changes of around 10^{-7} refractive index units (RIU).

As illustrated in Figure 1.2, for biosensors, the metal film is deposited on a glass substrate that is coupled to the prism with an index matching fluid. The TIR conditions now occur inside the glass substrate instead of the prism. This practical Kretschmann set-up enables the user to couple a replaceable SPR sensing substrate with a fixed prism that is optically aligned with other instrument modules of the SPR imaging set-up. For a majority of SPR biosensors, the value of ε_2 for plasmon excitation is designed to be around 1.7. This value corresponds to a dielectric medium that has R.I around 1.3 which is similar to R.I of standard bench-top buffers that are used as the solvent medium for these biological interactions.

Over the course of the last two decades, SPR has evolved into a popular and sensitive label-free sensing technique that is utilized for a variety of biosensing. SPR-based biosensing is being currently employed for studying a wide spectrum of bio-interactions in real-time, like DNA hybridization [5,6], DNA-RNA binding [7], DNA-protein binding [8,9], aptamer-protein binding [10], antibody-antigen binding [11,12], detection of proteins from whole blood [13], drug detection from saliva [14], and other biological [15-17] and drug-protein [19] interactions.

1.3 Microfluidics

Microfluidics refers to the handling, manipulation, and control of fluids that are confined inside geometric features of micrometer scale [20]. Introduction of microfluidics dates back to the 1970s. The development and successful application of photolithography and semiconductor microfabrication technology like MEMS (Micro Electro Mechanical Systems) [21] in microelectronic industry prompted research groups to investigate the application of similar fabrication techniques to construct devices that can study biological and chemical processes in a confined volume. From the development of microfabricated pressure sensors in late 60s to the fabrication of the first microfluidic chromatographic analyzer [22], research and advancement in fabrication of miniaturized fluidic devices continued to grow. This was soon followed by the fabrication of micro-channels and micro-impressions that can be molded and sealed (usually with a material that provides mechanical stability and robustness) to form a microfluidic chip. Figure 1.3 shows typical microfluidic chips made of PDMS as mold material and glass as sealing material.

Over the years, many microfluidic devices or chips have been developed to perform more complicated laboratory procedures inside a single chip, also called ‘Lab-on-a-Chip’ (LOC) devices [23]. Microfluidics today is viewed as a necessary tool for studying a wide spectrum of biological, chemical, biochemical, electrical, electomechanical, and optical applications [20] mainly due to reduced sample consumption and sensing time and low dispersion characterestics which affect the detection accuracy otherwise.

1.3.1 Microchips for Biosensing

Miniaturization reduces expense in terms of chip fabrication and reagent consumption and provides a greater speed of sensing owing to faster experimental and analysis times. Microfluidics offer an added advantage of control and precision over fluid handling and manipulation conditions, making it a favorable platform for a large number of biological applications that demand greater control over micro-environment conditions and high-throughput. Detection and sensing in a microchip format is being currently applied to a large pool of biological and biomedical analysis, including Polymerase Chain Reaction (PCR), DNA sequencing, DNA and Protein Microarrays, immunoassay, etc. [24, 25]. As we shall see in later chapters, the novel techniques that are proposed in this work require precise control over liquid flow and dispersive mixing of reagents for successful implementation. A detailed discussion on the fabrication and integration of microfluidic components suited to this biosensing is discussed in Chapter 2.

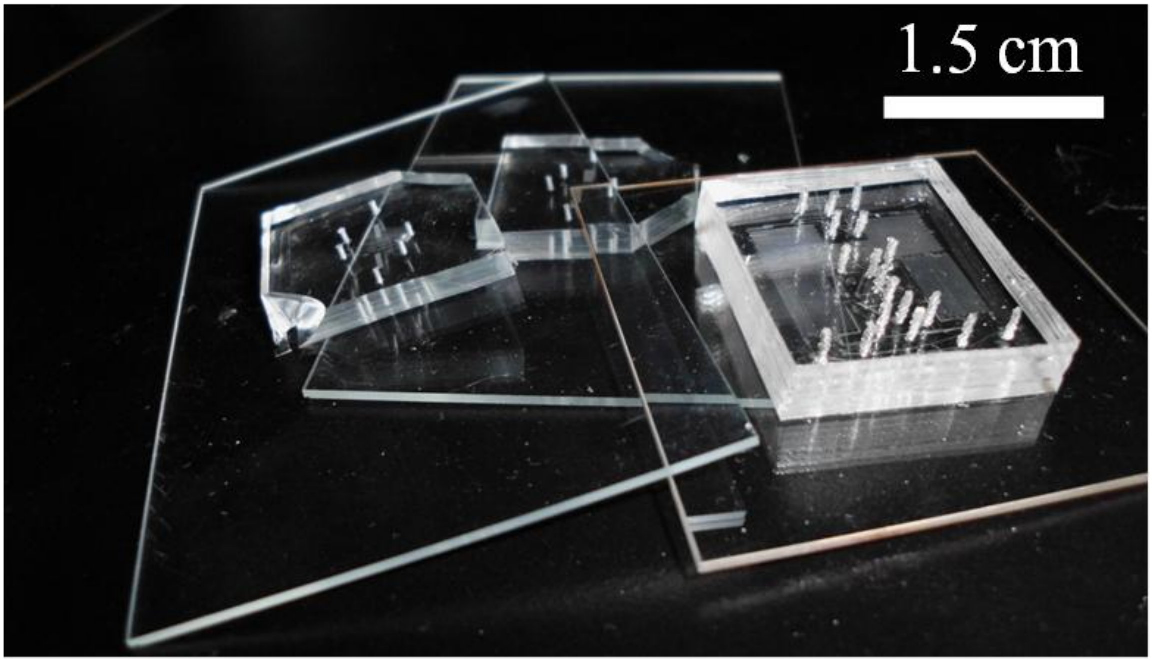

Figure 1.3. Hybrid PDMS/Glass microchips fabricated in our laboratory.

1.4 Conventional SPR Biosensing and Analysis Schemes

Biomolecular interaction analysis (BIA) of macromolecules like proteins and oligonucleotides is the primary tool used for investigations and analytical findings in the fields of functional proteomics and genomics. Many widely-used BIA systems like BIAcore and ProteOn use SPR as their sensing technology [18,19]. BIA addresses a large pool of biological interactions that were discussed in Section 1.2.1. The final goal of BIA is characterization of the binding kinetics of bio-reactions with maximum analytical accuracy. In this section, we will first discuss the theoretical assumptions of a bio-interaction involving two species which will be followed by conventional methods of quantification and rate constant extraction. Interactions where one of them can be a well-behaved macromolecule follow a simple reversible bimolecular Langmurian equation [26] given by

$$\mathrm{A} + \mathrm{B} \underset{\mathrm{k_d}}{\overset{\mathrm{k_a}}{\rightleftharpoons}} \mathrm{AB} \tag{1.4}$$

where A and B are reacting species, AB is the interaction complex, and k_a and k_d are kinetic association and dissociation rate constants, respectively. We will henceforth refer to A as the analyte (the mobile species in solution), B as the ligand (immobilized on gold transducer surface) and AB as the bio-complex, respectively. The rate of formation of the complex AB as a function of time t in the association phase subject to analyte flow (concentration in buffer solution is [A]) can be written as

$$\frac{\mathrm{d[AB]}}{\mathrm{dt}} = \mathrm{k_a[A][B]} - \mathrm{k_d[AB]} \tag{1.5}$$

where [B] is the surface concentration of the immobilized ligand [18]. The dissociation rate of complex AB subject to buffer flow in dissociation phase is given by

$$\frac{d[AB]}{dt} = -k_d[AB] \tag{1.6}$$

Analytical integration of rate Equations (1.5) and (1.6) yields piecewise exponential solutions of complex formation and dissociation, respectively. The concentration of complex AB can also be rearranged as the total surface concentration of immobilized ligand B_0 minus available ligand B for binding. This forms the basis for conventional SPR measurements, most common being a single association-dissociation step [18, 27-29] depicted in the real-time sensorgram of Figure 1.4. At any point of sensing, the SPR sensorgram specified by the imager intensity I(t) is proportional to this bound complex concentration [AB]. The constant of this proportionality varies for different SPR imagers and is denoted by the term G_{SPR}. In the association cycle, the signal intensity can then be written as

$$I_A(t) = G_{SPR} \cdot [AB](t) = G_{SPR} \cdot \left(\frac{k_a[A][B_o]}{k_a[A]+k_d} \right) \cdot (1-e^{-(k_a[A]+k_d)\cdot t}) \tag{1.7}$$

where $[B_0]$ is the maximum surface concentration of the active ligand and [AB](t) is the time-dependent surface concentration of the complex. Similarly, the SPR signal for dissociation cycle can be written as

$$I_D(t) = G_{SPR} \cdot [AB](t) = G_{SPR} \cdot [AB_d] \cdot e^{-k_d \cdot t} \tag{1.8}$$

where $[AB_d]$ is the concentration of bound complex *AB* prior to dissociation under buffer flow. This SPR signal intensity obtained from the sensing imager is fitted to the model exponential curves of Equations (1.7) and (1.8) and the characteristic association and dissociation kinetic constants are extracted [30,31] from the fitted parameters. Since the reaction is carried out under continuous flow conditions in subsequent steps of analyte and buffer flow, this conventional methodology of kinetic parameter estimation from the

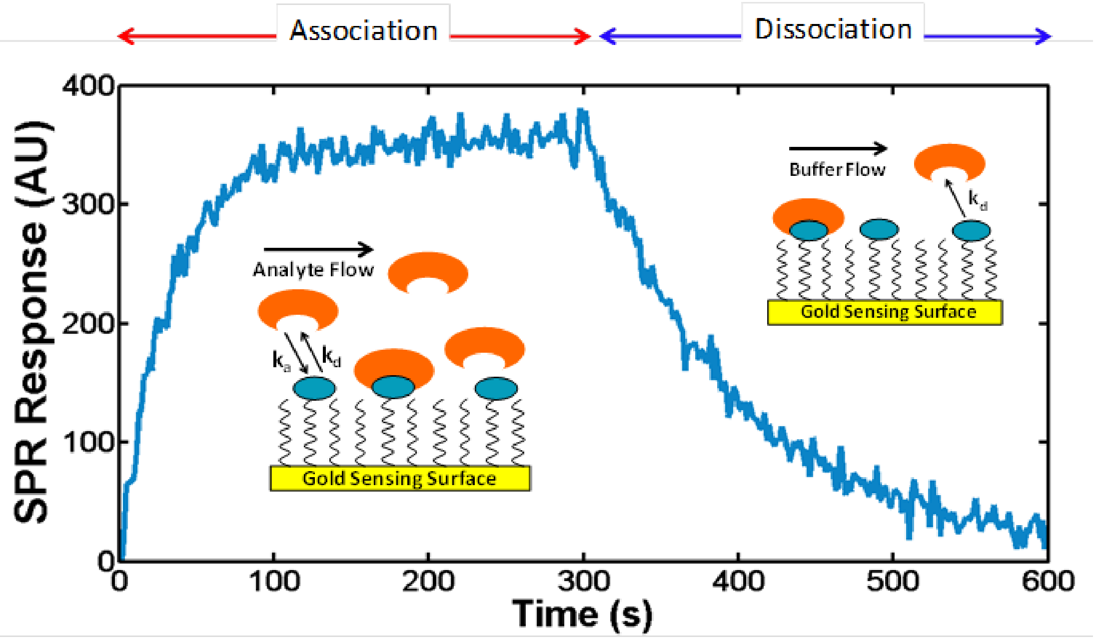

Figure 1.4. SPR sensorgram for the conventional SPR biosensing in which the raw data are plotted postcapture in the above manner. This is followed by postprocessing and extraction of the kinetic parameters that characterize the investigated biochemical reaction of the illustrated graphics.

experimental response is referred to as step-response method (SRM). Equations (1.7) and (1.8) represent the idealized SPR sensorgram response.

1.4.1 Drawbacks of Conventional SRM

Typically SPR sensors are also sensitive to the bulk characteristics of the solvent which vary with its R.I. In the association and dissociation steps of the sensorgram, this manifests as an increment or decrement of the signal that stays constant for the time period of the solution introduced, thus producing a bulk output s(t) along with I(t). In addition, the sensorgram signal is subject to drifts and noise originating from a variety of environmental sources (ambient temperature fluctuations, slow drifts, thermal drifts, white noise, etc.) and the imaging equipment. These effects can be lumped together as disturbance d(t) that is added to idealized SPR output and given by

$$I(t) = G_{SPR}.[AB](t) + s(t) + d(t) \tag{1.9}$$

The contribution s(t) from the bulk characterestics of the solvent can be subtracted from equation (1.9) to yield an SPR sensorgram having an intensity change happening only due to bio-interaction and mass change at the surface of the transducer. This is usually done by using an independent measurement of the bulk R.I. shift denoted by $s_{ref}(t)$ on a nonreacting surface that serves as our reference [19]. The two separate SPR signals are baselined to zero and $s_{ref}(t)$ is substracted from I(t) which is then used for curve fitting and kinetic parameter estimation. Figure 1.4 shows an example SPR response that has been baselined and referenced in both association and dissociation phases. The contribution from disturbance d(t), however, cannot be completely eliminated in I(t) since G_{SPR} is itself dependent on noise elements from the imaging camera. This dependence of

SRM on spurious and uncorrelated signals presents a major drawback of the measurement scheme. As we shall see, these erroneous signals limit the resolution of detection and the parameter estimation accuracy by SRM gets compromised. In the following section, we will discuss the drawbacks of conventional SRM which forms the basis of this thesis work.

1.4.1.1 Disturbance Rejection and Signal Orthogonality

In a typical SPR experiment, the curve fitting procedure in conventional SRM uses Levenberg-Marquardt technique, geometrical interpretation of which requires orthogonality [32] between the Jacobian of the exponential and the disturbance d(t). This poses a problem because the exponential pulse is not orthogonal to common non-oscillatory disturbances such as slow drifts. Let us first look into the structural origin of this disturbance susceptibility [33].

The fundamental weakness of the fitting method becomes evident when the recorded data consist of purely spurious signals. Consider, for example, a simple linear drift of constant slope typically caused by a gradual temperature change in the experimental set-up, as shown in Figure 1.5. Clearly, there is no reaction at the surface, but the linear drift yields a best-fitting SRM exponential pulse and an erroneous result. Similar errors are caused with many other nonlinear and monotonic drifts. This pitfall is the consequence of the poor orthogonality properties of the SRM exponential pulse.

Specifically, two continuous time signals a(t) and b(t) representative of recorded and model responses are orthogonal when

$$\int a(t)b(t)dt = \vec{a}\bullet\vec{b} = <\vec{a},\vec{b}> = 0 \tag{1.10}$$

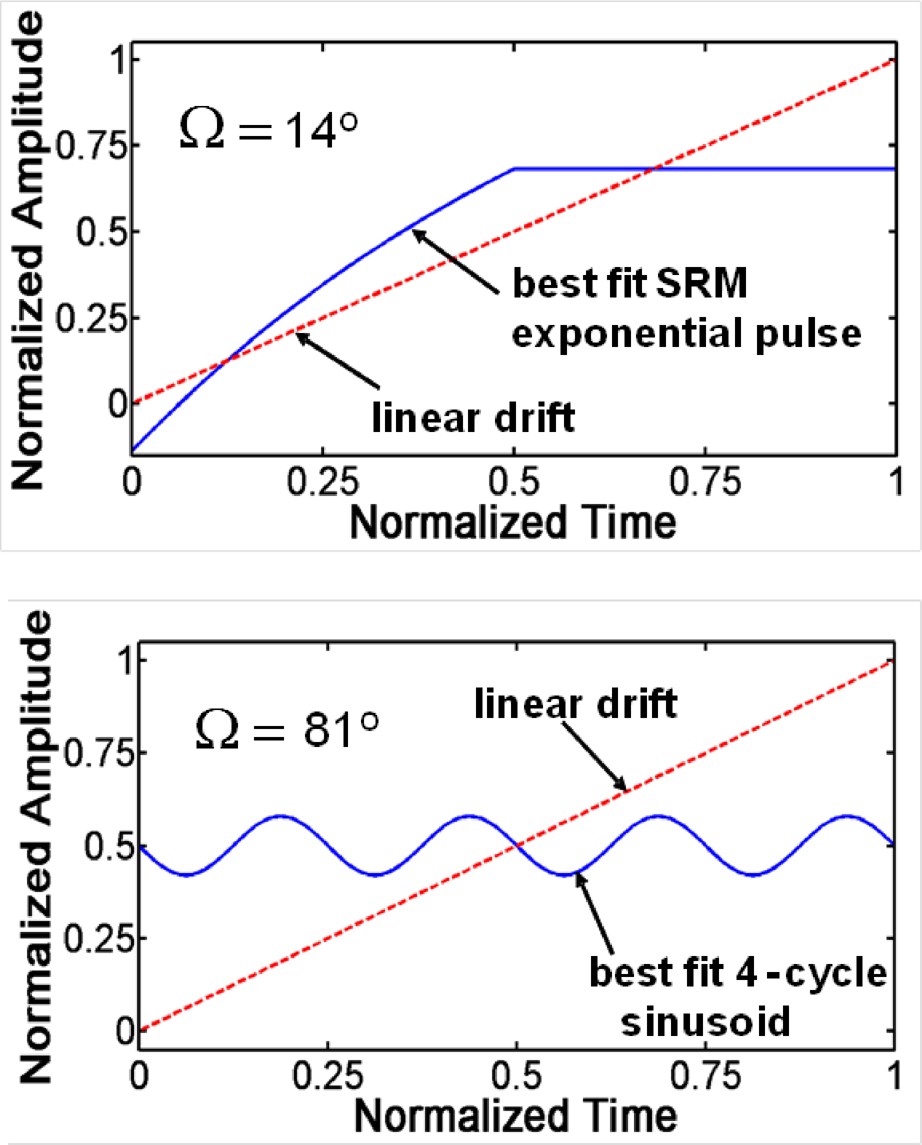

Figure 1.5. Fitted response to a linear drift. Best-fitting exponential pulse (top) and a rapid oscillatory response (bottom).

The best way to understand Equation (1.10) and its orthogonality meaning is to think of signals a(t) and b(t) as vectors $\vec{a}$ and $\vec{b}$ oriented in an infinitely dimensional signal space. The integral hence corresponds to their dot product which is zero when the two vector signals are orthogonal. In our real SPR system, the observed signal $\vec{s}$ and the true SPR response $\vec{r}$ are related by

$$\vec{s} = \vec{r} + \vec{d} \tag{1.11}$$

where $\vec{d}$ is the disturbance vector. The true response is estimated from the best fit to $\vec{m}(\vec{p})$ corresponding to the model SPR response. The model response is a function of parameter vector $\vec{p}$. The best fit corresponds to the parameter vector with the largest projection of $\vec{s}$ onto $\vec{m}(\vec{p})$. In this procedure, note that the disturbance also influences the fit through its projection

$$\vec{d}_P(\vec{p}) = \left(\frac{\vec{d} \bullet \vec{m}(\vec{p})}{\vec{m}(\vec{p}) \bullet \vec{m}(\vec{p})} \right) \vec{m}(\vec{p}) \tag{1.12}$$

thus producing an error. The error is minimized when the disturbance is orthogonal to the model response, or alternatively when the angle given by

$$\Omega(\vec{p}) = \cos^{-1}\left(\frac{\vec{d} \bullet \vec{m}(\vec{p})}{|d||\vec{m}(\vec{p})|} \right) \tag{1.13}$$

is as close to $\pm 90^{o}$ as possible. Equation (1.13) states that one may improve the rejection of the disturbance by simply selecting an appropriate model response. For good rejection, it is desirable that the SPR response be orthogonal to all possible uncorrelated signals but itself. Generally speaking, for good orthogonality, the model response should be oscillatory in nature, while the regular SPR exponential model response is not. Figure 1.5

shows the angle Ω for a linear disturbance and two different model responses. For the single best fitting exponential pulse, Ω is 14^{o}, but for a four-cycle sinusoid of fixed frequency, the angle is a much higher 81^{o}; hence, the oscillatory signal has 5-fold superior rejection.

In the presence of substantial noise and systematic drifts, the step-response fitting scheme is only able to accurately detect relatively coarse interactions between the analyte and ligand. In drug discovery applications, this is a major limitation, as often drug targets are large proteins with masses of 10^{4}-10^{5} dalton (Da) or larger, and the interaction of interest is often triggered by the binding of a very small analyte (300 Da or less). In order to increase the sensitivity of these systems, commercial state-of-the-art instruments such as the BIAcore and ProteOn use many corrective schemes, including sophisticated referencing [19], data scrubbing software [34,35], temperature control [36], and most successfully, the use of high-density binding sites on three-dimensional dextran surfaces [28]. In spite of the commercial availability of several SPR systems for many years, they have not been able to sense interactions of small analytes, presently 100 Da being the minimum detectable mass.

1.4.1.2 Slow Detection and High Sample Consumption

In this section, we discuss the additional notable limitations of kinetic and equilibrium constants obtained by the method of nonlinear least squares in SRM [31]. As indicated in this detailed study, for dissociation constants less than 10^{-5} s^{-1}, it is difficult to distinguish dissociation constant in the measurements of pure association phase at different analyte concentrations. For greater accuracy of parameter estimation, a longer time period of data acquisition is recommended. In must be noted that curve fitting of dissociation phases can, however, distinguish between dissociation steps at different concentrations even below the value 10^{-6} s^{-1}. In the instance of very high dissociation rates (> 10^{-1} s^{-1}) and very low analyte mass, the dissociation phase data are deemed redundant as the rates are beyond limit of determination and are hence extracted from equilibrium analysis [37]. Therefore, the most thorough analysis of SPR data can be done when the equilibrium binding constant is relatively high [31]. In general, all conditions mentioned above require a sensorgram acquisition period in the order of a few minutes for a complete step-response cycle at one concentration [18,28,29,31,37-39] and hence consumes a substantial amount of precious bio-samples as well. This is accompanied by the fact that for rate estimation using equilibrium analysis [31,38], the association phase has to go to equilibrium which consumes more time. Besides, the association and dissociation phases in SRM are sequential and hence inseparable. These experimental limitations make SRM an intrinsically slow and a high sample consuming process, resulting in high detection costs of sensing and low throughput.

1.4.2 Addressing Drawbacks: Chemical Signal Processing

The key to further improvements in detection limits of SPR-based systems lies in the development of more robust sensing techniques that can reject experimental noise and disturbances more efficiently. Given the slow nature of SRM, the development of faster detection schemes has also emerged as an important area of research as SPR is presently being considered as a candidate label-free technology for high-throughput drug screening. Over the years, SPR-based BIA has gained considerable popularity in pharmaceutical industry where it is used as a primary and secondary drug screening tool. However, the accuracy of binding kinetic parameters estimated from BIA relies heavily on its numerical techniques of quantification. As we have seen earlier, the conventional method currently employed in BIA uses SRM which is not very reliable when it comes to detection of fine biomolecular interactions in presence of systemic disturbances. Measurement techniques which are able to reject spurious and uncorrelated signals with maximum efficiency and improve SNR of the sensorgram in a time- and cost-effective way are highly desirable in the study of such fine interactions and thus require our greater attention. This thesis addresses the aforementioned drawbacks using chemical signal processing techniques implemented inside microfluidic chips integrated with SPR.

In the following chapters, we will introduce the theory of the new techniques of measurement for kinetic characterization of bio-interactions. These schemes will address the drawbacks of SRM that were discussed in the previous chapter. The proposed methods are intended to be introduced in conjunction with microfluidic components in order to achieve maximum accuracy and speed of detection. Since these schemes require processing of the biochemical signals postdetection, we will broadly categorize them as chemical signal processing techniques.

First in Chapter 2, we will discuss the fabrication and postfabrication processing of SPR microchips that will be used for the implementation of the new measurement schemes.

From Chapters 3 through 6, we will discuss the theory behind the various chemical signal processing methods and demonstrate the implementation of these schemes using these method specific microfluidic SPR chips. Experimental results and conclusions of individual measurement methods are discussed at the end of the chapter.

Finally, we will present the conclusions and future scope of this research work in Chapter 7.

1.5 References

1. Rothenhausler, B.; Knoll, W. *Nature*, 1988, 332, 615–617.
2. Yeatman, E.; Ash, E. A. *Electron. Lett*., 1987, 23, 1091–1092.
3. Campbell, C. T.; Kim, G. *Biomaterials*, 2007, 28, 2380–2392.
4. Schasfoort, R. B. M.; Tudos, A. J. *Handbook of Surface Plasmon Resonance*; Royal Society of Chemistry, Cambridge, 2008.
5. Li, Y.; Wark, A. W.; Lee, H. J.; Corn, R. M. *Anal. Chem*., 2006, 78, 3158–3164.
6. Malic, L.; Veres, T.; Tabrizian, M. *Biosens. Bioelectron*., 2009, 24, 2218–2224.
7. Goodrich, T. T.; Lee, H. J.; Corn, R. M. *J. Am. Chem. Soc*., 2004, 126, 4086-4087.
8. Wegner, G. J.; Lee, H. J.; Marriott, G.; Corn, R. M. *Anal. Chem*., 2003, 75, 4740-4746.
9. Shumaker-Parry, J. S.; Aebersold, R.; Campbell, C.T. Anal. Chem., 2004, 76, 2071-2082.
10. Li, Y.; Lee, H. J.; Corn, R. M. *Anal. Chem*., 2007, 79, 1082–1088.
11. Wegner, G. J.; Lee, H. J.; Corn, R. M. *Anal. Chem*., 2002, 74, 5161–5168.
12. Lee, K. H.; Su, Y. D.; Chen, S. J.; Tseng, F. G.; Lee, G. B. *Biosens. Bioelectron*., 2007, 23, 466–472.
13. Lausted, C. G.; Hu, Z.; Hood, L. E. *Mol. Cell Proteomics*, 2008, 7,2464–2474.
14. Fu, E.; Chinowsky, T.; Nelson, K.; Johnston, K.; Edwards, T.; Helton, K.; Grow, M.; Miller, J. W.; Yager, P. Ann. N. Y. *Acad. Sci*., 2007, 1098, 335–344.
15. Piliarik, M.; Vaisocherov, H.; Homola, J. *Biosens. Bioelectron*., 2005, 20, 2104-2110.
16. Wassaf, D.; Kuang, G.; Kopacz, K.; Wu, Q. L.; Nguyen, Q.; Toews, M.; Cosic, J.; Jacques, J.; Wiltshire, S.; Lambert, J.; Pazmany, C. C.; Hogan, S.; Ladner, R. C.; Nixon, A. E.; Sexton, D. J. *Anal. Biochem*., 2006, 351, 241–253.
17. Shumaker-Parry, J. S.; Zareie, M. H.; Aebersold, R.; Campbell, C. T. *Anal. Chem*., 2004, 76, 918–929.

18. Jönsson, U.; Fägerstam, L.; Ivarsson, B.; Johnsson, B.; Karlsson, R.; Lundh, K.; Löfås, S.; Persson, B.; Roos, H.; Rönnberg, I.; Sjölander, S.; Stenber, E.; Ståhlberg, R.; Urbaniczky, C.; Östlin, H.; Malmqvist, M. *Biotechniques*, 1991, 11, 620–627.

19. Myszka, D. *J. Mol. Recognit*., 1999, 12, 279–284.

20. Nguyen, N. T.; Wereley, S. *Fundamentals and applications of Microfluidics*, Artech House, Boston, 2006.

21. Ghodssi, R.; Lin, P. *MEMS Materials and Processes Handbook*; Springer, Berlin, 2011.

22. Terry, S. C.; Jerman, J. H.; Angell, J. B. *IEEE Trans. on Electron Devices*, 1979, 26, 1880-1886.

23. Herold, K. E.; Rasooly, A. *Lab-on-a-Chip Technology: Fabrication and Microfluidics*, Caister Academic Press, Norfolk, 2009.

24. Berthier, J.; Silberzan, P. *Microfluidics for Biotechnology*; Artech House, Boston, 2010.

25. Gomez, F. A. *Biological Applications of Microfluidics*; John Wiley & Sons: Hoboken, New Jersey, 2008.

26. Karlsson, R.; Michaelsson, A.; Mattson, L. *J. Immunol. Methods*., 1991, 145, 229-240.

27. Stenberg, E., Persson, B., Roos, H., and Urbaniczky, C. *J. Colloid Interface Sci.*, 1991, 143, 513–526.

28. Löfas, S.; Johnsson, B. *J. Chem. Soc*; *Chem. Commun*., 1990, 21, 1526-1528.

29. Williams, L.; Ghosh, T.; Mastrangelo, C. *Anal. Chem*., 2010, 82, 6025-6031.

30. Fagerstam, L. G.; Frostell-Karlsson, A.; Karlsson, R.; Persson, B.; Ronnberg, I. *J. Chromatogr.,* 1992, 597, 397-410.

31. O'Shannessy, D. J.; Bringham-Burke, M.; Soneson, K. K.; Hensley, P.; Brooks, I. *Anal. Biochem*., 1993, 212, 457-468.

32. Moon, T.; Stirling, W. In *Mathematical Methods and Algorithms for Signal Processing*, Prentice-Hall: New Jersey, 2000.

33. Ghosh, T.; Williams, L.; Mastrangelo, C. *Lab on a Chip*, 2011, 11, 4194-4199.

34. Khalifa, M.; Choulier, L.; Lortat-Jacob, H.; Altschuh, D.; Vernet, T. *Anal. Biochem*., 2001, 293, 194-203.

35. Navratilova, I.; Papilia, G.; Rich, R. Bedinger, D.; Brophy, S.; Condon, B.; Deng, T.; Emerick, A.; Guan, H.-W.; Hayden, T.; Heutmekers, T.; Hoorelbeke, B.; McCroskey, M,; Murphy, M.; Nakagawa, T.; Parmeggiani, F.; Qin, X.; Reve, S.; Tomasevic, N.; Tsang, T.; Waddell, M.; Zhang, F.; Leavitt, S.; Myszka, D. *Anal. Biochem.,* 2001, 364, 67-77.

36. Shen, B.-J.; Hage, T.; Sebald, W. *Eur. J. Biochem*., 1996, 240, 252-261.

37. Myszka, D. G. *Anal. Biochem*., 2004, 329, 316-323.

38. Corr, M.; Slanetz, A. E.; Boyd, L. F.; Jelonak, M. T.; Khilko, S.; Al-Ramadi, B. K.; Kim, Y. S.; Maher, S. E.; Bothwell, A. L. M.; Marguiles, D. H. *Science*, 1994, 265, 946-949.

39. Lahiri, J.; Isaacs, L.; Brzybowski, B.; Carbeck, J. D.; Whitesides, G. M. *Langmuir*,1999, 15, 7186-7198.

40. Ghosh, T.; Mastrangelo, C. *Analyst*, 2012, 137, 2381-2385.

CHAPTER 2

MICROCHIP DESIGN: MATERIALS, FABRICATION, AND TESTING

2.1 Introduction

In this chapter, we will discuss the experimental methodologies that are employed for the implementation of the chemical signal processing microchips. These microchip fabrication and integration techniques will be employed for designing experiments of different signal processing methods in Chapters 3-6. We start with a broad section on SPR microchips where we first discuss the basic design and fabrication aspects. In following subsections, we discuss the surface modification strategies that follow the chip assembly. All the signal schemes we have introduced will be tested on a specific type of surface chemistry as a model. The kinetic constants of the chosen interaction pair will be evaluated separately for each of the schemes in later chapters.

2.1.1 SPR Microchips

The microfluidics of the chip should be able to support switching of flow between samples used in the bio-reaction and simultaneously generate the chemical signals with low dispersion. Secondly, it should have components integrated for sensing on-chip real-time SPR sensorgrams. We will refer to such an assembled microfluidic chip as an SPR microchip. Here we will first discuss the considerations behind the design of the

Certain portions of this chapter are reproduced with permission from the article “Low Noise Detection of Biomolecular Interactions with Signal-Locking Surface Plasmon Resonance”, Williams, L.; Ghosh, T.; Mastrangelo, C. *Anal. Chem.*, 2010, 82, 6025-6031. Copyright [2010] American Chemical Society.

microfluidics of the chips used in this study. General fabrication steps and integration of the chip with SPR components will be discussed in the fabrication subsection. In subsequent subsections, we discuss the surface chemistry and modifications of the sensing surface inside these SPR microchips prior to experimental runs of the schemes. This is followed by subsections where we will discuss the integration of the microchip with microfluidic signal generation instrumentation and the SPR optical instrumentation set-up separately.

2.1.1.1 Design Considerations

Generally speaking, in order to implement these spectral and other measurement techniques, it is necessary to generate and transport a stream of analyte plugs to the sensing site with minimal distortion for the entire frequency range of the scan. While this approach is theoretically straightforward, there are severe difficulties associated with the chemical signal generation and transmission. A practical scheme can only be realized within the microscopic channels available in microfluidic chips which provide low dispersion. Since we will be using pressure as the driving source of fluid flow, the transmission of solute signals is subject to Taylor dispersive mixing inside these microchannels which broadens and diffuses the solute plugs as they travel from the signal generator to the sensing site. This results in a large enhancement of the solute diffusion in the solution. The adjusted effective dispersion diffusion coefficient D_{eff} in rectangular microfluidic channel capillaries [1] is approximately given by

$$D_{eff} \cong D_0 \cdot \left(1 + \frac{\alpha(w,h) \cdot V^2}{D_0^2} \right) \tag{2.1}$$

where α is a function of height h and the width w of the flow channel [10]

$$\alpha(w,h) \cong \frac{1}{210}\cdot\left(\frac{8.5\cdot h^2\cdot w^2}{h^2+2.4\cdot h\cdot w+w^2}\right) \tag{2.2}$$

where D_0 is the original solute diffusion coefficient and V is the average flow velocity. For channels having dimensions in millimeters and with average velocities in the range of few cm/s, the diffusion enhancement has very large values in the order of 10^7 or higher; precluding any signal resulting from transport in macroscopic environments. This enhancement factor has a quadratic reduction with channel diameter. The transmission of chemical signals through dispersion inside these channels has a low-pass filter behavior [2,3]. The low-pass filter transmission pole is given by

$$p_t \approx \left(\frac{V^3}{D_{eff}\cdot L}\right)^{1/2} \tag{2.3}$$

where L is channel distance between the signal generator release point and the sensor site. An excitation signal transported through a channel with $\omega > p_t$ will have inherently have amplitude reduction. This pole gives us an idea of the maximum frequency of the applied input signal. For example, in a microfluidic flow cell which is about 5 mm long having rectangular cross-sectional dimensions of 10 × 25 μm^2, a solute with diffusion constant $D_0=10^{-9}$ m^2/s and a flow velocity of 5 cm/s has a transmission pole of about 11.5 Hz. In contrast, a flow cell having cross-sectional dimensions 1000 × 1000 μm^2 and about 1 cm length at the same flow velocity gives us a cut-off frequency lower than 0.1 Hz. This difference in the values of pole cut-off frequency mandates the viability of the technique in microfluidic environments for generation of chemical signals where dispersion is low. As we shall see, all the experimental data from all SPR microchips are processed for frequency components that are at least an order lower than this transmission pole frequency.

2.1.1.2 Materials

In this section, we will list all the materials and reagents that have been used in fabrication and postfabrication procedures. The SPR microchips for the most part have been assembled using photolithographic equipments and methods at the Nanofabrication facility of the University of Utah. All photoresists (AZ 1500, AZ9260, SU-8, and S1813), developer solvents (AZ300MIF, AZ400MIF, 352, SU-8 developer), p-type Si wafers (4 inch diameter), Chrome etch solution, Gold Etch solution, Buffered Oxide Etch (BOE), 49 % Hydrofluoric Acid (HF), 30% Hydrogen Peroxide (H2O2), 96% Sulfuric Acid (H2SO4) solutions, and photolithographic instruments (Heidelberg MicroPG 101, Suss MA1006, TMV Super, Technics PE-II A, Oxford PlasmaLab 80) are provided by the fabrication facility. Chemicals 5 kDa carboxymethyl-polyethylene glycol-thiol (cm-PEG-SH) and 2 kDa methoxy-PEG-thiol (m-PEG-SH) were purchased from Laysan Bio. Sulfo-N-hydroxysuccinimide (S-NHS), N-ethyl-N'-(3-dimethylaminopropyl) carbodiimide (EDC), and phosphate buffered saline (PBS) tablets were obtained from Thermo Scientific. Carbonic anhydrase II (CA-II), 4-(2-Aminoethyl) benzenesulfonamide (ABS) and 10% sodium dodecyl sulfate (SDS) solutions were obtained from Sigma. Sylgard 184 from Dow Chemicals was used to make the PDMS. Square SF10 glass substrates (RI = 1.72) 2 x 2 inch^2 were purchased from Schott glass. Deionized (DI) water for rinsing and buffer preparation was provided by an in-house plant associated with the University of Utah Nanofabrication house. Syringes of capacity 1 mL, 5 mL, and 10 mL are obtained from General Stores and receiving, University of Utah and a programmable syringe pump (Cole-Parmer single-syringe infusion pump, 115 VAC) is obtained from Cole-Parmer®. Tubing (Tygon PVC tubing, inner and outer diameters of 0.01 and 0.03 inch, respectively) and syringe needles (Stainless Steel blunt needle with 30 gauge Luer Polypropylene hub, 0.5 inch) used for connecting and sample delivery from the sample reservoirs to the microchip is obtained online from Smallparts.com.

2.1.1.3 Fabrication

Irrespective of the signal processing scheme, all the microfluidic chips are fabricated and implemented using a conventional two-level PDMS technology on glass substrates [3-5]. In this two-layer channel system, the top layer has microchannels that facilitate pressure driven fluid flow (buffer, analyte, etc.) and the bottom layer has micro-impressions that are aligned beneath the flow channels. These impressions are called valves. Similar to the fluid flow, these valves are actuated by a driving pressure which is ~5-10 PSI (pound per square inch) higher than the fluid driving pressure. When actuated, these valves seal the overlying microchannel and stops the flow, thus facilitating the flow switching and fluid plug generation. Each fluid channel has a dedicated valve that controls its flow. The switching pattern of these valves determines the type of input chemical signal [3,4] that is synthesized and transported to SPR sensing sites in output channels, and the designs for input signal generation will be discussed for individual schemes in respective chapters.

A graphic presentation of the general fabrication steps of a two-level PDMS microchip is illustrated in Figure 2.1. These PDMS/glass hybrid chips are fabricated using conventional photo-lithography, making it a relatively simple and inexpensive method of

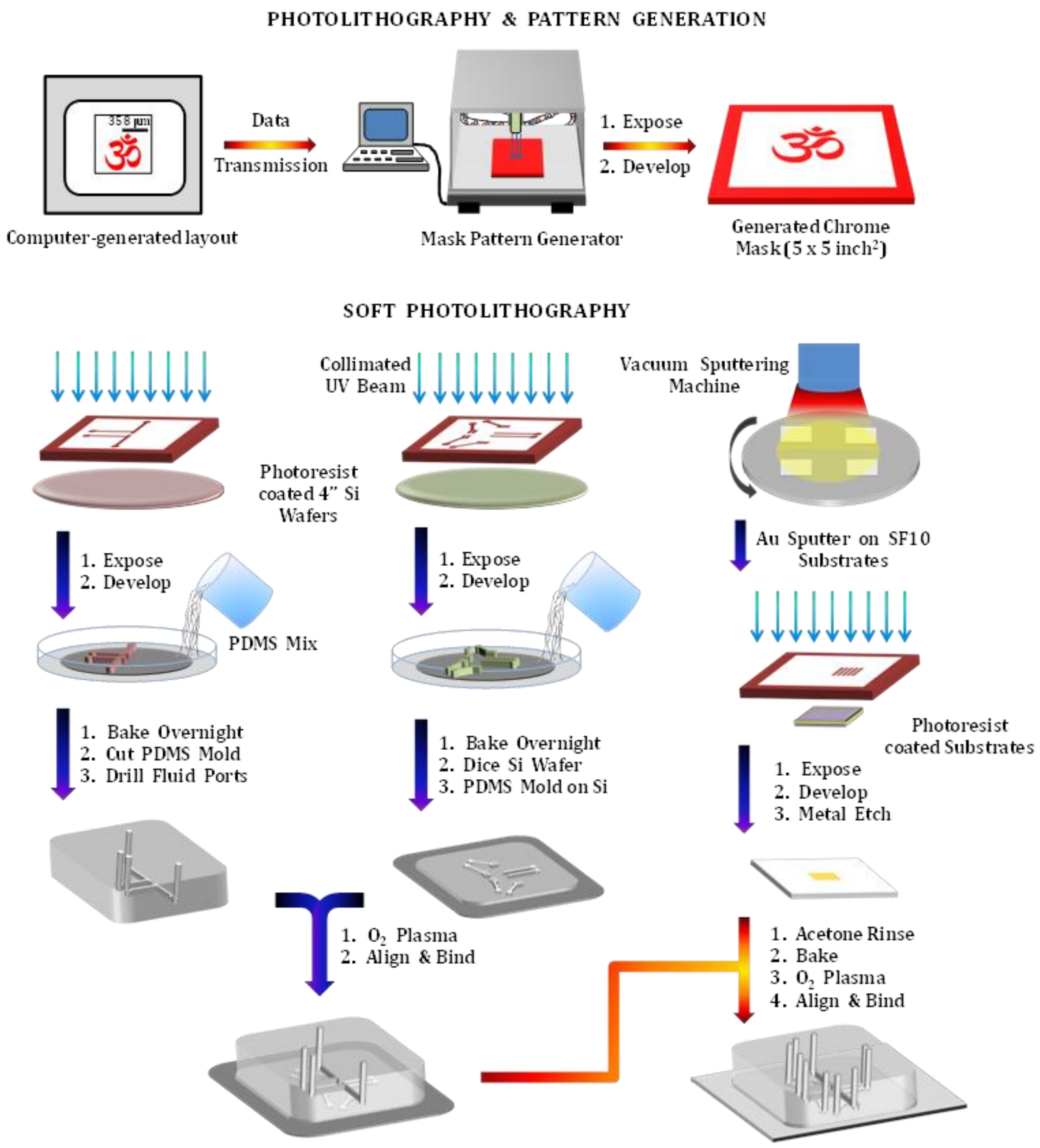

Figure 2.1. A graphical illustration of fabrication steps for a two-level PDMS microchip integrated with SPR sensing gold spots.

microchip assembly. The basic layout of a chip for each scheme is first generated in an editing software (L-Edit in our case) which is then fed to a pattern generator (Heidelberg MicroPG 101) for generating the 2-D impression on a chrome mask (5×5 inch^2 square, coated with AZ1500 photoresist). At this point, it must be noted that a pattern generation on any substrate (silicon Si in our case) implies that a photoresist-coated substrate is first exposed to 380 nm UV light through masks using an aligner (Suss MA1006) followed by developing in a solvent where the unexposed/exposed part of a negative/positive photoresist is etched away, leaving a 3-D pattern where the thickness of 2-D impression is that of the photoresist coat. The exposed masks are first developed in AZ300 MIF developer followed by dipping in a chrome etching solution for 2 minutes where the areas without the photoresist coat are etched away, leaving an opaque impression of the design layer in chrome on a transparent mask plate. The width of this 2-D impression, or in other words the microchannel width used in all the schemes, usually ranges from 180~200 μm. The Si wafers are first dipped in BOE solution for 1 minute followed by HF for another 1 minute. They are blown dry with N_2 and heated at 100 ^{0}C for 2 minutes, after which they are ready for spin-coating. As shown in Figure 2.1, three different masks (two for the layers and one for gold sensing spots on glass substrate) are generated and the ones for microfluidic layers are used to create the two different patterns on Si wafers. The top layer is patterned in a 23 μm thick layer of spin-coated AZ9260 photoresist (spin-coated @ 1000 rpm for 40 s) and the bottom layer is patterned using a 20 μm thick negative photoresist SU-8 (spin-coated @ 1600 rpm for 40 s). The developing solutions used for SU-8 and AZ9260 are SU-8 Developer and AZ400MIF, respectively. After this, the PDMS (mixed with curing agent in a ratio 10:1 by mass) is poured over these Si wafers patterned with top layer and left to cure at 40 ^{0}C overnight. In case of the bottom layer, PDMS is spin-coated (@ 2000 rpm for 1 minute) and cured to form a thin peel on the Si wafer. After this, they are removed from the curing oven and stored at room temperature until used. A molded PDMS block is then cut out from the wafer with the top layer and this is cleaned with acetone and heated at 100 ^{0}C for 5 minutes and cooled down to room temperature (~ 23 ^{0}C) for another 10 minutes. A wafer piece that contains SU-8 pattern and the PDMS peel on top of it is similarly prepared. The two pieces are then exposed to oxygen plasma for 20 seconds at a pressure of 100 mTorr and RF power of 40 W (March Plasmod system, Technics PE-II A, Oxford PlasmaLab 80) and then aligned and bonded together using an in-house built alignment system.

The third mask is used for patterning gold spots on glass substrates (SF10 glass). The glass substrates are first cleaned by piranha etch (3:1 v/v, $H_2SO4:H_2O_2$) for 20 minutes, rinsed for 5 minutes in deionized (DI) water and then dried under nitrogen gas N_2. The substrates are placed in an oven at 80 °C for 10 minutes before being transferred to a TM Vacuum sputter deposition system. A 3 nm adhesion layer of Ti/W is deposited, followed by 40 nm of gold (Au). The metal layers on the substrate are then collectively patterned using S1813 photoresist. After photolithographic exposure and developing in developer 352, the glass substrates are rinsed in DI water for 2 minutes blown dry in N_2, after which the metals are etched with gold etch solution (4:1 ratio by mass of $KI:I_2$) and H_2O_2 separately for 2 minutes each. The patterned substrates used in the assembly of SPR microchips consist of 200 x 200 μm^2 Au spot arrays which form our SPR sensing sites. Finally, the photoresist is removed with acetone and the patterned SF10 substrates are stored in a desiccator until used.

The two-layer PDMS mold is then aligned, bonded, and sealed with the patterned SF10 substrate using a similar O_2 plasma and alignment method. Figure 2.2 shows the first-generation SPR microchip fabricated by the above methodology. At this point, our SPR microchip is ready for the next experimental step: surface modification of SPR gold spots for immobilization of the ligand. This forms the intermediate step between an SPR microchip assembly and the experimental procedures where a chemical signal in analyte will be synthesized and transported for monitoring SPR response of the bio-reaction.

2.1.1.4 Surface Modification

2.1.1.4.1 A Mixed PEG Layer

As discussed in Section 1.2.1, the ligand of a bio-interaction pair to be studied is immobilized on the surface of Au which then gives us an SPR response when subject to analyte flow. Also, since referencing (see Section 1.4) needs a control reference surface which gives the SPR signal from the bulk R.I. shift of the analyte and buffer, we need a non-reacting surface in its vicinity which has no ligand anchored over it. The SPR response from such a referencing surface also gives us an idea of the nonspecific surface fouling by the biomolecules in analyte. It is also desirable for the immobilized ligand molecules to have an appropriate orientation on the surface for bio-recognition by the analyte. The modification of the surface with a brush of a hydrophilic polymer that can reduce this biofouling and improve the bio-recognition levels has been a wide topic of research. Over the years, polyethylene glycol (PEG) has developed as the polymer of choice. Due to its biocompatibility with most biomolecules, large exclusion volume, and extensive hydrogen bonding and flexibility properties in aqueous medium, the use of

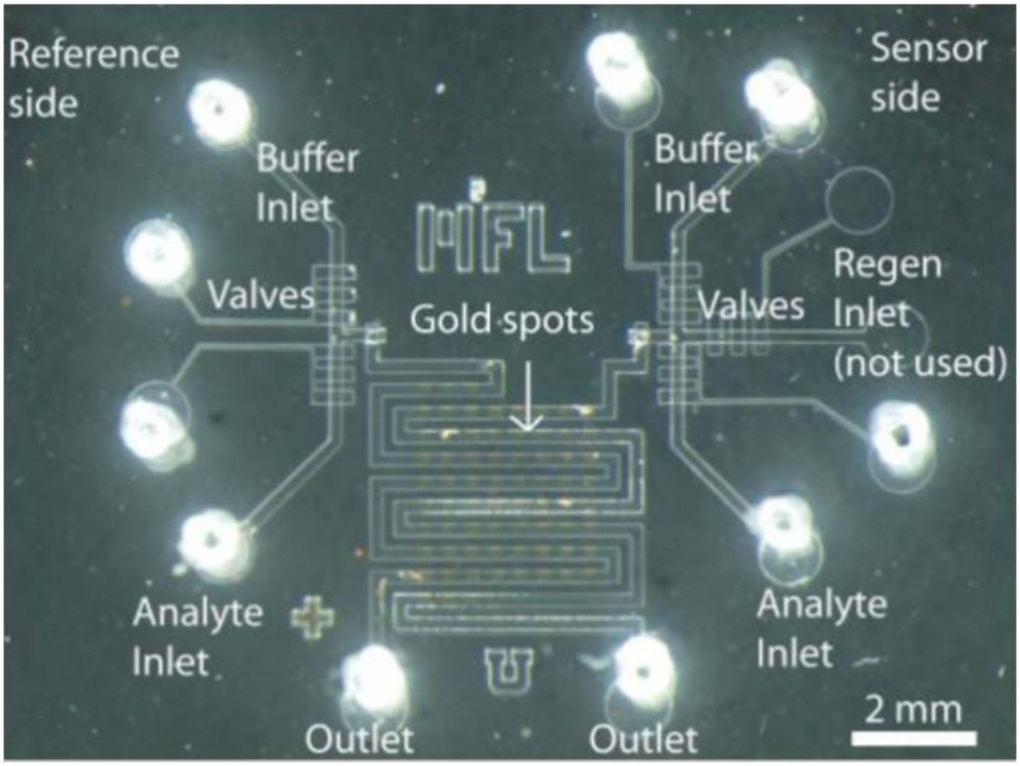

Figure 2.2. Image of a first-generation SPR microchip fabricated using two-level PDMS technology, with the patterned gold on the SF10 glass substrates. As we shall see, SPR biosensing of a biological interaction in general requires separate sensing and referencing compartments.

PEG as an antifouling agent was extensively studied [6-9]. Since reduction of the signal contributed from nonspecific surface events also improves SNR of the SPR response, we will use a surface chemistry protocol of biofouling reduction and ligand immobilization developed by Uchida [10] to modify our SPR surface. As demonstrated by authors [10,11], a SPR chip is modified by grafting two sulfanyl-ended PEG molecules of different chain lengths (2 and 5 kDa, respectively) to form a dense mixed brush of tethered PEG chains which are capable of eliminating the biofouling characteristics of biomolecules (particularly DNA and proteins). Another advantage of this protocol states that the surface modifications can be carried out in aqueous medium as opposed to other methods where self-assembled monolayers (SAMs) [12-14] of non-fouling agents like modified and unmodified alkanethiolates are grafted to the surface in ethanol. Since a large number of polymers that are used for making microchips (PDMS in our case) are porous to ethanol, it results in unwanted swelling.

Modification of the Au spots is performed in situ to avoid disturbance of the delicate surface chemistry during O_2 plasma step for the bonding steps of the PDMS with the glass substrates. The assembled SPR microchip is first connected to a syringe pump which has a solution filled syringe (1 mL) and flushed with 0.01 M HCl for 5 minutes to remove any contaminants or oxide, followed by a 15-minute rinse with DI water. The long 5 kDa cm-PEG molecule is introduced to the flow channels for 20 minutes at a flow rate of 0.8 mL/hour and concentration of 1mg/mL, followed by a 0.05 M NaOH rinse. Then the 2 kDa m-PEG is flown through the channels and rinsed in a similar manner. The PEG molecules are dissolved in a high ionic strength PBS buffer (50 mM Phosphate, 1 M Nacl, pH ~ 7.4). The smaller PEG is applied a total of three times to backfill any gaps in the initial PEG layer and prevent protein adsorption on the gold surface. Once the PEG tethered chains are grafted, the longer PEG chains are chemically modified for conjugating and anchoring the ligand on the sensing surface and a blocking agent on reference surface, respectively.

The surface is again treated with 0.01 M HCl and rinsed with DI water to ensure the proper chemical functionalization for the next step. This chemical modification of the cm-PEG chain is performed using S-NHS and EDC to create an amine reactive surface. S-NHS at 100 mM and EDC at 400 mM of concentration in water are mixed in 1:1 ratio and passed through both the reference and sensing channels for 30 minutes. This modifies the carboxylic acid group of cm-PEG into a NHS ester for zero length cross-linking with an amine-modified ligand and blocking agents. The system is rinsed with DI water for 2 minutes to wash away remnant S-NHS and EDC. A ligand (see next section) and a blocking agent (50 mM ethanolamine in PBS buffer at pH ~ 9) with the terminal amine group are then flown over the sensing and reference Au surface, respectively, for 30 minutes. This is followed by another 20-minute flow of ethanolamine followed by DI water and 1X PBS (10 mM Phosphate, pH ~ 7.4) rinse.

2.1.1.4.2 A Model Protein-Drug Pair

All the signal-locking and other SPR detection concepts are tested using a well-established protein-small molecule interaction pair of carbonic anhydrase-II (CA-II, M.W ~ 29 kDa) and 4-(2-Aminoethyl) benzenesulfonamide (ABS, M.W ~ 200 Da) similar to that used previously [14-17]. As reported by authors [18,19], a para-substituted benzenesulfonamide molecule binds specifically to the enzyme CA by co-ordination of the sulfonamide moiety with a zinc ion at the interaction site of CA. The small molecule with the sulfonamide group is anchored to the surface and acts as our ligand and CA II dissolved in 1X PBS is our analyte. For all experiments in this work, this pair will be the test model and 1X PBS is used as our standard running buffer. The para-group of benzenesulfomaide in our case is chosen to be an amino-ethyl group to take advantage of the amino group that can be cross-linked to surface carboxylic acids of cm-PEG using a standard S-NHS/EDC protocol [14,16], thus presenting a benzenesulfonamide group on the SPR surface for recognition and binding with CA II. The reported association and dissociation constant values for the binding reaction have a range of $10^3 \sim 10^7$ $M^{-1}s^{-1}$ and $10^{-3} \sim 10^{-1}$ s^{-1}, respectively. Since the values are influenced by surface concentration of ligands and the type of hydrophilic brush used in the gold modification scheme, we will evaluate the kinetic constants using SRM for our PEGylated Au surface and use it as a reference value for the measured constants from all other SPR schemes. All the chemical modifications above can also be found in our previous work [20].

The reaction and blocked reference SPR surfaces are now ready for the next experimental step: integration of the microchip with SPR instrumentation.

2.1.1.5 Integration with SPR Instrumentation

Figure 2.3 shows our SPR instrument with the microfluidics and other sensing components. A modified GWC Technologies SPRimager®2 system is used for performing the SPR experiments and collecting real-time SPR sensorgram raw data. The system was modified by the manufacturer so that we can use it in a horizontal [20]

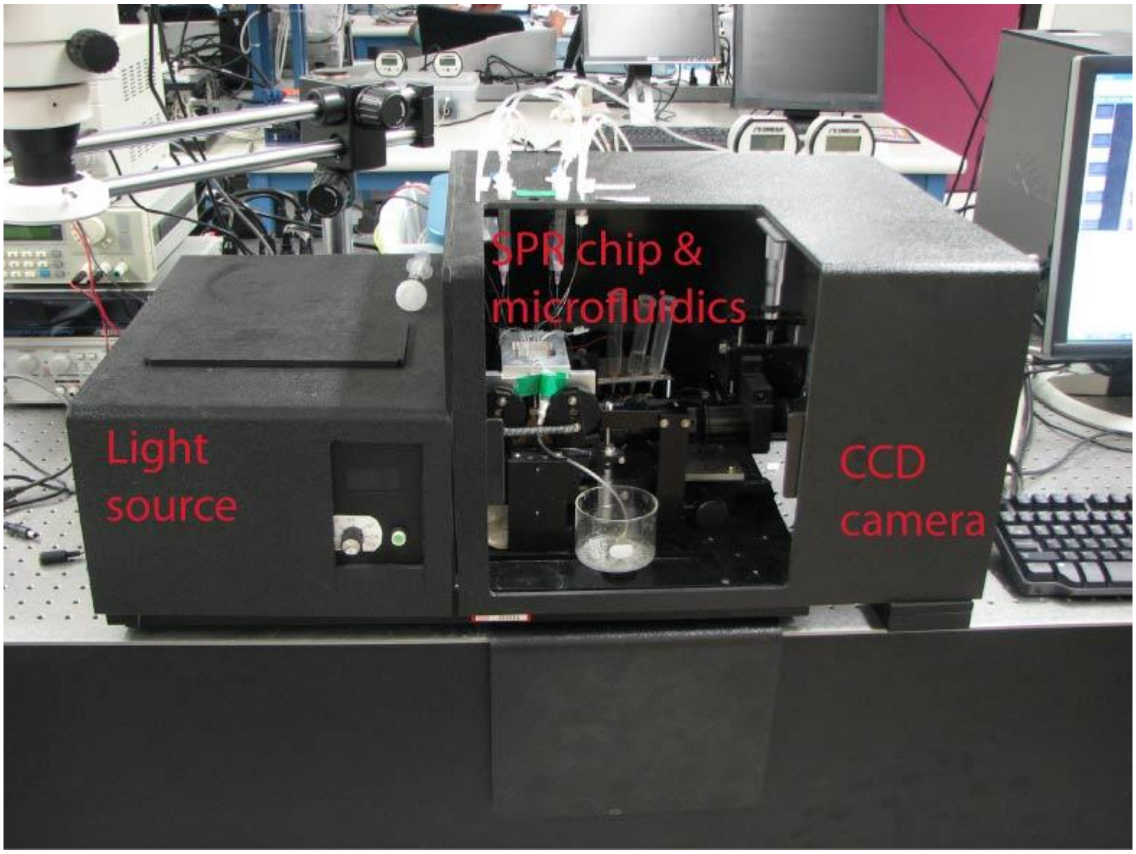

Figure 2.3. Our SPR instrumentation system integrated with microfluidic components.

configuration incorporating a custom built microfluidic mounting stage and mounting cell. We further modified the instrument with the following instrumental parts: a World Star Tech TEGCIRL-100G-808 808 nm laser source, a rotating diffuser from Suss-Microoptics, a Navitar Zoom 6000 lens system, and a Hamamatsu C9100-01 EMCCD camera. Following surface modification, the SPR microchip is coupled to a prism using index matching liquid and the cell is loaded onto the mounting stage. Inside the stage, the cell is positioned where the light from the laser excites and senses gold spots in the chip. The angle of incidence can be controlled by a rotating knob that tilts the stage. The output SPR signal subject to chemical input signal is collected by an EMCCD camera which is controlled by Wasabi Software. All the SPR integration steps above can also be found in our previous work [20].

2.1.1.6 Integration with Microfluidic Components

The SPR microchip of Figure 2.2 is first subject to surface modification procedures by solution flow in microchannels lined with sensing Au spots. This is done by programming the pump to deliver the samples at a predefined flow rate calibrated for 1 mL syringe pumps. The syringe delivers the sample to the microchannels through polyvinyl chloride (PVC) tubing that is connected to a needle at the syringe tip at one end and a 0.02 inch diameter drilled inlet microfluidic port at the other.

The integration of mounted SPR chips with microfluidic components post-surface-modification is carried out in a similar fashion. As shown in Figure 2.2, drilled solution input ports are dedicated to the reservoir of a specific sample for both surface modification and actual experimental steps (analyte, buffer, and regeneration solutions, respectively) and form a water-tight connection with the PVC tube. Output ports are similarly drilled which dumps the solutions from output channels to the waste reservoir through the tubes. The sample reservoirs are connected to a pressure source P_0 which drives the solution through the channels. The flow switching of the samples is facilitated by the presence of dedicated valves beneath the flow channels.

The SPR signal from the sensing Au spots in output channels (sense + reference) are recorded by the EMCCD camera using a camera-control Wasabi Software which converts the real-time sensorgram intensity values I(t) in a readable and extractable format (Microsoft Excel), which is used for further data processing.

2.1.2 Signal Postprocessing

Wasabi camera software first analyzes the collected data by selecting multiple sensing and reference SPR spots in the collected images. The mean intensity values for all the user-chosen zones in each recorded frame are stacked in the readable format. Fourier transform analysis, exponential and linear curve-fitting, and similar other signal processing schemes postextraction are performed on this data by a digital algorithm which is coded in MATLAB®. As mentioned in conventional SRM of Section 1.4, the intensity values from both the sensing and reference surface are first baselined to zero and subtracted from each other followed by further postprocessing in MATLAB to extract kinetic parameters which are specific to the individual schemes.

2.2 References

1. Dutta, D.; Leighton, Jr. D. T. *Anal. Chem*., 2001, 73, 504-513.
2. Xie, Y.; Wang, Y.; Chen, L.; Mastrangelo, C. *Lab on a Chip,* 2008, 8, 779-785.
3. Azizi, F.; Mastrangelo, C. *Lab on a Chip*, 2008, 8, 907-912.
4. Chen, L.; Azizi, F.; Mastrangelo, C. *Lab on a Chip*, 2007, 7, 850-855.
5. Thorsen, T.; Maerkl, S. J.; Quake, S. *Science,* 2002, 239, 580-584.
6. Mori, Y.; Nagaoka, S.; Takiuchi, H.; Kikuchi, T.; Noguchi, N.; Tanzawa, H.; Noishiki, Y. *Trans. Am. Soc. Artif. Intern. Organs*, 1982, 28, 459-463.
7. Jeon, S. I.; Andrade, J. D. *J. Colloid Interface Sci.*, 1991, 142, 159-166.
8. Gölander, C. G.; Herron, J. N.; Lim, K.; Claesson, P.; Stenius, P.; Andrade, J. D. In *Poly(Ethyleneglycol) Chemistry, Biotechnical and Biomedical Applications*, Plenum Press: New York, 1992.
9. Lina, Y. S.; Hlady, V.; Gölander1, C. G. *Colloids and surfaces B. Biointerfaces*, 1994, 3, 49-62.
10. Uchida, K., Otsuka, H., Kaneko, M., Kataoka, K. & Nagasaki, Y. 2005, *Anal. Chem*., 77, 1075-1080.
11. Uchida, K.; Hoshino, Y.; Tamura, A.; Yoshimoto, K.; Kojima, S.; Yamashita, K.; Yamanaka, I.; Otsuka, H.; Kataoka, K.; Nagasaki, Y. *Biointerphases*, 2007, 2, 126-130.
12. Bain, C. D.; Troughton, E. B.; Tao, Y. T.; Evall, J.; Whitesides, G. M.; Nuzzo, R. G. *J. Am. Chem. Soc.*, 111 , 321-335.
13. Love, J. C.; Estroff, L. A.; Kriebel, J. K.; Nuzzo, R. G.; Whitesides, G. M. *Chem. Rev.*, 2005 105, 1103–1169.
14. Lahiri, J.; Isaacs, L.; Brzybowski, B.; Carbeck, J. D.; Whitesides, G. M. *Langmuir*, 1999, 15, 7186-7198.
15. Mrksich, M.; Grunwell, J. R.; Whitesides, G. M. *J. Am. Chem. Soc*., 1995, 117, 12009-12010.
16. Lahiri, J.; Isaacs, L.; Tien, J.; Whitesides, G. M. *Anal. Chem*., 1999, 71, 777-790.
17. Myszka, D. G. *Anal. Biochem*., 2004, 329, 316-323.

18. Dodgson, S. J.; Tashian, R. E.; Gros, G.; Carter, N. D. *The Carbonic Anhydrases: Cellular Physiology and Molecular Genetics*, Plenum Press: New York, 1991.

19. Taylor, P. W.; King, R. W.; Burgen, A. S. V. *Biochemistry*, 1970, 9, 3894-3902.

20. Williams, L.; Ghosh, T.; Mastrangelo, C. *Anal. Chem*., 2010, 82, 6025-6031.

CHAPTER 3

METHOD 1: SIGNAL-LOCKING FOURIER TRANSFORM SPR

Certain figures and text portions of this chapter content have been reproduced with permission from [1] (see footnote). As a statement of contribution from authors for this chapter (recommended by dissertation supervisory committee as the introductory paragraph), the theory and analytical background for the SLFT-SPR methods have been developed by the first and third authors. The SPR instrumentation, microchip design, and farbication have been contributed by the first author while chip testing has been contributed by the second author. The biochemical functionalization steps and the mathematical analysis in MATLAB have been contributed by the second author.

3.1 Introduction and Theory

In this chapter, we introduce the theory of the first chemical signal processing method, frequency domain signal-locking fourier transformSPR (SLFT-SPR), mentioned previously in section 1.4.2. This is followed by implementation of the signal analysis of signal-locking SPR method. Implementation strategy includes schematics of this measurement scheme followed by discussion on large signal SLFT-SPR chip and its input chemical signal synthesis. This is followed by a results section where we will discuss the experiments and analyze the kinetic parameters and the SNR obtained from

---

Certain portions of this chapter are reproduced with permission from the article "Low Noise Detection of Biomolecular Interactions with Signal-Locking Surface Plasmon Resonance", Williams, L.; Ghosh, T.; Mastrangelo, C. *Anal. Chem.*, 2010, 82, 6025-6031. Copyright [2010] American Chemical Society.

the conventional SRM and large signal SPR outputs. Finally, we conclude the chapter with a discussion on the merits, drawbacks, and future scope of the work.

3.1.1 Frequency Domain Signal-Locking SPR Scheme

The SRM discussed in Chapter 2 is not an optimal detection method because it does not attempt to reject the influence of the disturbance on the fit. In this section, we introduce the theory behind a new detection scheme based on measurement and subsequent kinetic constant calculation in frequency domain. This method is aimed at rejecting the influence of disturbances by improving the SNR of the SPR sensorgram and hence the detection resolution and accuracy. If the ordinary differential equation (1.6) for the biochemical interaction is linear in [A] (analyte concentration), it is possible to substantially improve the sensitivity of the measurement by appropriate selection of the input test signal. An improved detection scheme can be implemented if the analyte excitation and the corresponding interaction response are highly correlated. The SRM requires a-priori knowledge of the reaction dynamics, the number of species involved, and the order of the reaction. The assumed model information is, however, not required if one treats the biochemical reaction as a general dynamical system under test as shown in the block diagram of Figure 3.1. The concentration of the product [C] (also referred to as formed complex [AB]) follows the first order reaction dynamics specified by the ordinary differential equation of Equation 1.6. Since the biochemical system is linear, the input signal and output response are correlated to each other at a particular input modulation frequency ω_i, as shown in the figure. Since the analyte input signal and the corresponding sensorgram response have sharp autocorrelations, the input signal and the

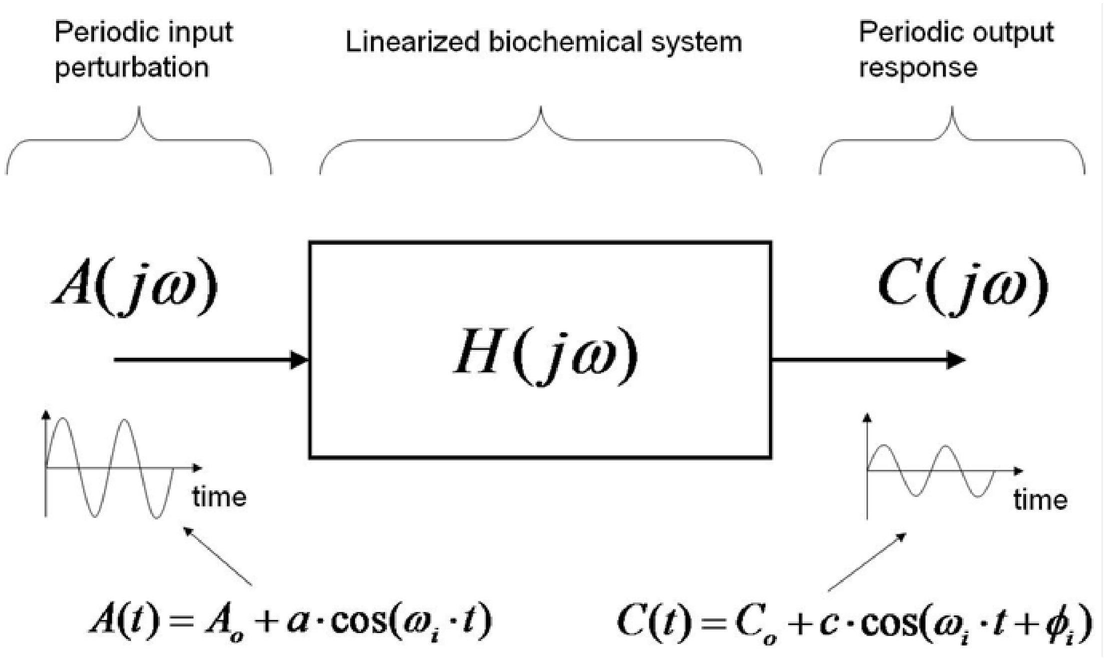

Figure 3.1. The biochemical reaction under test can be abstracted as a general dynamical system that can be excited with input chemical signals. The system response under periodic excitation is its transfer function.

response are nearly orthogonal to all other signals except themselves, hence rejecting greatly the influence of uncorrelated noise and disturbances.

An example of such an approach is the signal-locking Fourier-transform SPR (SLFT-SPR) detection scheme shown in the diagram of Figure 3.2. In this method the biochemical system is driven by a periodic input excitation of analyte or buffer of constant frequency f_ϕ specified by digital clocks ϕ and $\overline{\phi}$. The corresponding periodic association and dissociation cycles produce a highly correlated sensorgram output of the same frequency. This signal can be easily "locked" respect to the driving clock. The periodic sensorgram thus can be easily detected even in the presence of high levels of additive uncorrelated disturbances and noise. The virtues of the scheme are visibly evident when the power spectrum of the SPR response and the disturbance are plotted as shown in the example of Figure 3.3. While noise and disturbance have broad spectra, the power of the sensorgram dissociation and association response cycles are concentrated at a single modulation frequency, thus showing as a spike in the spectrum that can be easily discriminated from the noise using a narrow band filter. Most of the noise and disturbance power falls outside this narrow band; hence, it is greatly rejected. This kind of signal-locking methodology offers a substantial improvement in the SNR of the SPR sensorgram. Noise rejection capability of such a SLFT scheme will be quantitatively analyzed in this and the following chapter. This scheme can be analyzed using two kinds of input signal considerations, small signal and large signal analysis.

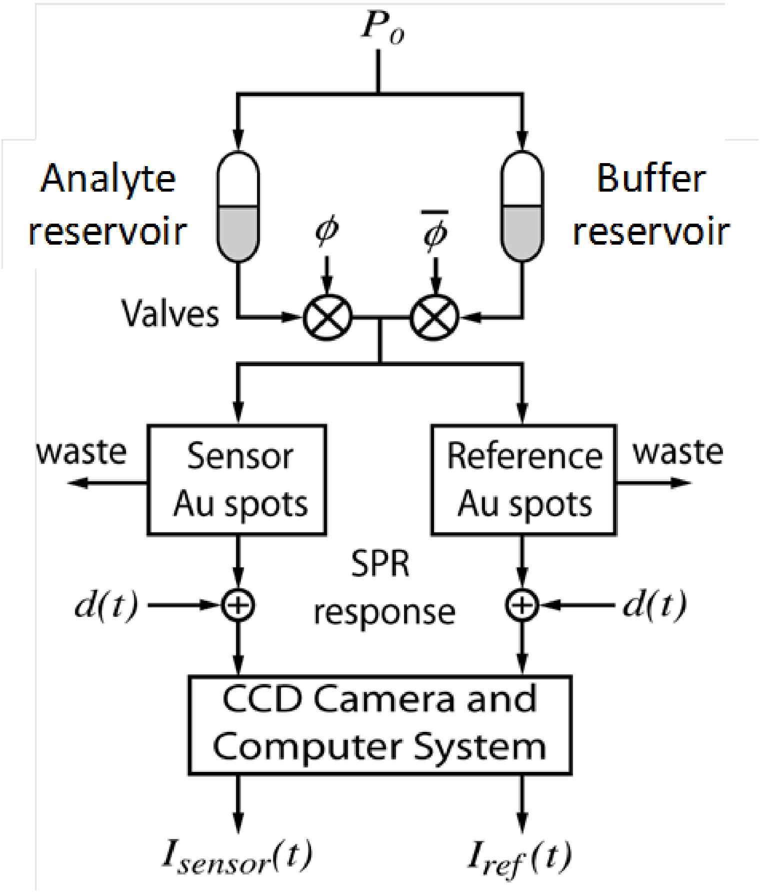

Figure 3.2. Schematics of SLFT-SPR detection system. The sensor input excitation is a periodic stream of analyte and buffer plugs controlled by clocks ϕ and $\overline{\phi}$. This produces periodic association and dissociation steps modulated at frequency f_ϕ which are easily separated from disturbances.

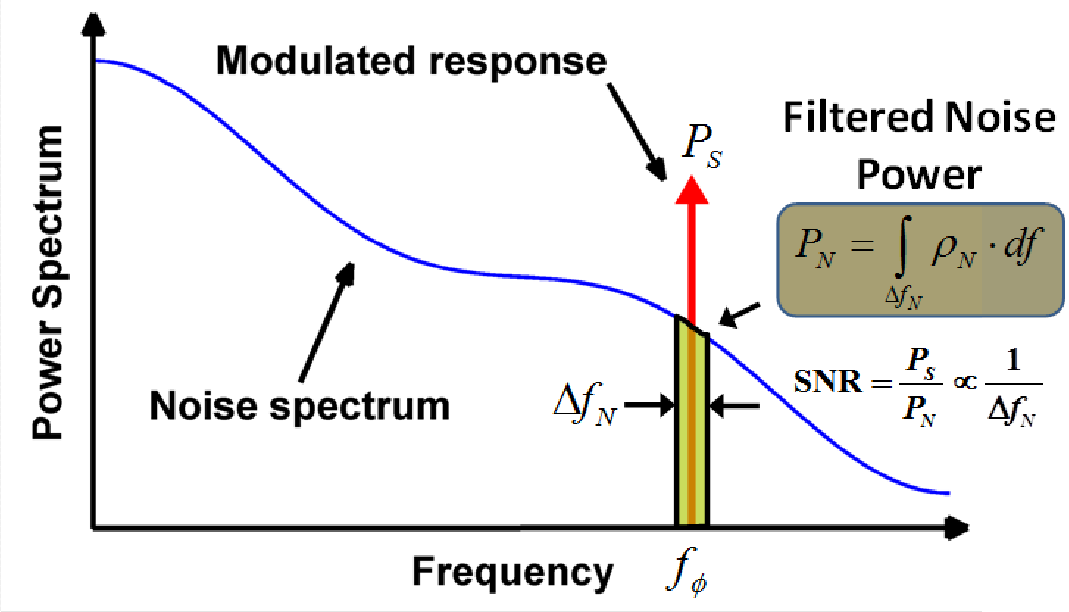

Figure 3.3. The power spectrum of the sensorgram versus frequency plot contains the narrowband response and broadband noise and disturbances. The modulated response can be discriminated from the broadband noise using a signal locking sharp bandpass filter, thus greatly rejecting the influence of out-of-band noise and disturbances.

3.1.1.1 Small-Signal Analysis

In order to utilize these signals effectively, we must first establish a relation between the excitation response and the kinetic constants. We can first set the clock frequency f_ϕ and record the sensorgram response. By repeating this procedure at different discrete modulation frequencies, one may obtain a relation between the excitation frequency and the sensorgram response. Since both excitation and response are periodic, they can be expanded as Fourier series. As shown in Figure 3.1, the relation between the fundamental terms of response and input series is the Fourier transfer function (TF) $H(j\omega)$ of the biochemical system given by

$$H(j\omega) = \frac{Y(j\omega)}{X(j\omega)} \tag{3.1}$$

where $X(j\omega)$ and $Y(j\omega)$ are complex phasors [2] of the input analyte excitation and filtered sensorgram output, respectively, and $\omega = 2\pi f_\phi$ is the excitation angular frequency. For small periodic input perturbations of the type

$$A(t) = A_0 + \Delta A(t) = A_0 + \sum_{n=1}^{\infty} \Delta A_n \sin(n \cdot \omega \cdot t) \tag{3.2}$$

with $|\Delta A(t)| \leq 0.1 \cdot A_0$, the sensorgram response is approximately proportional to the analyte-ligand complex which also has the form

$$C(t) = C_0 + \Delta C(t) = C_0 + \sum_{n=1}^{\infty} c_n \sin(n \cdot \omega \cdot t + \theta_n) \tag{3.3}$$

where C_0 is the equilibrium analyte-ligand complex concentration [1]. If the biochemical interaction is determined by Equation (1.6), the transfer function is directly related to the kinetic constants k_a and k_d, and it is obtained by direct substitution of Equations (3.2) and (3.3) into Equation (1.6), which reduces to

$$\begin{aligned}\frac{d\Delta C(t)}{dt} &= k_a \cdot (B_0\text{-}\Delta C(t)) \cdot \Delta A(t) \text{ - } (k_a \cdot A_0 + k_d) \cdot \Delta C(t) \\ &\approx k_a \cdot B_0 \cdot \Delta A(t) \text{ - } (k_a \cdot A_0 + k_d) \cdot \Delta C(t)\end{aligned} \tag{3.4}$$

The above equation is valid for corresponding small changes in the analyte-ligand complex such that $B_0 >> \Delta C(t)$. The reduced simplified Equation (2.4) is linear in $\Delta A(t)$ and its corresponding Fourier series components. The small-signal transfer function (TF) $H(j\omega)$ is easily obtained from Equation (3.4) by substitution of the time derivative with $j\omega$. The small-signal sensorgram TF at the fundamental component has the single pole behavior

$$\begin{aligned}H(j\omega) &= G_{SPR}\left(\frac{c_1}{\Delta A_1}\right)e^{j\theta_1} \\ &= G_{SPR}\frac{k_a \cdot B_0}{(k_a \cdot A_0 + k_d)} \cdot \frac{1}{(1 + j\omega/\omega_p)}\end{aligned} \tag{3.5}$$

with characteristic pole ω_p given by

$$\omega_p = 2\pi f_p = k_a \cdot A_0 + k_d \tag{3.6}$$

Therefore, we can measure the kinetic constants k_a and k_d by direct measurements of the small-signal transfer function and finding each TF pole for different A_0 analyte concentrations. This is the basis for the SLFT-SPR methodology. Since SLFT-SPR relies on the repetition of rapid association and dissociation cycles, the depletion of analyte in solution is much less severe than that for the conventional single-pulse technique; therefore, experimental flow conditions that are not subject to transport issues in the conventional single-pulse method are also sufficient for this technique.

3.1.1.2 Large-Signal Analysis

In the SLFT-SPR [1] measurement, it is advantageous to increase the excursion of the input analyte beyond $0.1 \cdot A_0$ because the magnitude of the corresponding sensorgram increases proportionally. For large analyte excursions, the analysis is more complex because Equation (1.6) differs for the association and dissociation cycles and input-output linearity of the Fourier components does not hold. In the large signal analysis, we assume the analyte excitation is a periodic square waveform of period T, amplitude A_0, and clock frequency $f_\phi = 1/T$. At low frequencies, the sensorgram is also square, but as the frequency increases, it becomes triangular, thus changing the Fourier coefficients of the response. We can account for the impact of the change in shape by calculating the Fourier series components of the sensorgram waveform. At steady state, C(0) = C(T); and we arrive at the following derivation

$$\text{a} - \text{b} = (\text{a} - \text{b} \cdot e^{-\beta_1}) \cdot e^{-\beta_2} \tag{3.7}$$

where $\text{a} = \left(\frac{k_a \cdot A \cdot B_0}{\alpha_1} \right)$, $\alpha_1 = k_a \cdot A + k_d$, $\alpha_2 = k_d$, $\beta_1 = \frac{\alpha_1 \cdot T}{2}$ and $\beta_2 = \frac{\alpha_2 \cdot T}{2}$. Solving Equation (3.7) for b, the steady-state solution can then be written as

$$C(t) = \begin{cases} \text{a}\left(1 - \left[\dfrac{1 - e^{-\beta_1}}{1 - e^{-(\beta_1 + \beta_2)}}\right] \cdot e^{-\alpha_1 \cdot t}\right) & , \ 0 \le t \le \dfrac{T}{2} \\ \text{a}\left(1 - \left[\dfrac{\left(1 - e^{-\beta_1}\right) \cdot e^{-\beta_1}}{1 - e^{-(\beta_1 + \beta_2)}}\right]\right) \cdot e^{-\alpha_2 \cdot (t - \frac{T}{2})} & , \ \dfrac{T}{2} \le t \le T \end{cases} \tag{3.8}$$

The first component of the complex Fourier series of Equation (3.8) for two limiting conditions as T→∞ (ω→0) and T→0 (ω→∞) are determined (Appendix A). The amplitude of the sinusoidal component is

$$c_1^{\infty} = \frac{2a}{\pi} \tag{3.9}$$

while the cosine amplitude is

$$c_1^{0} = -\frac{2\alpha_1\alpha_2 aT}{(\alpha_1 + \alpha_2)\pi^2} \tag{3.10}$$

With the amplitude from these two limiting cases, an approximation for the magnitude of the normalized large signal TF can be written as

$$\begin{gathered}\left\|T(j\omega)\right\| = \left\|\frac{H(j\omega)}{H(0)}\right\| \approx \left\|\frac{c_1^{0}(j\omega)}{c_1^{\infty}}\right\| = \\ \frac{2\alpha_1\alpha_2 aT}{(\alpha_1 + \alpha_2)\pi^2}\cdot\frac{\pi}{2a} = \frac{\alpha_1\alpha_2}{(\alpha_1 + \alpha_2)\pi\times f} = \frac{2\alpha_1\alpha_2}{(\alpha_1 + \alpha_2)\omega}\end{gathered} \tag{3.11}$$

At the pole frequency $f = f_p$, the magnitude of the normalized TF equals $1/\surd 2$; hence, the expression for the pole for large signal excitation is approximately

$$f_p \approx \frac{\sqrt{2}\cdot\alpha_1\alpha_2}{\pi(\alpha_1 + \alpha_2)} \tag{3.12}$$

This can be written finally in terms of k_a and k_d (sometimes referred to as k_{on} and k_{off}, respectively) as

$$f_p \approx \frac{\sqrt{2}\cdot(k_a\cdot A_0 + k_d)\cdot k_d}{\pi(k_a\cdot A_0 + 2k_d)} \tag{3.13}$$

Equation (3.13) provides a relation between the observed pole and the kinetic constants under the condition of large analyte square wave excitation. Note that this expression differs significantly from the small signal pole expression of Equation (3.6). In particular, Equation (3.13) includes the effects of saturation which develop for large A_0, making the pole approach $\surd 2\cdot k_d/\pi$.

3.1.2 Schematics of Measurement

In the following sections of this chapter, we discuss the schematics and testing of large-signal SLFT-SPR. Analysis for small-signal SLFT-SPR will be discussed in the following chapter. The large-signal SLFT-SPR analysis method is implemented using the set-up shown in the schematics of Figure 3.2. As described in Section 3.1.1, the biochemical system under test is driven by a periodic input excitation of analyte and buffer of a constant frequency f_ϕ specified by digital clocks ϕ and $\overline{\phi}$. The corresponding periodic association and dissociation cycles in response produce a highly correlated sensorgram of the same frequency which is then "locked" with respect to the driving clock. In order to have the response over the entire frequency spectrum, this technique thus requires the sweeping of the clock modulation frequency f_ϕ from low to a high frequency (f_ϕ typically should be higher than the pole frequency f_p but preferably lower than signal transmission pole frequency) and the generation of a stream of high-frequency plugs that are transported to SPR sensing and control surfaces. In order to create such short fast plugs, it is necessary to use microfluidic chips which permit the transport of time-dependent chemical signals with low dispersion [3]. Figure 3.4 shows a SPR microchip that has been fabricated for synthesis and testing of the large-signal SLFT-SPR method. The chip consists of two signal generators (multiplexers or MUX) each of which has three plug generators (one for each of analyte, buffer and regeneration) and two output flow channels which are lined by several SPR sensing and reference Au spots. Each three-valve flow MUX along with its connected output channel is dedicated for signal generation on the reference (control) and the bio-interaction sensing surface, respectively. The two-channel arrangement also facilitates the functionalization of the

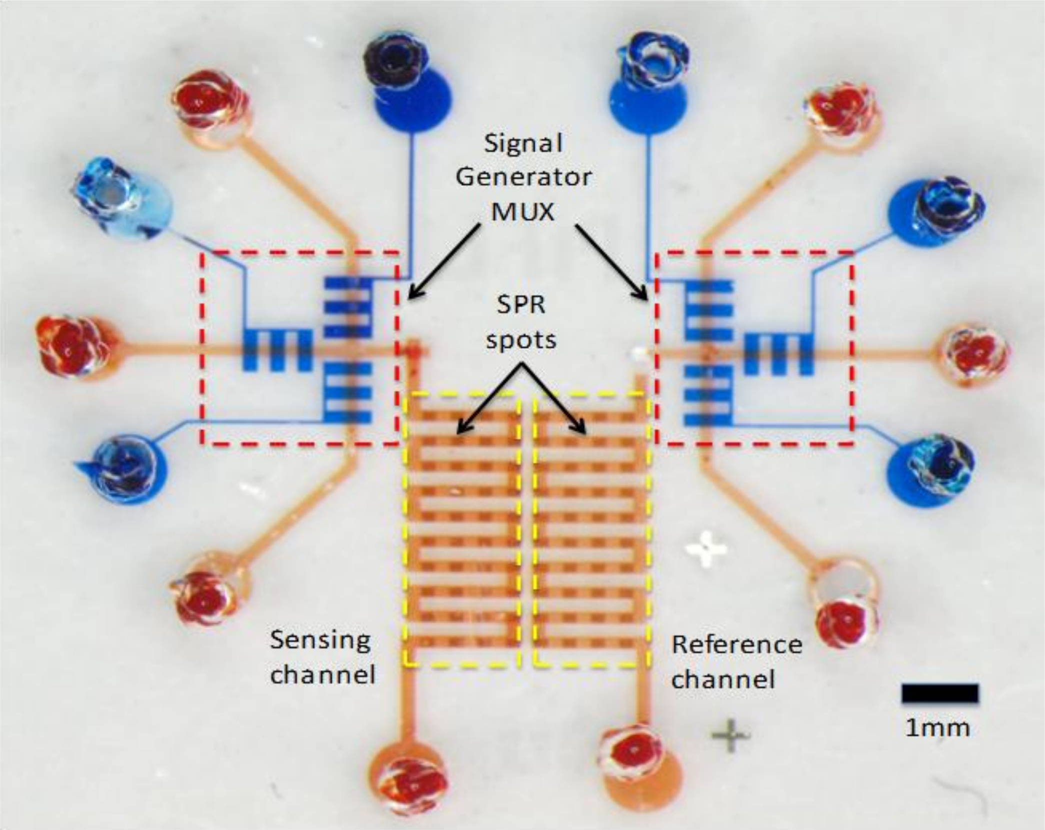

Figure 3.4. Photograph of large-signal SLFT-SPR microchip.

sensing and blocking of the reference sites simultaneously and separately. Two of the valves switch between pure buffer and analyte flows. The third valve is used for regeneration and cleaning of the sensor and reference surfaces. The analyte and buffer valves are driven by digital clock signals ϕ and $\overline{\phi}$, respectively, and pulsed at a specific frequency. The test chip of Figure 3.4 was fabricated using conventional two-level PDMS technology [4-6]. Details of the fabrication and Au surface modification have been discussed previously in sections 2.1.1.3 and 2.1.1.4.

3.2 Testing of Large-Signal SLFT-SPR

3.2.1 Experiments

The microfluidic chip is placed in the SPR mounting cell, with a refractive index matching fluid (R.I.=1.72) to couple the prism with glass substrate. Microfluidic connections are made to the valves and flow channels, and then the valves control lines are filled with water, due to the gas permeability of PDMS. The valves are actuated by a pressure system at 30 PSI controlled by a computer. Syringes containing analyte (CA-II), buffer (PBS), and regeneration solution (0.1% SDS in PBS) are pressurized as well with a constant source at 10 psi which corresponds to a flow velocity of 16 cm/s, sufficiently high (> 6.7 cm/s, calculated) to overcome transport limiting effects [7]. CA-II samples were prepared as follows. We first measure the dry CA-II on an analytical balance with a resolution of 0.1 mg. The dry CA-II is then added to an appropriate volume of the PBS running buffer to make our analyte solution, i.e., if we want a 100 μg/mL analyte solution (or 3.4 μM at 29 kDa MW for CA-II), we measure 1.0 ± 0.1 mg, and add that to 10 mL of buffer. We next measure the actual concentration in solution using a spectrophotometer

(GENSYS5, Thermo Scientific) at 280 nm. Reported values of the extinction coefficient for bovine CA-II range from 55,300-57,000 L/mol-cm [8,9]. Three different (measured) concentrations of CA-II were used, 2.3, 5.3, and 11 μM. Experiments are performed for each CA-II concentration by collecting the response from a single step input first, and then continuously running multiple cycles of a square wave input signal at different frequencies, swept from 2 mHz to 256 mHz. The sampling rate was 4 Hz for all experiments. Figure 3.5 shows an example eight frequency (2, 4, 8, 16, 32, 64, 128, and 256 mHz) input chemical signal coded in MATLAB. As we can see, this a relatively simple binary (on/off) digital signal, each on/off cycle of which has a particular frequency of oscillation. All frequency components are equally weighed (contains the same power in each frequency component) except for the lowest frequency component of 2 mHz which has twice the power of others. This is done deliberately to improve the detection of the lowest frequency component in frequency domain. Wasabi camera control software from Hamamatsu is used to analyze the collected data by selecting multiple sensing and reference spots in the image as discussed in previous chapter. After an experiment at a given concentration is completed, the channels are flushed with regeneration solution to clean the sensor surface.

3.2.2 Results

Kinetic constants were obtained using both a single-step method and the large-signal SLFT-SPR scheme. In all the data sets, the fixed imager intensity offset I_{offset} is first recorded at the beginning of the measurement and subtracted from all the recorded data. Each spot analyzed comprised approximately 1550 pixels on the CCD camera. In our

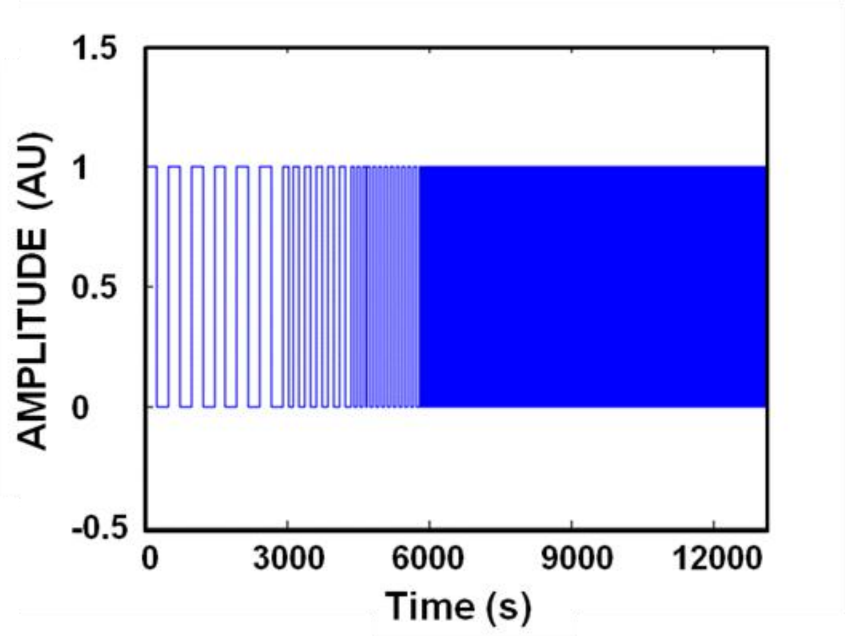

Figure 3.5. An example digital multifrequency binary input chemical signal encoded in MATLAB.

experiments, we observed a large discrepancy exists between the concentration prepared by weight and that measured in the spectrophotometer. This discrepancy can originate from several phenomena, including differences between weighted and active protein [7] concentration as well as various error sources of the scale and spectrophotometer. We believe our largest source of error originates from the uncertainty in the analyte concenetration.

3.2.2.1 SRM Response

For each concentration, a single-step experiment was first performed by flowing buffer for 5 minutes, CA-II for 5 minutes, and then buffer again for 5 minutes. After removing I_{offset} from the data, the signal from a reference spot, I_{ref}, was subtracted from a sensor spot, I_{sensor}, at the same distance downstream from the fluid control valves. This is needed to cancel the solvent bulk contribution s(t) of the analyte solution as compared to that of the buffer. The corrected responses from the single-step experiments are shown in Figure 3.6, along with the fits to the exponential solution

$$I(t) = I_0(1 - e^{-k_{obs}\cdot t}) \tag{3.14}$$

where k_{obs} is the observed rate constant for the association phase,

$$k_{obs} = k_a \cdot A_0 + k_d \tag{3.15}$$

The observed rate values were then plotted against the respective concentration values and a linear fit was used to determine k_a and k_d according to Equation (3.15). These values were found to be 6.5 x 10^3 1/M·s and 2.5 x 10^{-2} 1/s, respectively, ($R^2 = 0.974$) in reasonable agreement with published results [7].

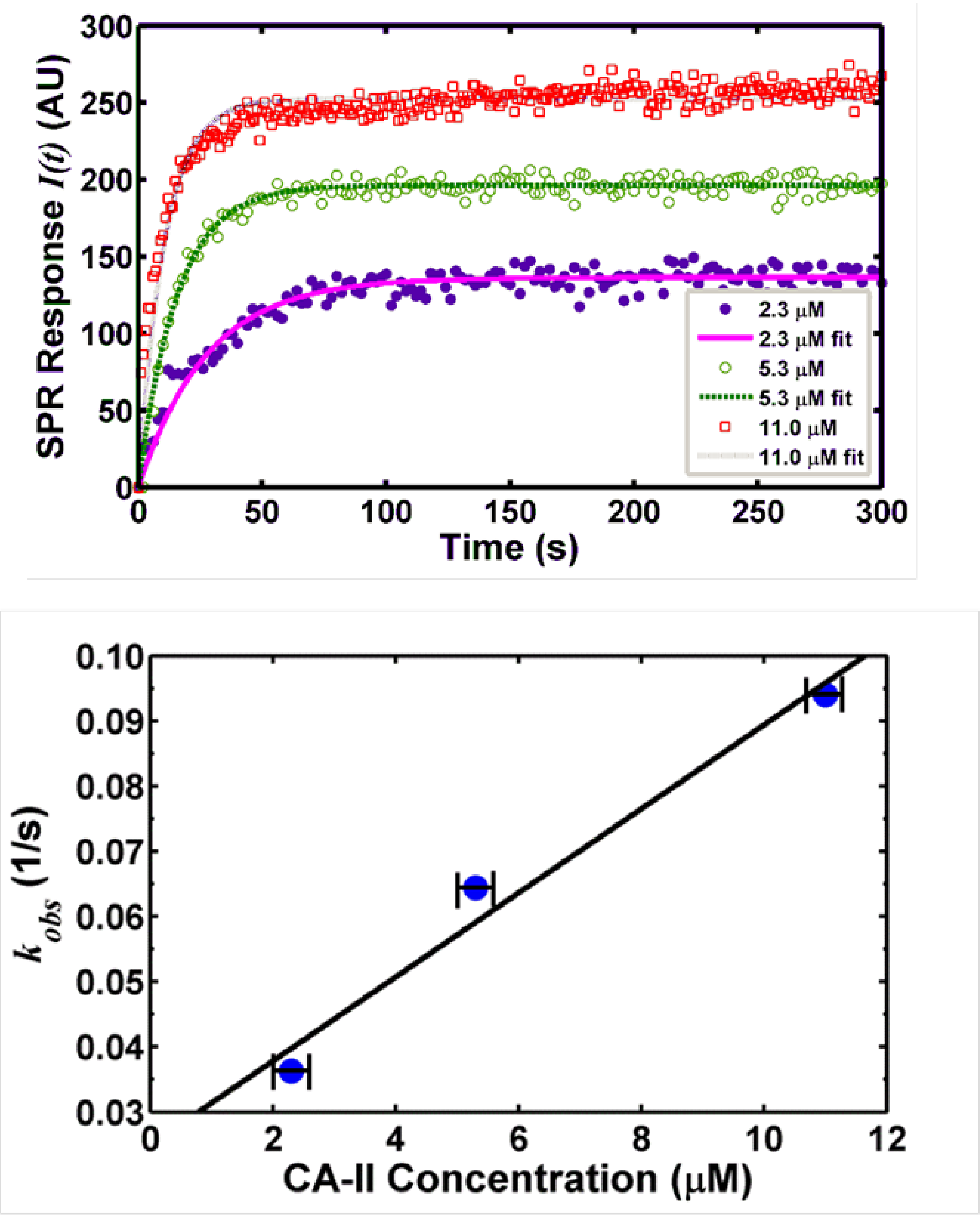

Figure 3.6. Plot of single step sensorgram response data for each concentration and the associated fit (top), and the resulting value for k_{obs} versus the respective concentration, and a linear fit used to find k_a and k_d (bottom).

3.2.2.2 SLFT-SPR Response

The continuous cycle intensity data were collected for each concentration at a discrete set of frequencies selected to give an even power distribution across the spectrum. The input frequencies of the digital input signal of Figure 3.5 and its output SPR waveform are shown in Figure 3.7. The frequencies began at 2 mHz and increased by doubling until 256 mHz was reached, keeping the time each frequency was applied constant. This was performed after the single-step data were collected so that the system was near steady state when the cycles started to avoid a long transition during the experiment. Fourier transform analysis is used to determine the magnitude of the sensorgram response intensity and normalized transfer function $||T(j\omega)||$ at the excitation frequencies from the magnitude of the measured power spectrum. $||T(j\omega)||$ is next plotted versus each excitation frequency as shown in the Bode plot of Figure 3.8. The pole frequency for each concentration was determined at the -3dB point. The experimental tail of the Bode plot at high frequencies differs from the single-pole behavior. We attribute this flattening of the experimental response to imperfect but not negligible reference cancellation of bulk signals which is independent of frequency. The k_a and k_d is determined from the SLFT-SPR analysis by fitting the pole values to Equation (3.13). They were found to be 9.4×10^3 1/M·s and 2.7×10^{-2} 1/s, respectively (R^2=0.968). These values match reasonably well with those determined with the single step method. The values determined by the large-signal SLFT-SPR method do differ slightly from reported values of k_a and k_d for the same model system, but the range of these values is very large among the different detection methods used. We attribute the difference in the values we obtained as due to the particular surface chemistry employed in this work.

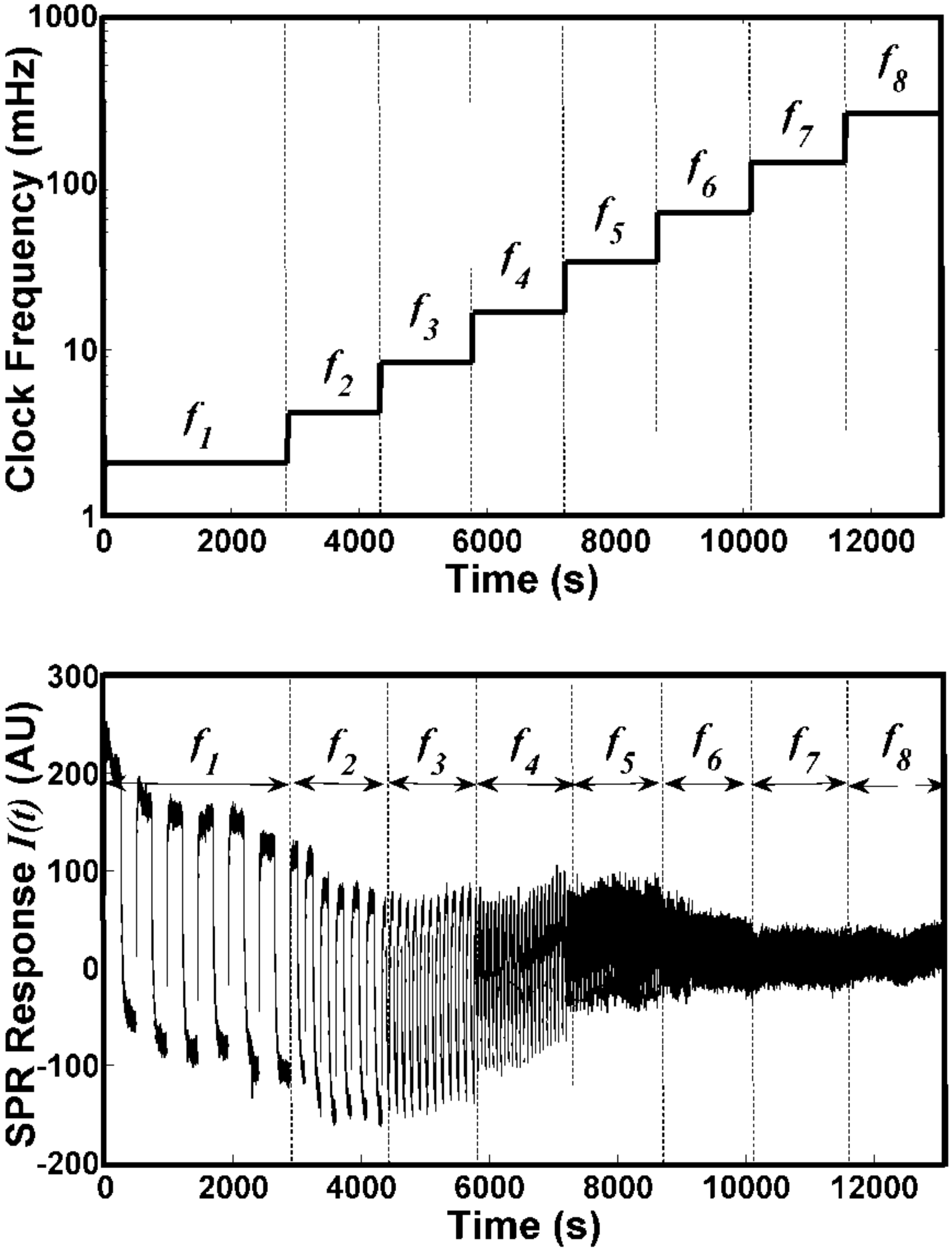

Figure 3.7. Plot of example input clock frequency sweep used for the FT-SPR measurement (top), and resulting SPR sensorgram waveform from the biochemical interaction system (bottom).

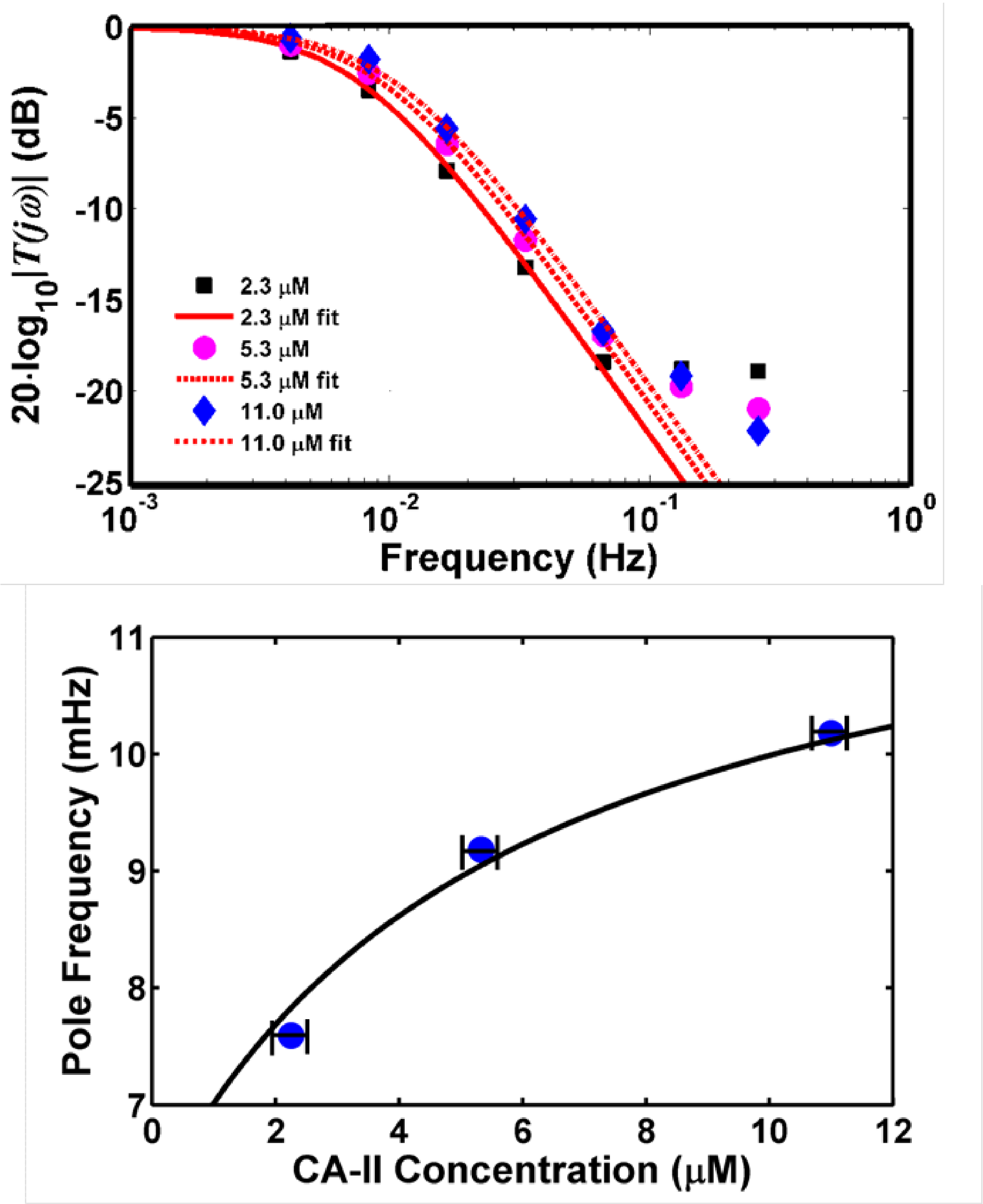

Figure 3.8. Plot of magnitude of the normalized transfer function T(jω) (bode plot) vs. frequency; the poor fit at the higher tail frequencies originates from imperfect cancellation of the bulk response (top), and the resulting pole frequencies vs. the respective CA-II input concentration (bottom).

3.2.2.3 SNR and Sensitivity Analysis

The signal-to-noise ratio (SNR) in decibels (dB) for the step-response measurement was computed from the ratio of the average power of the exponential fitted signal to the average power of the fit residual over the measurement period as shown below

$$\mathrm{SNR}_{\mathrm{step}} = 10 \cdot \log\left(\frac{\int_0^\tau I_{\mathrm{fit}}^2 \mathrm{d}t}{\int_0^\tau (I_{\mathrm{meas}} - I_{\mathrm{fit}})^2 \mathrm{d}t} \right) \tag{3.16}$$

The measured SNR for the step response method was 26 dB, meaning that the average power of the fitted exponential was 400 times larger than that of the noise and disturbances. The SNR for the SLFT measurement is calculated differently from that of the SRM. First, we recorded the noise and disturbance intensity signal of the SPR system under no input excitation for 30 minutes at a sampling frequency of 4 Hz. After subtraction of the initial offset, the intensity was normalized to the full scale of the imaging camera. We next computed the power spectral density of the normalized intensity signal measured in dB-full scale/Hz (or dB-fs/Hz). Because this is a random signal, the power spectrum was averaged over 10 equal duration 180-second recording cycles. This procedure produces a reasonably well-defined estimate of the disturbance and noise spectral density. We can now readily compare the relative power of the system noise and disturbances to the power spectrum of the SLFT-SPR signal (also in dB-fs/Hz) as shown in Figure 3.9 (top). Note that the power spectrum of the SLFT-SPR interaction signal is simply $||H(j\omega)||^2$ which is flat at low frequencies and displays a dual pole at fp. In contrast, the power spectrum of the noise and disturbance seems to be largely concentrated at the lower frequencies becoming flat at the higher frequencies. The SNR for this large-signal SLFT-SPR measurement is equal to the ratio of the two power spectrums, as shown in Figure 3.9 (bottom). Note that unlike the fixed SNR for the single-pulse step response method, the SNR of the SLFT-SPR technique increases and peaks at a specific frequency near the TF pole. In addition, the peak SNR is much higher for this technique than SRM by a factor of 20 dB or 100-fold better than that of the step response method.

3.3 Discussion and Summary

There are two reasons behind the observed SNR improvement in our results; (a) the measurement takes place in a region where the power density of the disturbances and noise is low and (b) the power spectrum of the disturbance is broad, hence only a small contribution of the disturbance and noise is present at the narrow excitation frequency. The major improvement in the SNR of the narrowband FT-SPR technique leads us to believe that it may be possible to directly detect small molecule binding on these surface. However, this improvement in SNR (100-fold) comes at the price of measurement times (~ 240 minutes), which is much longer than the conventional SRM of ~ 10 minutes.

Finally, we would like to state that in spite of the impressive SNR ratios, the large-signal SLFT-SPR technique does have practical limitations. First, in order to make a clean measurement, the modulator chip has to be able to produce sufficiently high frequency plugs to reach the TF pole region. Therefore, small distances between the chip valves and the sensing spots are required to minimize the plug dispersion. In addition, smaller noisier spots must be used in the chip. The technique also requires periodic

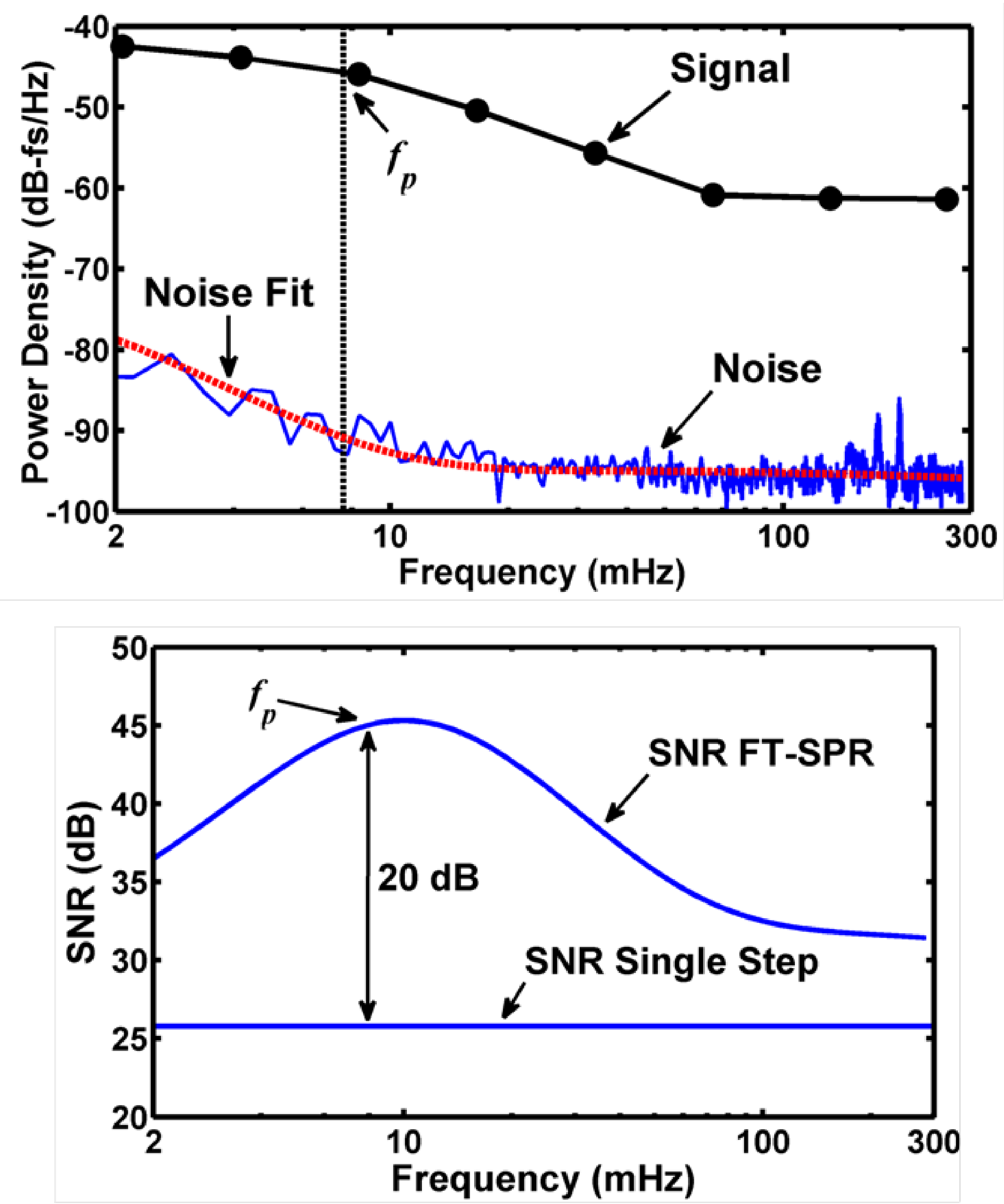

Figure 3.9. Plot of comparison of the power spectrum of the sensorgram signal (from the lowest applied concentration of CA-II) and the power spectrum of the system noise and disturbances with no excitation (top), and the signal-to-noise ratios (SNR) for the step response and FT-SPR methods (bottom). The SNR of the large-signal FT method is 20 dB higher than that of the single-step method. This translates to a 100-fold improvement in the SNR for the FT-SPR method.

excitation and a periodic response; therefore, it cannot handle irreversible reactions with strong associations and weak dissociation, but such reactions could be measured with the use of periodic regeneration cycles.

3.4 References

1. Williams, L.; Ghosh, T.; Mastrangelo, C. *Anal. Chem*., 2010, 82, 6025-6031.

2. Giancoli, D. In. *Physics for Scientists and Engineers*, Prentice-Hall: New Jersey, 1989.

3. Xie, Y.; Wang, Y.; Chen, L.; Mastrangelo, C. *Lab on a Chip,* 2008, 8, 779-785.

4. Azizi, F.; Mastrangelo, C. *Lab on a Chip*, 2008, 8, 907-912.

5. Chen, L.; Azizi, F.; Mastrangelo, C. *Lab on a Chip*, 2007, 7, 850-855.

6. Thorsen, T.; Maerkl, S. J.; Quake, S. *Science,* 2002, 239, 580-584.

7. Lahiri, J.; Isaacs, L.; Brzybowski, B.; Carbeck, J.; Whitesides, G. M. Langmuir, 1999, 15, 7186-7198.

8. Krishnamurthy, V. M.; Kaufman, G. K.; Urbach, A.. R.; Gitlin, I.; Gudiksen, K. L.; Weibel, D. B.; Whitesides, G. M. *Chem. Rev.*, 2008, 108, 946-1051.

9. Nyman, P. O.; Lindskog, S. *Biochim. Biophys. Acta*, 1964, 85, 141-151.

CHAPTER 4

METHOD 2: MULTISINE SLFT-SPR

4.1 Introduction

In this chapter, we discuss the synthesis and implementation of the small-signal analysis method of SLFT-SPR introduced in section 3.1.1.2. We start by introducing the background and the choice of a multifrequency small signal for our SPR measurements. This is followed by discussion on the small-signal SLFT-SPR chip and the input multisine small signal and results section. We will compare the results with those of SRM and large-signal SLFT-SPR interrogated in the previous chapter and discuss the improvements offered by this scheme. Finally, we conclude the chapter with a discussion and future scope of the work.

4.1.1 Multisine: A Test Small-Signal

As demonstrated in the earlier chapter, at a given frequency, the functionalized sensing and reference spots can be excited by introducing a binary digital (on/off) excitation signal in a flow cell using simple flow multiplexers. The TF and its characteristic pole are then obtained experimentally from a sequence of measurements at several frequencies. While these measurements are straight forward, they require considerably longer measurement times than those of the single pulse technique. We can,

Certain portions of this chapter are reproduced by permission of The Royal Society of Chemistry from the article "Label-free detection of protein binding with multisine SPR microchips", Ghosh, T.; Williams, L.; Mastrangelo, C. *Lab on a Chip*, 2011, 11, 4194-4199. http://pubs.rsc.org/en/content/articlelanding/2011/lc/c1lc20260j#!divAbstract.

however, reduce the measurement time dramatically if we use a test signal that has multiple frequencies. In this section, we will discuss the theory and practicality of one such signal.

The choice of input excitation signal is critical in determining the speed and accuracy with which the response of a system is obtained [1,2]. Multifrequency input test signals are commonly used for estimation of transfer functions. These test signals have a well-defined spectrum and hence are useful to determine spectral measurements at several frequencies simultaneously in a time-efficient manner. In this paper, we utilize an analyte excitation scheme that employs multisine waveforms s(t) of the type

$$s(t) = A_{avg} + \sum_{i=1}^{N} A_i \cos(\omega_i t + \theta_i)$$

(4.1) where N is the number of frequency components. If we select the frequencies such that $\omega_i = k.\omega_o$ where k is an integer, the multisine discrete frequencies are all contained within a single cycle of the lowest component, and the measurement interval corresponds of a few periods of ω_1. The practical generation of a synthetic multisine signal requires careful consideration of component harmonics, their amplitude, and relative phases indicated in Equation (4.1) by θ_i. The phases are selected to minimize the waveform crest factor C [1,2] where

$$C = \frac{|s|_{peak}}{s_{rms}} \tag{4.2}$$

which is equal to the peak to root-mean-square average ratio. For a single sinusoid, the crest factor is $2^{1/2}$. For a multisine, the crest factor is generally higher. A low crest factor is desirable because it avoids the presence of exceedingly large peaks in the waveform and reduces the resolution requirements for waveform generation. For example, a commonly used low crest factor multisine is the Schroeder multisine [2,3] with quadratically weighted phases. Figure 4.1 shows a comparison of an equal phase 10-component multisine ($\theta_i=0$) and the Schroeder multisine ($\theta_i = \pi \cdot i^2/N$). Both waveforms have the same Fourier power spectrum, but the Schroeder waveform is much easier to generate. The Schroeder scheme is not the only low crest phase configuration. One may also select the phases via numerical minimization of the crest factor.

4.1.2 Schematics of Measurement

Figure 4.2 shows the schematic of the spectral technique using the multisine analyte test signal. The spectral content of the signal permits the simultaneous measurement of the transfer function at multiple frequencies. If this input analyte excitation has equally weighed spectral components, after interaction with the functionalized sensing spots, the SPR sensorgram will be attenuated for frequencies larger than the pole frequency of Equation 3.5, thus shaping the sensorgram spectrum. The entire measurement can be done in a few cycles of the lowest multisine component, thus significantly reducing the measurement time compared to the frequency sweep scheme [4]. A major consideration in the multisine scheme is that the multisine is an analog signal; therefore, its generation requires a more complex microfluidic chemical signal generator [5]. We fabricated and tested the chip-based multisine synthesis in the SPR microchip system of Figure 4.3. The chip consists of two high-frequency chemical pulse coded modulators of the type discussed in [6] connected to flow channels that are lined by functionalized SPR gold sensing and reference spots. The chip is implemented using conventional two-level

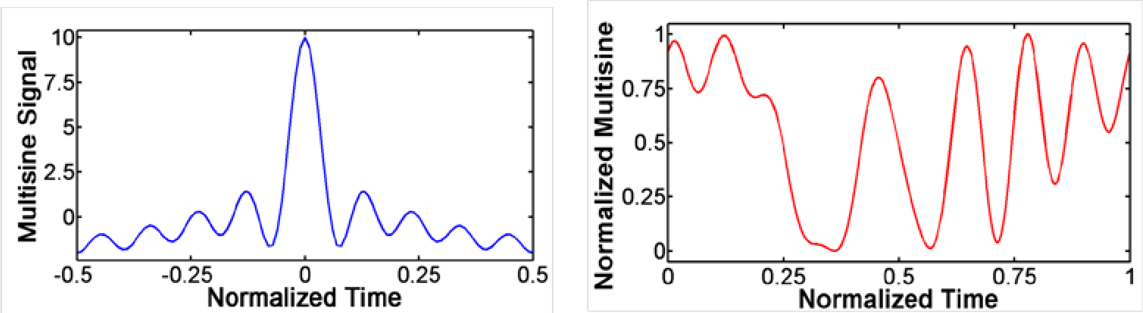

Figure 4.1. Plot of 10-component multisine with zero phase (left), and 10 component multisine with quadratic phase (right).

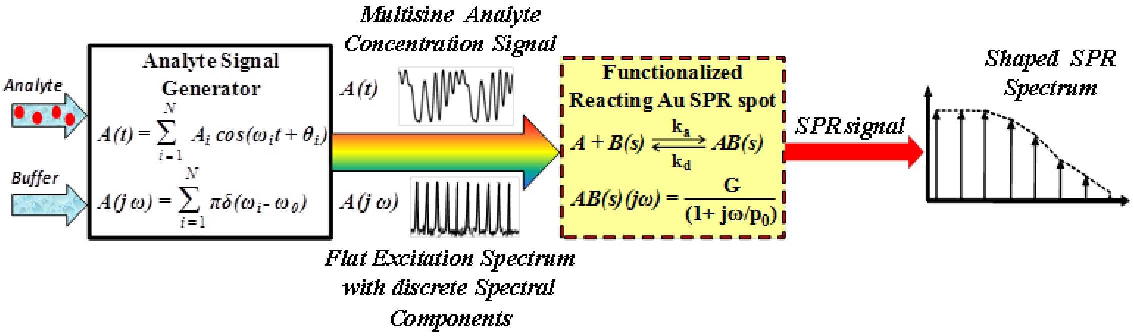

Figure 4.2. Schematics of the multisine chip. The response spectrum at multiple frequencies is measured simultaneously.

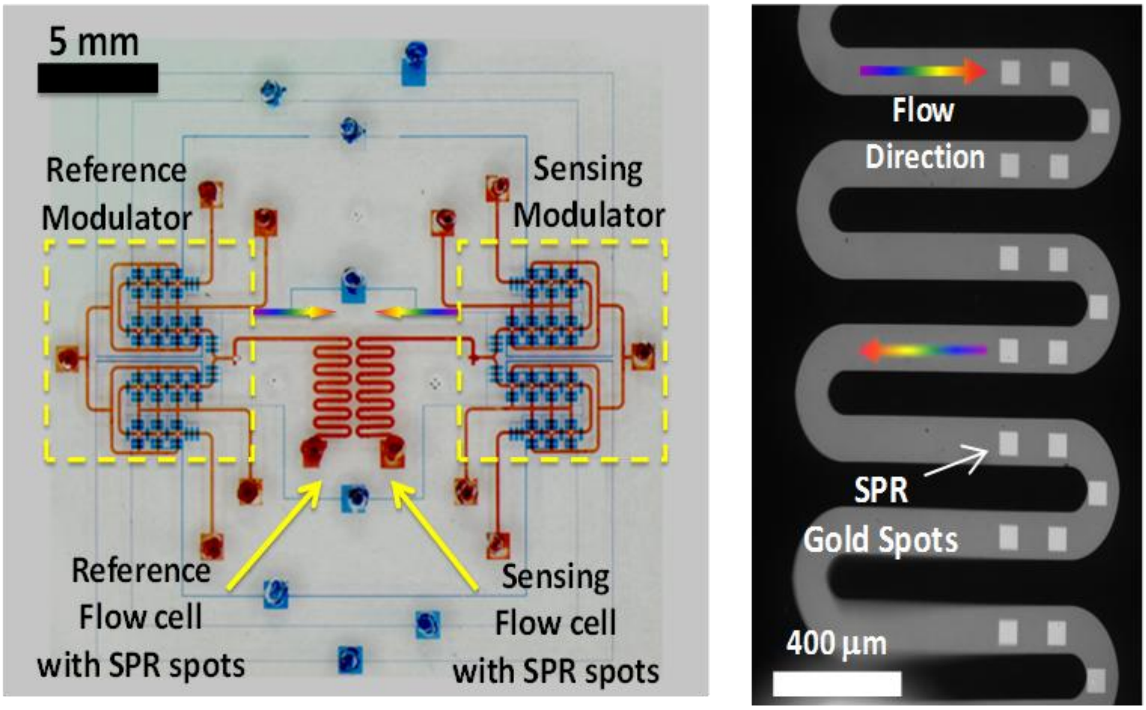

Figure 4.3. Picture of dual-channel multisine SPR chip (left), and close-up of a flow channel lined by SPR gold spots (right).

PDMS technology [6,7].

4.2 Testing of Small-Signal SLFT-SPR

4.2.1 Experiments

The SPR multisine chip is mounted onto a cell and coupled to the prism using refractive index matching fluid. Post microfluidic connections to flow channels and valves, the valve control lines are filled with water to displace the air with water in the valves due to gas permeable properties of PDMS. Phosphate-buffered saline (5mM sodium phosphate, pH 7.4) was used as running buffer. The valves are actuated by pressure of 28 PSI while the analyte (CA II) and buffer (PBS) are pressurized by 8.7 psi and 7 psi, respectively. The reservoir pressure of analyte and buffer correspond to a flow velocity of approximately 14 and 11 cm/s in output channels, respectively. The final velocity of analyte signal plug is thus sufficient to overcome mass transport effects [4]. The CA II samples were prepared using the following procedure. First, dry CA II powder was dissolved in the running buffer solution. Next, we measure the actual concentration in solution using a Spectrophotometer at a wavelength of 280 nm. Reported values for the extinction coifficient (a_{280}) for bovine CA II range from 55300 to 57000 L/mole-cm [8,9]. The protein concentration (*C*) is then given by the relation C (mole/L) = $A_{280}/(a_{280}\cdot b)$, where A_{280} is the value of absorbance at 280 nm and *b* being optical path length (1 cm for the given photometer). Three different concentrations (A_0) of 5.2, 10.4, and 15.6 µM were used for the separate multisine excitation experiments, consisting of seven frequency components ranging from 2 mHz to 64 mHz. The sampling rate was kept constant at ~5.7 Hz for all the runs. Wasabi camera control software integrated with the Hamamatsu EMCCD camera was used for analyzing the collected data. The mean intensity I(t) of the sensing and reference gold spots (700 pixels) for all the frames were extracted using this software followed by its Fourier transform analysis in MATLAB. The channels were flushed with regeneration solution (0.1% SDS in running buffer) between the runs.

4.2.2 Results

The kinetic constants k_a and k_d for this analyte-ligand pair were obtained by plotting the observed pole frequencies ($p = 2\pi f_p$) obtained from the Bode plot of the transfer function $H(j\omega)$ for the three different concentrations of the analyte. The term f_p here refers to the -3dB point of the transfer function plots in the frequency (Hz) domain. In all the data sets, there exists fixed imager intensity I_{offset} for all the imaging gold spots. This is first recorded at the beginning of the experiment and later on substracted from the measured signals to bring the baseline of the extracted signal to zero. The signal from the reference spots (I_{ref}) is then substracted from that of the sensor spots (I_{sensor}) to obtain reference and sensor signals for further processing. The reference-sensor spot pairs are approximately at the same distance downstream from the either modulators and substraction of their signals ensure elimination of the signal component from bulk response of analyte. The corrected time-domain responses from the multisine experiments then follow the simple relation $I(t) = I_0 \cdot s(t)$ where I_0 is the proportionality factor, s(t) being the test signal in analyte.

4.2.2.1 Nonreactive Multisine

In this chip, we first tested the proper generation and sensing of the multisine test signal using a 10% ethanol solution in PBS buffer as analyte. Figure 4.4 shows the time-domain response observed on a bare gold spot for a multisine signal consisting of five discrete frequency components of {10, 20, 50, 100, 200} mHz with corresponding phases of {0, 0, π, 0, π}, generated by the two MPMs at a plug rate of 40 plugs/sec. This is equivalent to a single 28-level digitized output every 0.7 seconds. The multisine crest factor is 2.1. Note that the analyte solution does not react with these nonfunctionalized gold spots; hence, the SPR response corresponds to the multisine spectrum of the test signal. This time-domain signal does not look particularly periodic, but when we calculate the power spectrum, we can clearly see the discrete frequency components of roughly the same power, demonstrated in Figure 4.5.

4.2.2.2 Biochemical Multisine

Next, we tested the feasibility of this spectral method for characterizing the biochemical reaction using functionalized sensor and passivated reference gold spots. A test multisine signal with minimized crest factor comprising equally weighed seven binary weigthed frequency components {1, 2, 4, 8, 16, 32, 64} mHz and corresponding phases {0, 2/3π, 5/3π, 5/3π, 5/3π, 5/3π, 0} was generated by the two MPMs. A time-domain plot of this analog signal is shown in Figure 4.6. The multisine waveform has a crest factor of 2.2. The average flow velocity is about 10 cm/s, which is sufficiently high to overcome mass transport effects [10]. The duration of this multisine run was ~17 minutes, corresponding to an input excitation synthesized with 40,000 plugs. Figure 4.7

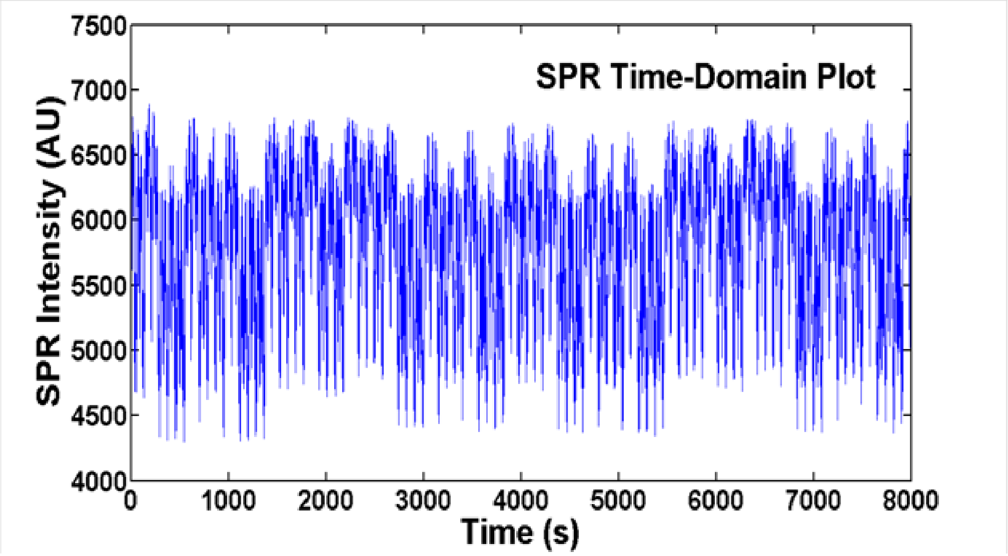

Figure 4.4. Time domain SPR signal recorded on bare Au spot using a of 5-component ethanol/PBS multisine.

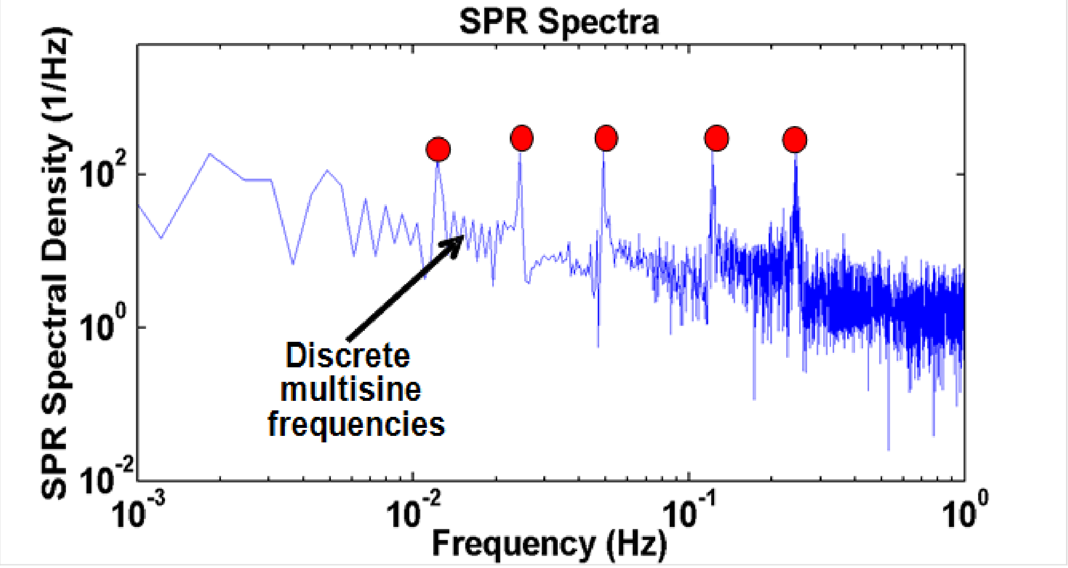

Figure 4.5. Spectral density of the response signal showing the 5 discrete frequency components.

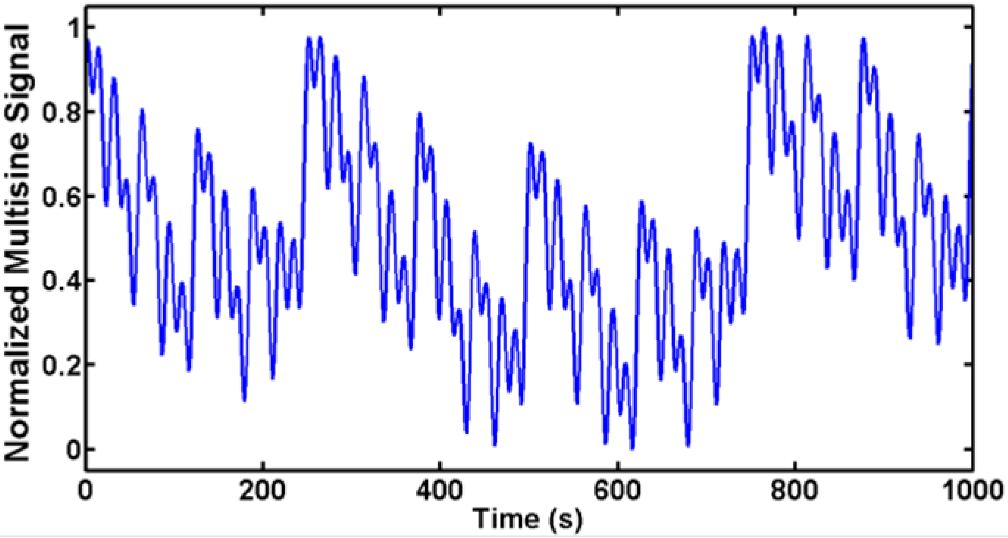

Figure 4.6. A 7-component multisine analyte waveform used for the SPR binding experiments.

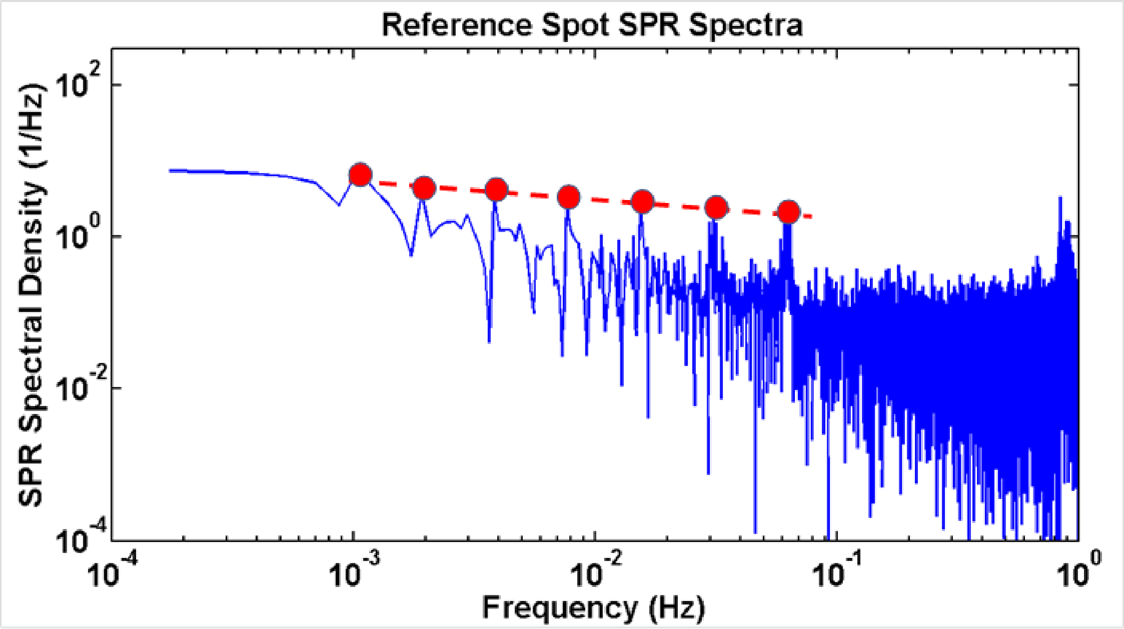

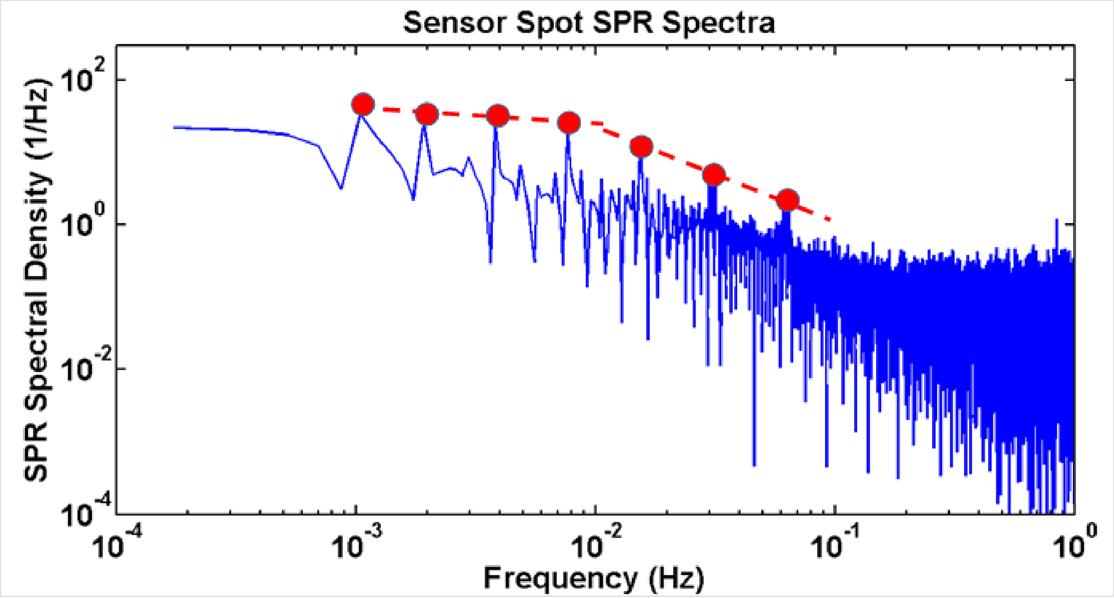

Figure 4.7. Plot of SPR spectrum of 7-component multisine on reference (top), and of sensor spots for analyte concentration of 10.4 μM (bottom). Note that the sensor spot response is shaped by the pole of the reaction.

shows the comparison of the SPR spectra under the multisine excitation of Figure 4.6 for analyte concentration of 10.4 μM. We can clearly see the discrete frequency peaks in the spectra. The Fourier spectral density of the response from the nonreacting reference surface is relatively flat (expected for a signal with components of equal weight), while the spectrum at the reactive sensor surface is attenuated at frequencies higher than the pole frequency, thus shaping the spectra expected from the single pole roll-off behavior of the TF. The magnitude of the transfer function is next plotted versus the frequency to obtain a bode plot for different analyte concentrations, as shown in the top of Figure 4.8. The values of frequencies obtained from the -3 dB points for these three concentrations are then plotted versus their respective average concentrations. As discussed before, the pole frequency p follows a linear relation (y = mx + c) with the analyte concentration; thus, one can extract the kinetic constants k_a and k_d from the slope 'm' and y-intercept 'c' of the linear fit, respectively, as shown in the bottom of Figure 4.8. The values for k_a and k_d from this fit are found to be 9.5×10^3 1/(M.s) and 6.2×10^{-2} 1/s, respectively. These values match reasonably well with those obtained in our previous sweeping spectral scheme.

4.2.2.3 SNR and Comparative Study

Note that the noise floor of Figure 4.7 for all the components is about ten times lower than each of the frequency peaks; hence, the response due to the input excitation signal can be clearly discriminated from the noise. The signal-to-noise ratio (SNR) for this multisine measurement is about 32 dB, corresponding to a minimum detectable protein concentration of 250 nM. The noise floor is about 7 dB higher (2.5X) than that observed

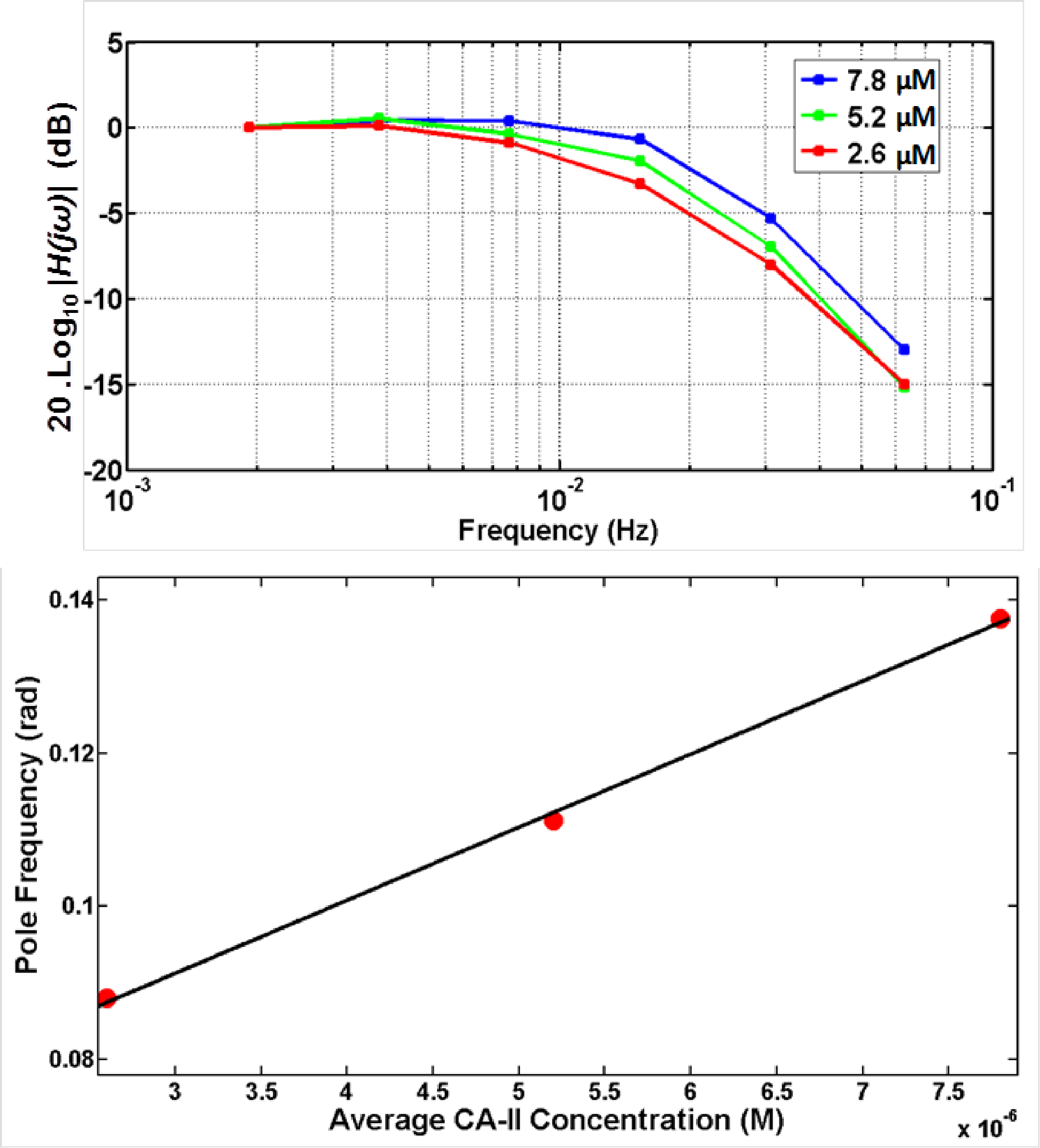

Figure 4.8. Plot of normalized bode plot of observed transfer function at three different average concentrations (top), and pole frequency vs analyte concentration (bottom).

in the single step-response method reported previously, while the overall measurement time is twice as long as required by the SRM. Table 4.1 shows a comparison of the resolution, measurement time, SNR, and system complexity for four different techniques: SRM, repeated SRM (calculated reolution ~ $N^{-0.5}$), periodic large-signal SLFT-SPR, and the multisine method.

4.3 Discussion and Summary

We have thus demonstrated a multisine Fourier-domain SLFT-SPR method for the measurement of binding constants of an analyte-ligand pair within a microfluidic environment using SPR as the detection technology. Compared to the conventional SRM, the multisine-SPR methodology provides cleaner measurement of parameters with higher SNR in about twice the time required by the conventional SRM method. This sort of measurement scheme can thus be used as a practical input SPR signal in analyte to

Table 4.1 Comparison of Different SPR Techniques

TECHNIQUE	**SRM**	**Repeated SRM(calc.)**	**Periodic Fourier**	**Multisine**
Resolution (RIU)	10^{-5}	7×10^{-6}	8.9×10^{-7}	4×10^{-6}
Time (min)	10	20	240	17
SNR (dB)	25	28	45	32
Complexity	simple	simple	medium	complex

recover the kinetics of its ligand recognition with higher resolution of detection and acceptable experimental time duration.

4.4 References

1. Rees, D.; Jones, D.; and Evans, D. *IEEE Conference on Instrumentation and Measurement Technology*, 1992, 174-179.

2. Godfrey, K. *Pertubation Signals for System Identication: Chapter 12*. Prentice Hall International Limited, UK, 1993, 348-372.

3. Schroeder, M. *IEEE Transactions on Information Theory*, 1970, 85-89

4. Williams, L.; Ghosh, T.; Mastrangelo, C. *Anal. Chem.,* 2010, 82, 6025-6031.

5. Xie, Y.; Mastrangelo, C. *Lab on a Chip*, 2008, 8, 779-785.

6. Azizi, F.; Mastrangelo, C. *Lab on a Chip*, 2008, 8, 907-912.

7. Thorsen, T.; Maerkl, S. J.; Quake, S. *Science,* 2002, 239, 580-584.

8. Krishnamurthy, V. M.; Kaufman, G. K.; Urbach, A.. R.; Gitlin, I.; Gudiksen, K. L.; Weibel, D. B.; Whitesides, G. M. *Chem. Rev*., 2008, 108, 946-1051.

9. Nyman, P. O.; Lindskog, S. *Biochim. Biophys. Acta*, 1964, 85, 141-151.

10. Lahiri, J.; Isaacs, L.; Brzybowski, B.; Carbeck, J.; Whitesides, G. M. *Langmuir*, 1999, 15, 7186-7198.

CHAPTER 5

METHOD 3: DUAL-SLOPE SPR

5.1 Introduction and Theory

In this chapter, we introduce a new signal processing method for faster detection of analyte-ligand binding. We first discuss the theory and basic principle underlining this fast measurement scheme called Dual-slope SPR. This is followed by the schematics of this measurement scheme and the fabricated SPR chip used for the dual-slope measurements of the biochemical reaction sensorgram. This will be followed by a results section where we will discuss the experiments and analyze the kinetic parameters obtained from the conventional SRM and Dual-slope SPR outputs. We next compare the results and verify the accuracy and viability of this technique. Finally, we conclude the chapter with a discussion on SNR of this method, drawbacks, and future scope of the work.

5.1.1 Fast Detection Schemes

The new Dual slope SPR technique provides a faster means for the measurement of the reaction kinetics. This is aimed at addressing the intrinsically slow nature of SRM, as discussed previously in Section 1.4.1.2. This new scheme utilizes rapid slope-based

Certain portions of this chapter are reproduced by permission of The Royal Society of Chemistry from the article "Fast measurement of binding kinetics with dual slope SPR microchips", Ghosh, T.; Mastrangelo, C. *Analyst*, 2012, 137, 2381-2385. http://pubs.rsc.org/en/content/articlelanding/2012/an/c2an35045a#!divAbstract.

measurements and it separates association and dissociation half reaction measurements at two separate reaction sites. As we shall see later, this scheme can speed up the detection times of the biochemical reactions by an order or more.

5.1.1.1 Dual-Slope SPR

In conventional SRM, Equations [1.8] and [1.9] are fitted to the experimental sensorgram to determine k_a and k_d. This sometimes results in a long measurement cycle; information, however, can be obtained in a much shorter time from the association and dissociation initial slopes [1] as follows. Differentiating Equation (1.8) with respect to time *t* gives

$$S_A = \lim_{t\to 0} \frac{dI_A(t)}{dt} = G_{SPR} \cdot k_a[A][B_o] = K_{SPR} \cdot k_d[A] \tag{5.1}$$

where S_A is the associative slope and K_{SPR} is a constant of proportional (since maximum surface concentration of ligand B_0 is constant through the detection process). At a given flow rate, the associative slope is thus linearly proportional to the analyte concentration [A]. Similarly, from Equation (1.9), subsequent differentiation yields

$$S_D = \lim_{t\to 0} \frac{dI_D(t)}{dt} = -G_{SPR} \cdot k_d[AB_d] \tag{5.2}$$

S_D being the dissociative slope. In order to extract k_a and k_d from Equations (5.1) and (5.2), we need to eliminate the constant terms. This can be done by deliberately reacting the species to equilibrium prior to the dissociation phase. Since a high analyte concentration ensures rapid surface saturation, we can use a high analyte concentration $[A_{RE}]$ to achieve a rapid complex equilibrium level $[AB_{RE}]$ with corresponding SPR intensity I_{RE} given by

$$I_{RE} = G_{SPR} \cdot [AB_{RE}] = \frac{K_{SPR} \cdot k_a \cdot [A_{RE}]}{k_a [A_{RE}] + k_d} \tag{5.3}$$

Rearranging the terms in Equations (5.1), (5.2), and (5.3), we can eliminate G_{SPR} and K_{SPR}. Since [A] and $[A_{RE}]$ are both known, and I_{RE} is easily extracted from the sensorgram, k_a and k_d can then be written as

$$k_d = -\frac{S_D}{I_{RE}} \tag{5.4}$$

and

$$k_a = \frac{S_A \cdot [A_{RE}] + S_D \cdot [A]}{I_{RE} \cdot [A_{RE}][A]} \tag{5.5}$$

Therefore, the kinetic constants can be determined from a measurement of the association slope with analyte concentration [A] and a second measurement of the dissociation slope with predissociation equilibrium achieved with analyte concentration $[A_{RE}]$. It should be noted that similar to a single cycle of association and dissociation in a conventional step response cycle, the dual slope technique estimates a single set of k_a and k_d for one set of [A] and $[A_{RE}]$.

5.1.2 Principles of Measurement

As we have seen in section 5.1.1.1, three independent parameters, namely the association and dissociation slopes of the sensorgrams S_A and S_D and predissociation equilibrium intensity I_{RE}, require to be extracted from the SPR response at fixed analyte concentrations of [A] and $[A_{RE}]$ to estimate one set of kinetic parameters k_{on} and k_{off}. The analyte signal is a binary on/off signal where analyte is tuned on during associative measurement step and turned off (pure buffer) for the dissociative step similar to that used in the conventional SRM scheme. As shown in Figure 5.1, parameters S_A, S_D and I_{RE} are determined from measurements at two identical but separate functionalized surface sites producing two distinct sensorgrams. At the association site, the functionalized surface is exposed to a brief positive association slope S_A measurement step by exposing the surface to analyte of concentration [A], followed by a brief regeneration step and subsequent short buffer wash. At the dissociation site, the surface is exposed to a solution of high analyte concentration [A_{RE}], quickly producing the pre-dissociation equilibrium level I_{RE}. The analyte solution at the dissociation site, [A_{RE}], has a much higher magnitude than [A] in order to reach rapid equilibrium. The rapid equilibrium step is followed by a brief negative dissociation slope S_D measurement in pure buffer. Both chemical excitation sequences are repeated multiple times to produce measurements of progressively improved quality.

The associative and dissociative phases of the biochemical reaction are made independent of each other to reduce the measurement time. In addition, the linearity assumptions of the dual-slope scheme holds true for first few seconds of the analyte and buffer introduction. Thus, the time required for the slope measurement is short, also in the order of few seconds, making the overall process of detection and sensing is fast. The minimum measurement time is limited only by the amount of noise present in the system. Generally speaking, the slope measurement time is much less than that required by the full step response. In this report, we demonstrate a measurement realized 10-fold faster than the SRM technique.

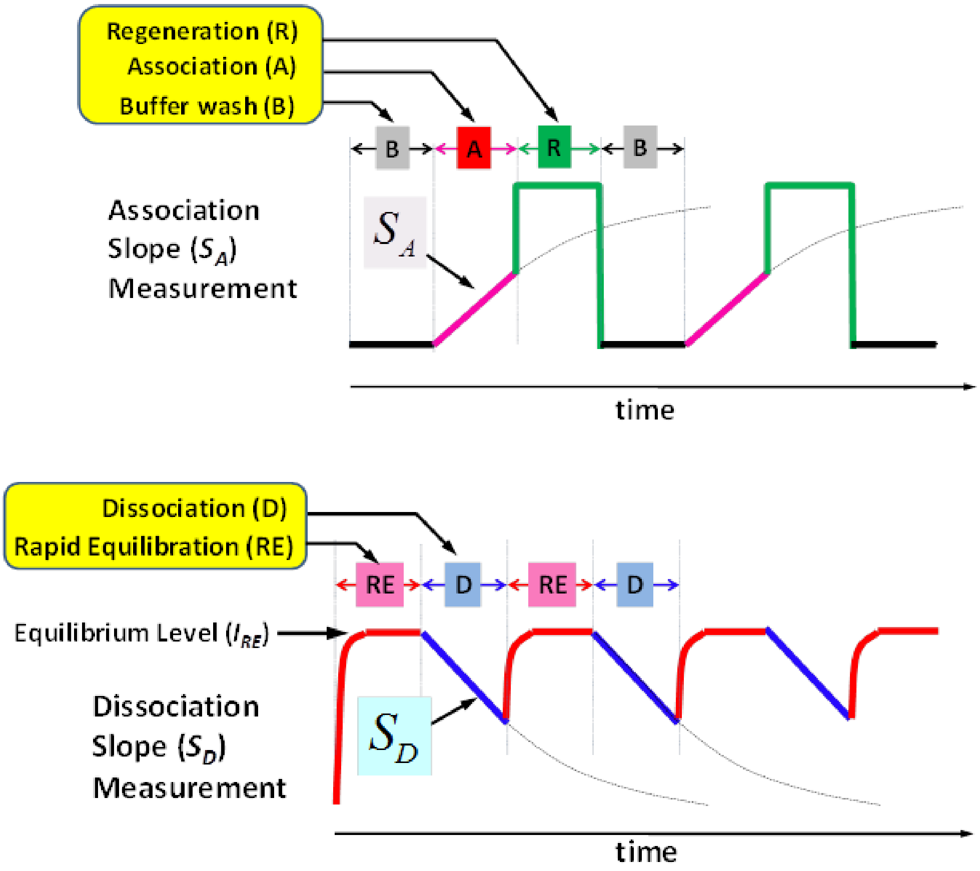

Figure 5.1. Basic principle used in the new fast dual-slope SPR technique. Two identical functionalized sites are exposed to different sequences of analyte, buffer, predissociation rapid equilibrium, and regeneration solutions. The association and dissociation constants are obtained from the two decoupled slopes S_A, S_D, and the equilibrium sensorgram intensity level I_{RE}.

5.1.3 Schematics of Measurement

In order to utilize the dual-slope technique, we need to introduce short flow cycles with steep chemical gradients. Such flow switching profiles can only be achieved in microfluidic environments which exhibit low dispersive mixing [2]. Figure 5.2 shows a schematic of a dual-slope SPR chip. The experiments and data acquisition are carried out in two separate dedicated chambers. The association chamber performs the association half reaction using two gold sensor spots (sensor + control) and three microvalves, each for the flow control of buffer, analyte, and regeneration solutions. The dissociative chamber utilizes two gold spots and two microvalves each of which control the flow of analyte and regeneration solutions. The dual-slope SPR scheme was implemented using a conventional two-level PDMS microchip [3,4]. Figure 5.3 shows an image of the fabricated PDMS chip. It consists of two separate microfluidic chambers for associative and dissociative half reactions, respectively, each of which is connected to three pressure-driven input sources controlled by separate microvalves and two output channels. The two output channels in each chamber are lined by gold sensor spots which record the sensor and control sensorgrams, respectively.

5.2 Testing of Dual-Slope SPR

5.2.1 Experiments

The chip-on-substrate is placed onto a SPR mounting cell and coupled to a prism using an index matching fluid (R.I.=1.72). The input sources are then connected to pressure driven fluid reservoirs using plastic tubing (0.01 inch diameter, Tygon®). Due to gas permeable properties of PDMS, the valve control lines filled with water to displace

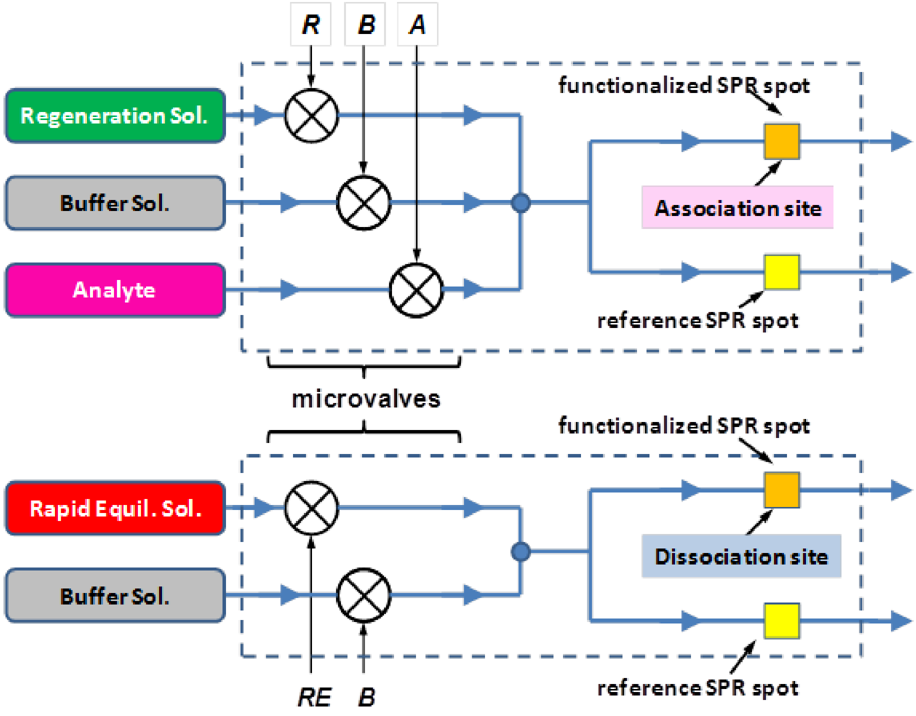

Figure 5.2. Schematic of a Dual-slope SPR chip consisting of four SPR spots and five microvalves.

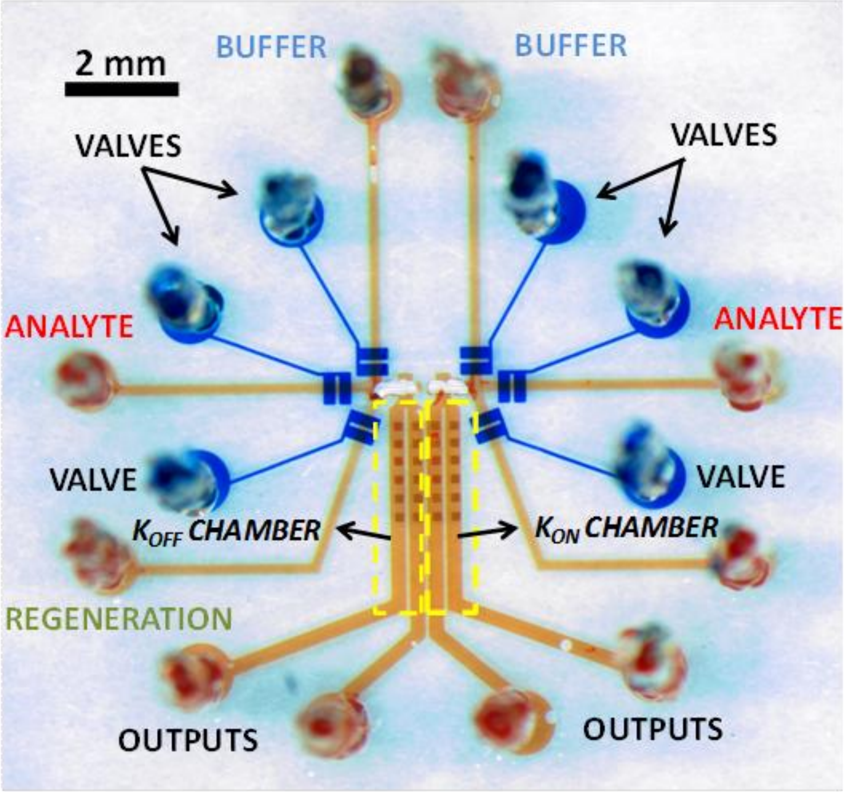

Figure 5.3. Photograph of Dual-slope SPR microchip.

air and are connected directly to pressure sources. The input reservoirs contain PBS (10 mM Phosphate, pH 7.4) as flow buffer, CA II as analyte, and 0.01% SDS as regeneration solution, respectively. The fluid flow and valve actuating pressures are 10 PSI and 25 PSI, respectively. The reservoir pressure corresponds to a flow velocity of ~16 cm/s in output channels which is sufficient to overcome mass transport effects [5]. The analyte samples are prepared by dissolving dry CA II powder in PBS followed by concentration measurement using a spectrophotometer at a wavelength of 280 nm. Reported values of extinction coefficient (a_{280}) for bovine CA II range from 55300 to 57000 L/mole-cm [6,7]. The protein concentration (*C*) is then given by the relation C (mole/L) = $A_{280}/(a_{280}.b)$, where A_{280} is the value of absorbance at 280 nm and b being optical path length (1 cm for the given photometer). The high concentration analyte ($[A_{RE}]$) solution is first prepared followed by appropiate dilution using PBS to make low concentration solution [A]. Two different concentration sets ([A] and $[A_{RE}]$) were prepared and used in experiments to calculate two sets of k_{on} and k_{off}. The analyte concentrations used to record the conventional step-response sensorgrams were used for associative half reactions on the same sensor surface. Values of analyte concentration sets {[A], $[A_{RE}]$} were {1.63, 54.4} and {3.4, 56.67} μM, respectively. The lowest allowable concentration of [A] is dictated by the background noise of the sensorgram, and the maximum concentration $[A_{RE}]$ was selected as the saturation limit of protein concentration for our spectrophotometer. The sampling rate was ~ 7.143 Hz for all data recordings. Wasabi camera control software integrated with EMCCD camera is used for data acquisition and analysis. The sensorgram intensity I(t) for sensing and reference spots (1160 pixels) for all data frames were first retrieved using the in-built software followed by further analysis using MATLAB.

5.2.2 Results

The measurement parameters S_A and S_D were obtained from linear curve fitting of the associative and dissociative sensorgrams and I_{RE} from the observed equilibrium intensity value of the rapid equilibrium sensorgram. The kinetic constants k_{on} and k_{off} for the analyte-ligand pair were then obtained from Equations 5.5 and 5.4, respectively. In all the data sets, there exists fixed imager intensity I_{offset} for all the imaging gold spots. This is first recorded at the beginning of the experiment and later on substracted from the measured signals to bring the baseline of the extracted signal to zero. The signal from the reference spots (I_{ref}) is then substracted from that of the sensor spots (I_{sensor}) to obtain reference and sensor signals for further processing. The reference-sensor spot pairs are approximately at the same distance downstream from the either modulators and substraction of their signals ensure elimination of the signal component from bulk response of analyte.

5.2.2.1 Dual-Slope and SRM

In order to serve a basis for comparison, we first ran a conventional step-response curve of a functionalized spot within a PDMS chip. Figure 5.4 shows the step-response sensorgram for analyte concentration of 3.4 μM requiring 5 minutes of recording time. Next, using a dual-slope SPR chip, we tested the feasibility of the new technique of parameter estimation using two different sets of associative and dissociative analyte

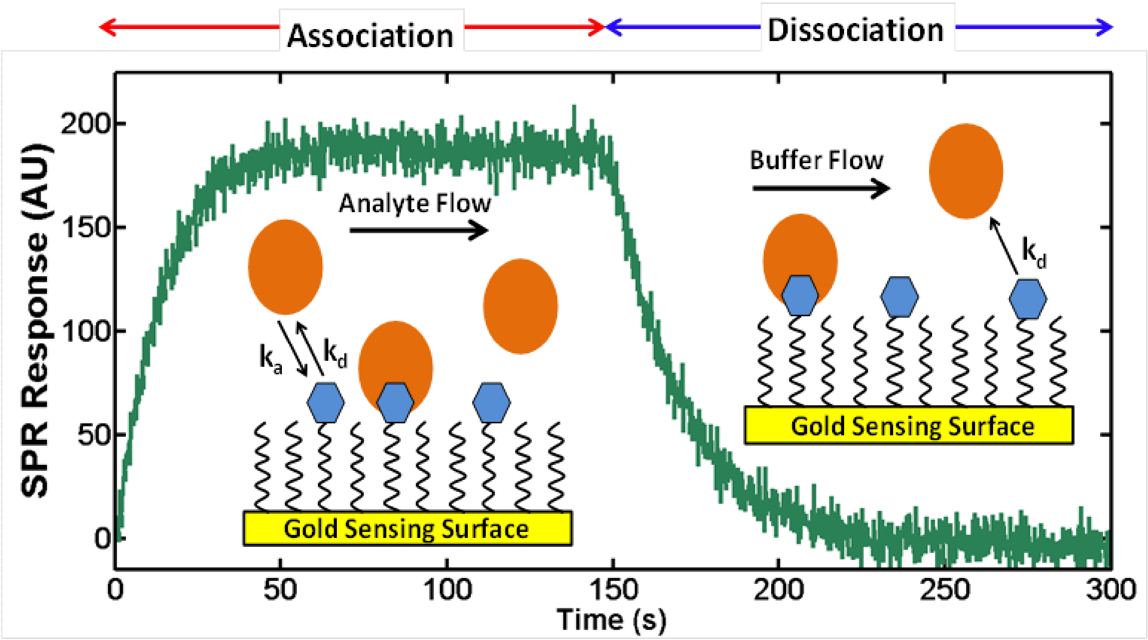

Figure 5.4. Conventional SPR step-response. The sensorgram consists of one association and one dissociation step (5 min for CAII-ABS).

concentrations. Figure 5.5 shows a sensorgram of ten half reaction cycles at analyte concentration of [A] =3.4 μM recorded from Au spots in the association chamber, indicating associative slope S_A. The time preiod for analyte, buffer, and regeneration flows are 10, 7, and 13 seconds, respectively. The flow cycle periods were adjusted to be sufficiently long as to achieve signal-to-noise ratios much greater than one; yet the cycle times were much shorter than expected exponential association and dissociation time constants. Figure 5.6 shows a sensorgram of ten dissociative half reaction cycles, indicating dissociative slope S_D for analyte concentration of $[A_{RE}]$ =56.67 μM. While predissociation saturation is allowed for 17 seconds, the dissociation is carried out for 13 seconds using buffer flow. The kinetic constants for conventional step response were calculated first by exponential curve fitting of sensorgrams using the method of least squares. The results are summarized in Table 5.1. The rates reported were averaged over 10 cycles. The rates are in good agreement with previously reported values [8]. Although the off-rate estimation using method of least squares is more accurate and reproducible, the on-rate tends to vary with analyte concentration and is hence less reproducible [9]. Our studies confirm that as well. However, as indicated by our estimate using the dual-slope method, both the on and off rates appear to be more reproducible for different sets of analyte concentrations. One possible explanation for the apparent reproducibility may be the result of the short measurement of the slope technique which intrinsically has a much lower sensitivity to drift induced errors when compared to the longer conventional step response measurement. Besides, the low dispersion characteristics of the microchip and less distance between the point of switch-flow and the sensing site make it possible to remove the erroneous sensorgram signals that appear at these solvent interfaces.

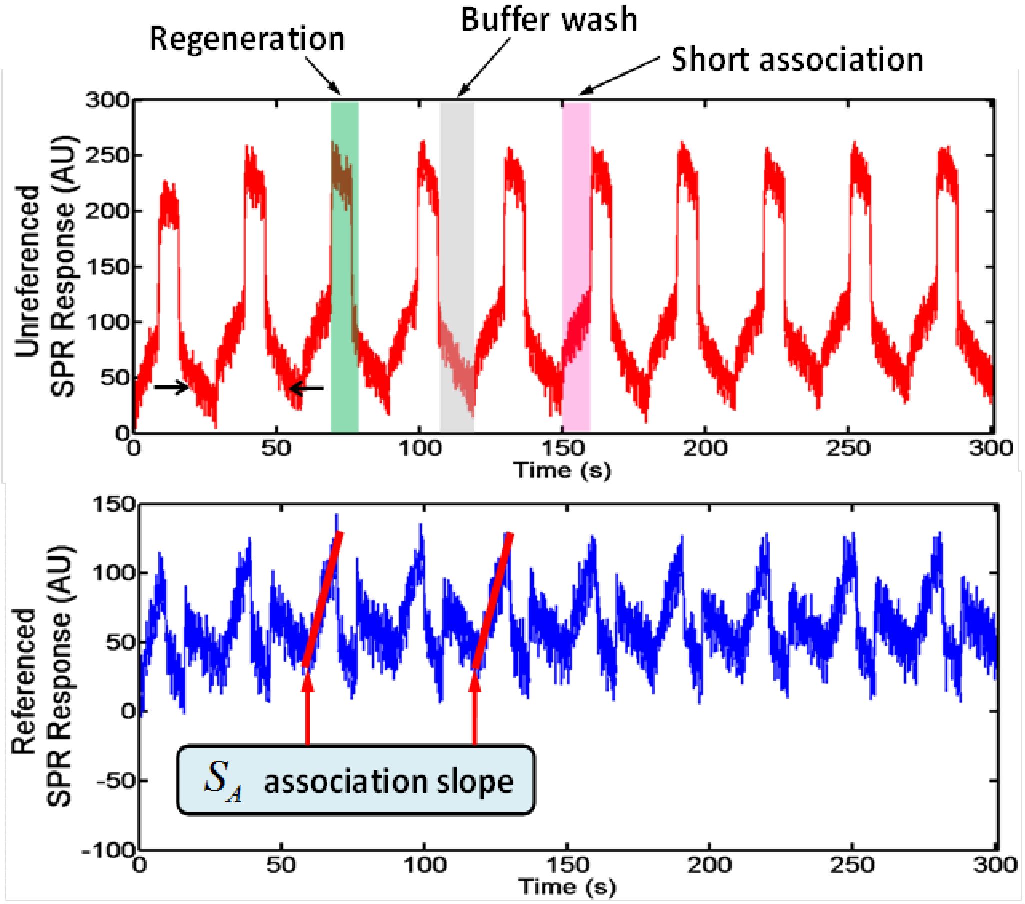

Figure 5.5. Rapid multistep measurement of association slopes for CAII-ABS. For the association slope measurement,we use a three-step buffer, analyte, and regeneration solution cycle. The top trace is unreferenced SPR trace and the bottom is referenced to a passivated spot.

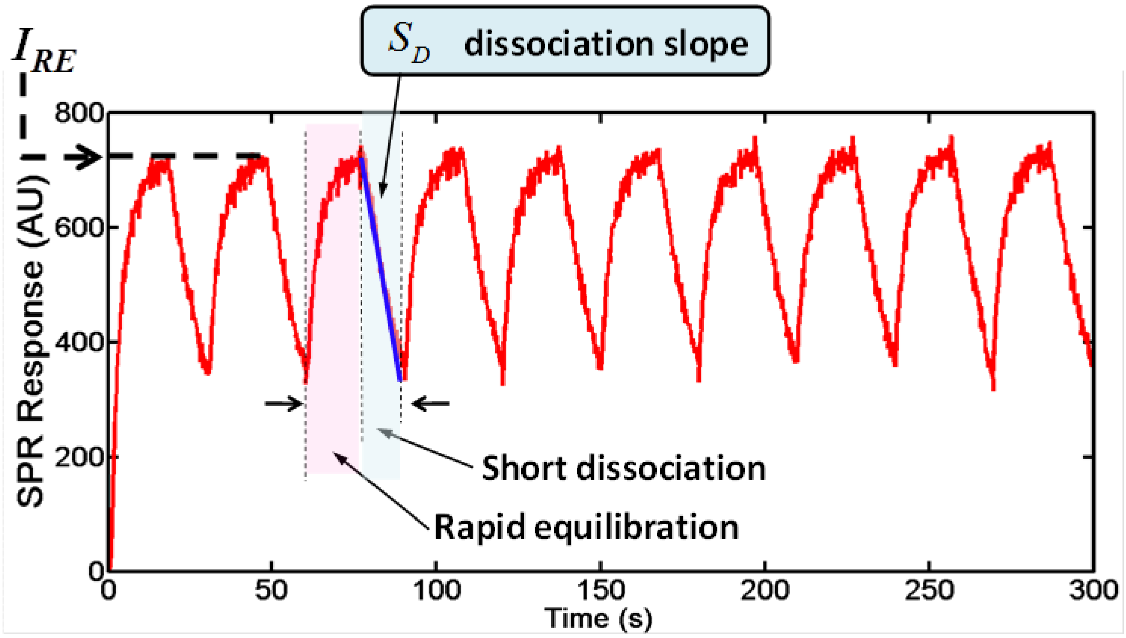

Figure 5.6. For the dissociation slope measurement, we use a two-step short rapid equilibrium and dissociation cycle. The analyte concentrations [A] and [A_{RE}] are 3.4 and 56.67 µM, respectively.

Table 5.1 Rate Constants of SRM and Dual-slope SPR

TECHNIQUE	**ANALYTE CONCENTRATION (μM)**	**KINETIC ON-RATE k_{on} ($M^{-1}s^{-1}$)**	**KINETIC OFF-RATE k_{off} (s^{-1})**
Conventional SRM	1.63	$4.75\pm0.42\times10^{3}$	$4.81\pm0.15\times10^{-2}$
	3.4	$8.68\pm0.35\times10^{3}$	$4.76\pm0.20\times10^{-2}$
Dual-slope Method	$[A]=1.63,[A_{RE}]=54.4$	$3.66\pm0.19\times10^{3}$	$4.83\pm0.17\times10^{-2}$
	$[A]=3.4$, $[A_{RE}]=56.67$	$3.60\pm0.22\times10^{3}$	$4.74\pm0.21\times10^{-2}$

5.2.2.2 SNR and Comparative Study

The experimentally observed signal-to-noise ratio or SNR for the dual slope SPR technique is about 18 dB compared to 28 dB of the step-response of Figure 5.4. The SNR was calculated as the ratio of the root-mean-square intensity of the fitted response over that of the recorded signal in the absence of any excitation. The SNR is improved when the measurement is performed over a longer period of time or averaged over many cycles because the standard deviation of random noise does not grow as much as the strength of the signal does. Therefore, for a shorter measurement period, the slope scheme yields a lower SNR. A figure of merit more useful for comparison is given by

$$\mathrm{FOM} = \frac{\mathrm{SNR}}{\sqrt{\mathrm{T_{meas}}}} \tag{5.6}$$

where T_{meas} is the total measurement time. The ratio of FOMs for the slope versus the step response measurement is approximately 1.4 when using measurement periods of 30 seconds and 5 minutes, respectively. This indicates that the FOM for the dual slope methodology is slightly better than that of the conventional step response. This technique should therefore be utilized in situations where random noise is not a limiting factor for the measurement when one can trade speed with SNR or when the noise is not random.

5.3 Discussion and Summary

While a complete on-off cycle in conventional method takes about 250~300 seconds [5,10,11], the new dual slope technique requires only 30 seconds for one cycle. While the associative cycle takes only about 10 seconds, the saturation level prior to dissociation (17 seconds in our case) can be achieved even faster using a higher concentration, hence reducing the overall time to complete the two half reactions. Besides, rate estimation using equilibrium analysis [9,11] requires association phase going to equilibrium, hence consuming time and larger volumes of bio-samples. The dual-slop technique circumvents such drawbacks. It must, however, be noted that the rapid equilibration time also depends on the value of rate constants for a particular bimolecular binding system. In our case, the detection process can be achieved ~10 times faster without compromising the quality or accuracy of rate estimation. This technique of kinetic characterization can be adopted in the instance of all high-throughput experiments of analyte-ligand binding using SPR owing to its speed and accuracy.

5.4 References

1. Ghosh, T.; Mastrangelo, C. *Analyst*, 2012, 137, 2381-2385.

2. Probstein, R.F. *Physicochemical Hydrodynamics: An Introduction*, 2nd Ed., Wiley, NY 2003.

3. Thorsen, T.; Maerkl, S. J.; Quake, S. *Science*, 2002, 239, 580-584.

4. Azizi, F.; Mastrangelo, C. *Lab on a Chip*, 2008, 8, 907-912.

5. Lahiri, J.; Isaacs, L.; Brzybowski, B.; Carbeck, J.; Whitesides, G. M. *Langmuir*, 1999, 15, 7186-7198.

6. Krishnamurthy, V. M.; Kaufman, G. K.; Urbach, A.. R.; Gitlin, I.; Gudiksen, K. L.; Weibel, D. B.; Whitesides, G. M. *Chem. Rev*., 2008, 108, 946-1051.

7. Nyman, P. O.; Lindskog, S. *Biochim. Biophys. Acta*, 1964, 85, 141-151.

8. Williams, L.; Ghosh, T.; Mastrangelo, C. *Anal. Chem.,* 2010, 82, 6025-6031.

9. O'Shannessy, D. J.; Bringham-Burke, M.; Soneson, K. K.; Hensley, P.; Brooks, I. *Anal. Biochem*., 1993, 212, 457-468.

10. Myszka, D. G. *Anal. Biochem*., 2004, 329, 316-323.

11. Corr, M.; Slanetz, A. E.; Boyd, L. F.; Jelonak, M. T.; Khilko, S.; Al-Ramadi, B. K.; Kim, Y. S.; Maher, S. E.; Bothwell, A. L. M.; Marguiles, D. H. *Science*, 1994, 265, 946-949.

CHAPTER 6

METHOD 4: PLUG-TRAIN SPR

6.1 Introduction and Theory

In this chapter, we discuss the theory and implementation of a low consumption scheme called plug-train SPR using singulated plug approach. We start with background followed by the schematics of this method. Next we introduce a new strategy for hydrophobic modification of PDMS channel walls needed to implement such an approach. In the results section, we will test the plug-train technique using this SPR microchip. We next compare the results with those obtained from other schemes from previous chapters. Finally, we conclude the chapter with a discussion where we will look into the accuracy and viability of this method.

6.1.1 Low Sample Consumption Scheme

As discussed in section 1.4.1.2, another pitfall of SRM is the bio-sample consumption due to continuous flow conditions of sensing. In the case of SRM and also other schemes [1,2,3], a substantial volume of bio-samples ranging from a few microliters (μL) to a few milliliters (mL) are consumed in one experimental run, increasing the reagent costs as well. If the reagent switching technique can be manipulated to transfer optimal volume to

Certain portions of the text and all figures and tables in this chapter are reproduced [translated] from the article “A droplet-based novel approach for viable and low consumption surface plasmon resonance bio-sensing inside a polydimethylsiloxane microchip”, Ghosh, T.; Xie, Y.; Matrangelo, C. Biomicrofluidics, 7, 044122, Copyright 2013, American Institute of Physics.

the sensing zone, the volume requirements of the experiment can be reduced manifold.

This extends to conventional SRM as well where the precise volume and time of the bio-reaction can be controlled by the user. Smaller volumes of analyte (in the order of nano-liters) when passed over the sensing zone need a faster detection scheme to support such a scheme. Thus, the dual-slope method of kinetic characterization we have introduced in previous sections can also be used in a flow switching scheme where the volumes of reagents consumed in the reaction and the biosensing time is reduced. In the following section, we present such a scheme of SPR detection.

6.1.1.1 Droplet-Train SPR

While continuous flow of sample is needed to eliminate transport limited reactions, in many of these cases, the sample consumption can be reduced by confinement of sample into droplets or plugs. Using short discrete solution plugs while employing conventional SRM for extracting reaction constants is potentially a fast and inexpensive technique for label-free high throughput analysis, provided the speed of droplet transport is high enough to overcome diffusion-limited reaction. Recently, it was demonstrated [4-6] that by manipulation of the flow switching method, singulated drug plugs separated by an immiscible oil phase can be can be synthesized and transferred to surface immobilized cells for bio-reaction. Therefore, this suggests that a similar technique could be used to separate plugs while delivering different compounds to a SPR sensing surface. However, while cells might be compatible with oil, the nature of surface chemistry in our case of SPR sensing is delicate and might not be compatible. Besides, the ligand molecules are immobilized on a hydrophilic layer (monolayer or 3-D matrix) that is anchored to the gold transducer surface. The presence of such a hydrophilic brush can be a source of inconsistent SPR sensorgram during the passage of plugs of separate phases. In addition, the physical effect of hydrophobic molecules on this brush is unknown.

One way of circumventing this problem is the use of air as the inert gas phase for plug separation. Under switch flow conditions where discrete reactant droplets are isolated by air and transported to SPR sensing sites, we can meet the goal of reduction in sample consumption. The reaction kinetic constants can be extracted either by conventional SRM or dual-slope method. We call such a scheme a Droplet-Train SPR method. As we shall see later, the accuracy and viability of the scheme cannot be validated unless we look into the physical phenomenon at the sensor surface during SPR sensing and explain it from the findings of Jennissen et al. [7].

6.1.2 Principles of Measurement

Figure 6.1 shows the basic principle of plug-train technique. Unlike other SPR schemes, solution samples are first loaded as discrete plugs separated by an immiscible inert phase. In our chip, we use an inert gas as the separating phase as the delicate chemistry of the functionalized SPR surface might be adversely affected by oil exposure. When these plugs are transported to the Au sensing functionalized spot, brief association and dissociation reactions occur for analyte and buffer plugs, respectively. The alternate air and solution plugs are transported sequentially over the gold spots to the output storage reservoir. As we shall see, these plug volumes range between 80-200 nano-liters (nL). Kinetic constants are then measured using conventional step response curve fitting of observed sensorgrams [8-10].

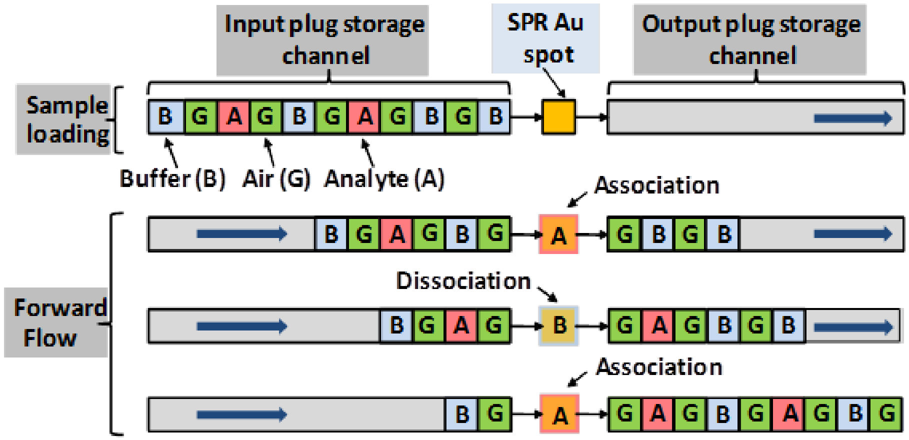

Figure 6.1. Basic principle of plug-train SPR microchip scheme. The chip consists of two channel reservoirs where analyte and buffer are separated into plugs by an immiscible inert phase (air). Plugs are first loaded in the input reservoir followed by transport in the forward phase, where association and dissociation cycles are measured with all plugs ending at the output reservoir.

The use of air as the inert separation phase, however, requires additional considerations as compared to all other SPR microchips we have used so far. Since PDMS is gas permeable, an impermeable thin layer of a coat material that remains adhered to the walls permanently is necessary to prevent alternate air plugs from collapsing. It also requires being hydrophobic. Since air is hydrophobic, it prefers to stick to a hydrophobic surface. Therefore, the channel wall surfaces of the reaction flow cell has to be modified to make it permanently hydrophobic and impermeable so that alternate plugs of the reagents that are synthesized and flown are discrete and disconnected from each other. This is also because studies [7] have shown that a discretized plug system with alternate air bubbles or short air plugs retain a thin layer of solvent on an otherwise hydrophilic wall surface which can also be a potential source of collapse of air plugs and hinder discretization. Besides, discretization is also crucial from the standpoint of being able to control the volume of plug delivered eventually to the SPR sensor surface. We will use amorphous fluoropolymer Teflon (Teflon AF) resin as this coating material.

In addition to above, the implementation of the chip requires preserving the bare gold spots from contamination of reagents, especially prior to the formation of hydrophilic PEG brush with an underlying small PEG molecule. This is primarily because the hydrophilic brush formation on the sensory gold surface is necessary for functionalization and also for avoiding spurious nonspecific signals from the gold surface. Since the sensory functionalization is carried out only after all other modification steps inside the microchip, the hydrophobic coating procedure of microchannels with Teflon AF needs to incorporate modification steps that protect the gold surface during the coating and then de-protect it when the coating is complete.

A plug-train of alternating plugs of Figure 6.1 is synthesized by simply opening the microfluidic valve that controls the flow through the channels from the reservoir source for a certain prechosen time period while keeping all other valves closed. A solvent plug (analyte or buffer) is introduced in the input channel in an alternating manner with air plugs.

6.1.3 Schematics of Measurement

Figure 6.2 shows the schematic of a plug-train SPR Microchip implementing a dual (sense + reference) chamber arrangement. Each of its chambers has four pressure driven load sources connected to buffer, analyte, regeneration, and a heterogeneous separation phase (air), respectively, and two outputs, all connected to flow channels. Flow of each of these solution sources is controlled by a set of microvalves. The chip microchannels are lined with functionalized SPR sensing and reference spots in order to record sensorgrams. Figure 6.3 shows a photograph of a plug-train microchip. This microchip is fabricated using a modified two-level PDMS technique [11-13]. In the next section, we will discuss how a methodology of protecting and then de-protecting the bare gold spots is employed during the hydrophobic modification of the walls of microchannels inside the fabricated chip prior to further surface modification procedures.

6.1.4 Hydrophobic Modification of Microchannels

In fabrication steps of Figure 2.1, Ti/W-Au spots are patterned on the glass substrate by conventional deposition, lithography, and etching; the photoresist S1813 covering the spots is not removed away by acetone and instead left as a protective layer. The Au-

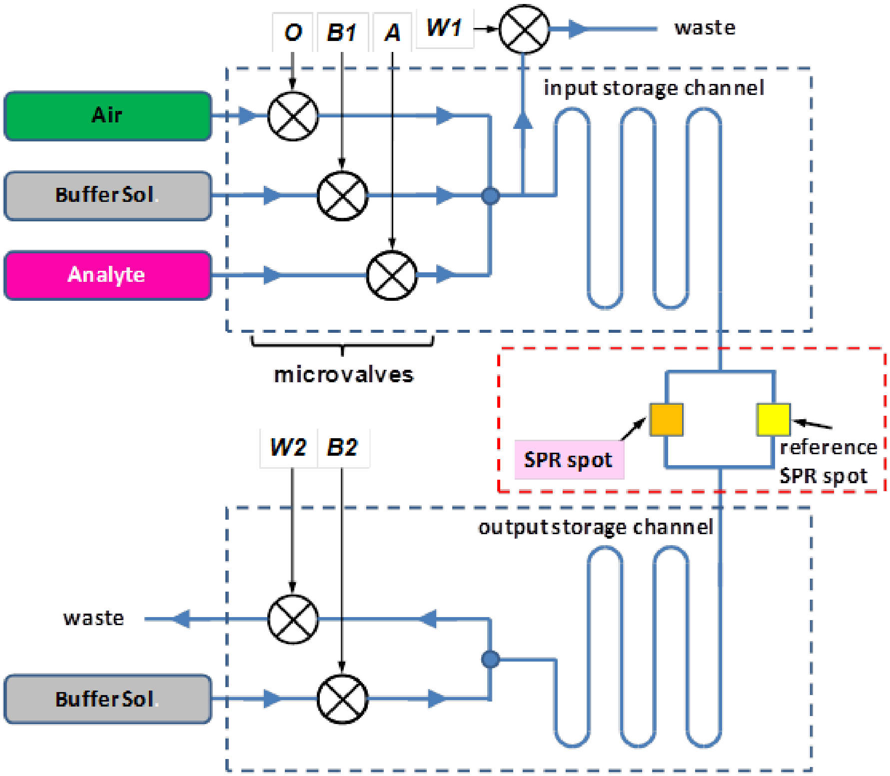

Figure 6.2. Schematics of plug-based SPR chip. Valves O, B1 and B2, and A regulate air, buffer, and analyte plugs, respectively, while valves W1 and W2 control the transport of the plug-train system to the SPR sensing channel via input storage channel.

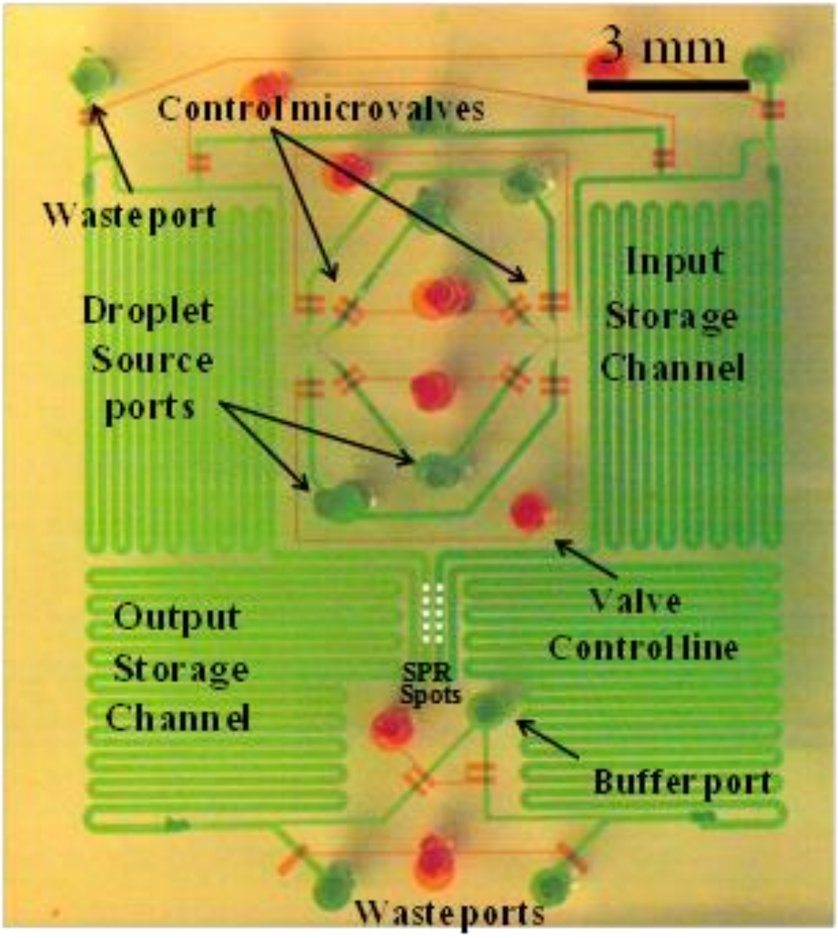

Figure 6.3. Photograph of fabricated SPR microchip. The chip measures 1.8 by 2.2 cm.

protected glass substrate is next bonded to a conventional two-level PDMS chip using an oxygen plasma step. It must be noted that the photoresist layer (~2.2 μm) on the gold spots is sufficiently high to avoid its etching and removal after the plasma etch step (oxygen plasma is performed for 20 seconds at an S1813 etch rate of ~200 nm/minute). Next, the microchannel walls are coated with a fluorination agent (Teflon-AF) that renders the channel walls permanently hydrophobic ($\theta \sim 108^{o}$). A Teflon-AF (6% resin by weight dissolved in fluorinert solvent FC-40 with glass transition temperature $T_g = 160\ ^{0}C$) solution and Fluorinert (FC-3283) dissolving solvent were purchased from DuPont™ and 3M Fluorinert™, respectively. A solution of 0.2 % Teflon-AF by volume in FC-3283 solvent is first prepared and flown inside the microchannel for 1 minute followed by removal of excess fluorinating solvent using pressure of 20 PSI. The chip is then baked at 95^{0} C for 12 hours to complete the hydrophobic coating. The Au protective resist is next removed by acetone exposure, rinsing, and subsequent HCL cleaning. This is followed by the SPR sensing and reference spot functionalization, as discussed in surface modifications steps of section 2.1.1.4. The flow process of Figure 6.4 shows the Teflon coating steps of this microchip.

6.2 Testing of Plug-Train SPR

6.2.1 Experiments

The SPR chip of Figure 6.3 is mounted onto a cell and coupled to the prism using refractive index matching fluid. Post microfluidic connections to flow channels and valves, the valve control lines are filled with water due to displace the air with water in the valves due to gas permeable properties of PDMS. Phosphate-buffered saline (PBS,

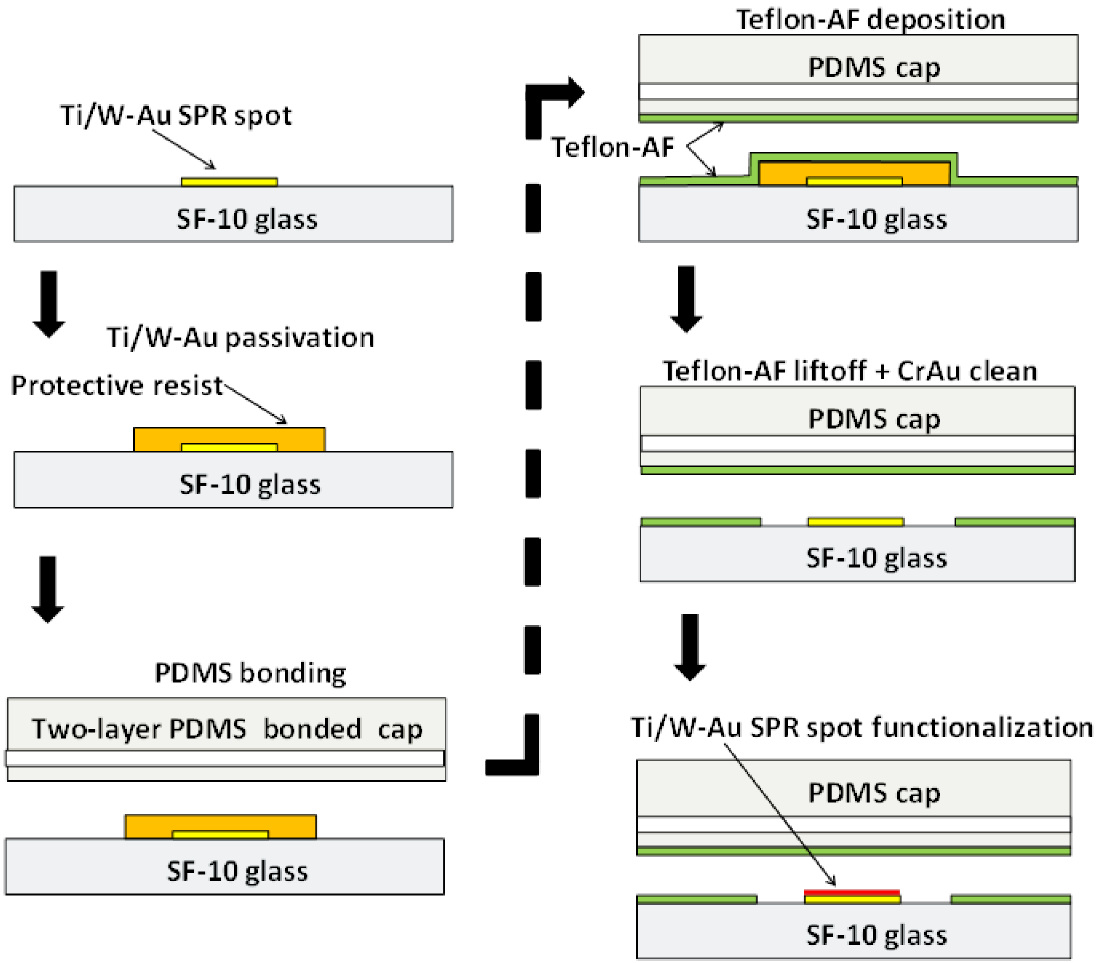

Figure 6.4. Fabrication process for coating of Teflon AF of a two-level PDMS SPR microchip. The gold spots are protected during the coating followed by release of the protective photoresist layer for further functionalization steps.

5mM sodium phosphate, pH 7.4) was used as buffer. The valves that control the air source are actuated by pressure of 9 PSI while the analyte (CA II) and buffer (PBS) are both pressurized by 10 PSI. The CA II samples were prepared using the procedures discussed in previous chapters. First, dry CA II powder was dissolved in the running buffer solution. Next, we measure the actual concentration in solution using a Spectrophotometer at a wavelength of 280 nm. The protein concentration (C) is then given by the relation C (mole/L) = $A_{280}/(a_{280}\cdot b)$, where A_{280} is the value of absorbance at 280 nm and b is optical path length (1 cm for the given photometer).

The sampling rate was kept constant at ~5.6 Hz for all the runs. Wasabi camera control software integrated with the Hamamatsu EMCCD camera was used for analyzing the collected data. The mean intensity I(t) of the sensing and reference gold spots (900 pixels) for all the frames were extracted using this software followed by its Fourier transform analysis in MATLAB. The channels were flushed with regeneration solution (0.1% SDS in running buffer) between the runs.

6.2.2 Results

The kinetic constants k_a and k_d for this analyte-ligand pair were obtained by using the conventional exponential curve fitting procedure of SRM. In all the data sets, there exists fixed imager intensity I_{offset} for all the imaging gold spots. This is first recorded at the beginning of the experiment and later on substracted from the measured signals to bring the baseline of the extracted signal to zero. The signal from the reference spots (I_{ref}) is then substracted from that of the sensor spots (I_{sensor}) to obtain reference and sensor signals for further processing. The reference-sensor spot pairs are approximately at the same distance downstream from the either modulators and substraction of their signals ensures elimination of the signal component from bulk response of analyte. The corrected time-domain responses from the experiments then follow the simple relation $I(t) = I_0 \cdot s(t)$ where I_0 is the proportionality factor, s(t) being the test signal in analyte.

6.2.2.1 Viability of Plug-Train Method

In this chip, we first tested the feasibility of the hypothesized plug-train measurement method. Fluorescent solvent plugs with alternating air plugs were first synthesized in the chip (without SPR gold spots) which was then transported to the actual SPR sensing zone and their fluorescent intensity signal is recorded in real-time. Figure 6.5 shows an example plug train where discrete solvent plugs of fluorescent solution (Fluorescein in PBS buffer) with alternating air plugs are transported through microchannels by a driving pressure source. This plug system is then plotted in real-time as illustrated by the fluorescent intensity plot of Figure 6.6. Droplets have an approximate volume of ~110 nanoliters and plug duration of 2 seconds at a source pressure of 10 PSI (for both solvent and air plugs). While solvent plugs of duration 1 second have an observed volume of 52 ± 3 nanoliters, shorter plugs have reduced reproducibility and higher standard deviation. The upper limit of plug volume is, however, determined by the maximum volume permissible in the input storage channels of this fabricated devise. The total volume of the fluidic channel system in this storage chamber is about 730 nanoliters. Generally speaking, optimal parameters for the devise of given dimensions and measurement technique is an input plug ranging from 400~600 nanoliters at flow rate of 10 PSI or higher. The air plugs can range from 2~4 seconds depending on the number of analytes

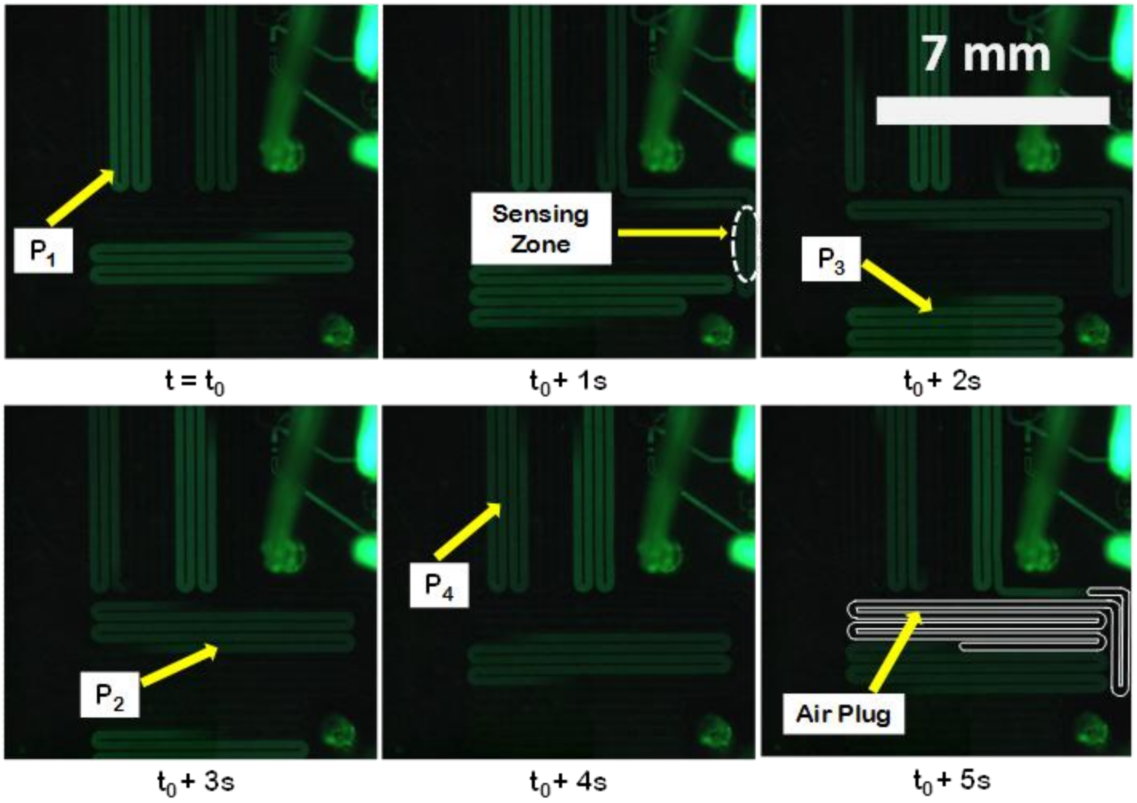

$t = t_0$ $t_0 + 1s$ $t_0 + 2s$

$t_0 + 3s$ $t_0 + 4s$ $t_0 + 5s$

Figure 6.5. Snapshots of alternating solvent plugs in green ($P_{1\text{-}4}$ in sequence from point of injection) and air plugs (dark regions between solvent plugs) transported inside the chip (flow direction from left to right in input channel via sensing zone to the output channel downwards). The images are obtained from a fluorescent microscope.

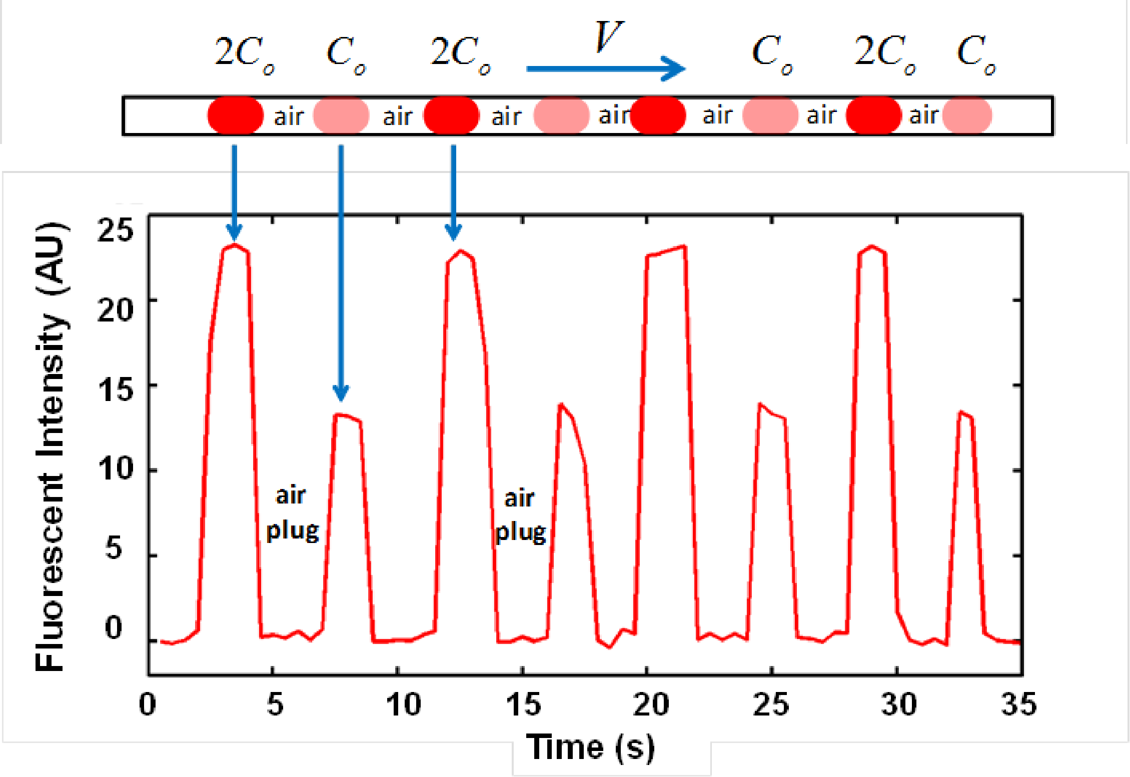

Figure 6.6. Recorded fluorescence intensity plot from a spot of 900 pixels in the sensing zone of the chip. Plugs of two different concentrations (C_0 and $2C_0$) of fluorescein alternated by air plugs are flown at constant pressure of 10 PSI and average flow velocity V.

and total input chamber volume.

6.2.2.2 Kinetic Characterization

Next, we tested the characterization of the biochemical reaction using functionalized sensor and passivated reference gold spots in a SPR chip. Analyte concentrations of 1.2, 3.1, and 4.6 μM were used for the analyte plugs in separate plug-train experiments. PBS buffer was chosen for the buffer plugs. Figure 6.7 (right) shows a time-domain SPR sensorgram obtained from the sense and reference gold spots for a flow of alternating analyte and buffer plugs (solvent plugs have a volume of ~480 nanoliters) separated by an air plug at a flow pressure of 15 PSI. Table 6.1 shows a comparison of the kinetic constant value obtained by all these reported SPR characterization techniques. While these estimation values vary for different sensing surfaces, we compare the kinetic constants from different techniques for same protocol of gold functionalization.

6.3 Discussion

While one can argue that PDMS is hydrophobic and might not require any further modification, the use of PEG reagents in SPR functionalization steps has been observed to reduce the wetting angle. This is probably due to the physical adsorption of hydrophilic thiol-terminated PEGs on PDMS surface. In the case of chips without Teflon modification, the air plugs sandwiched between two solvent plugs can diminish in volume as the combined plug system is driven by pressure through the channels to the point where the two solvent plugs can coalesce and move together as a combined plug.

This is primarily due to gas permeable properties of PDMS. As Figures 6.6 and 6.7

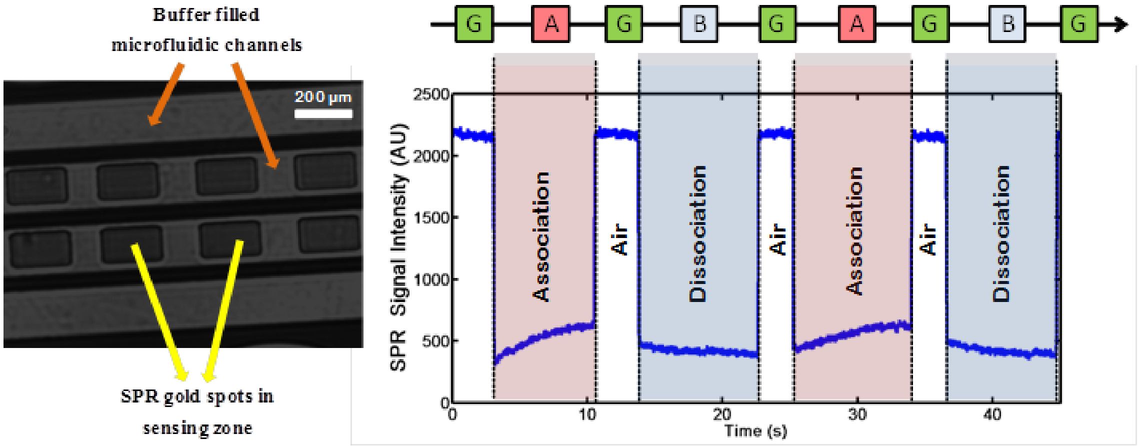

Figure 6.7. Image of the sensing zone in activated surface plasmon mode (left); the two separate channels are dedicated to sensing and control spots which are placed in proximity of each other [2] (left), and time-domain plug-based SPR sensorgram extracted from the analysis of sequence of images like one to the left (right). Two cycles of alternating analyte and buffer plugs (8 s) with an air plug in between (3 s) are synthesized and transported. Corresponding association and dissociation for the CAII-ABS biochemical interaction system are recorded from a gold spot for analyte concentaruion of 3.1 µM. The final referenced data set has been baselined to 300 for the figure.

Table 6.1 Comparison of Rate Constants of Different SPR schemes

TECHNIQUE	**ANALYTE CONCENTRATION (µM)**	**KINETIC ON-RATE k_{on} ($M^{-1}s^{-1}$)**	**KINETIC OFF-RATE k_{off} (s^{-1})**
Conventional SRM [2,14]	1.63	4.75×10^{3}	4.81×10^{-2}
	3.4	8.6×10^{3}	4.76×10^{-2}
Multisine Method [3]	5.2, 10.4 and 15.6	9.5×10^{3} (Average value)	6.2×10^{-2} (Average value)
Dual-Slope Method [2]	[A ; A_{RE}] = [1.63 ; 54.4]	3.66×10^{3}	4.83×10^{-2}
	[A ; A_{RE}] = [3.4 ; 56.67]	3.60×10^{3}	4.74×10^{-2}
Plug-Train Method[17]	1.2	8.33×10^{3}	4.58×10^{-2}
	3.1	7.83×10^{3}	4.13×10^{-2}
	4.6	9.08×10^{3}	5.36×10^{-2}

indicate, however, notable or inconsistent volume reduction of air plugs do not occur throughout the transport process in the modified devices. Since air is hydrophobic, it has a stronger affinity for more hydrophobic surfaces and hence, this Teflon coat on PDMS might therefore aid in withholding discretization requirements while transporting plugs.

Figure 6.7 shows another interesting observation. Since air (R.I. = 1) has much less R.I. than buffer (R.I. = 1.33), the SPR signal intensity for air plugs must be less than that of buffer and correspond to the baseline value instead of the peak value in the real-time sensorgram [15]. As observed, a quantifiable SPR value within the dynamic range of our

EMCCD capture device leads us to believe that due to unconventionally high R.I. change from buffer to air and vice versa, the SPR resonance conditions undergo a reduction of angle of resonance (θ_r) in a manner that the SPR signal around buffer conditions (on the left of initial resonance dip curve at a fixed θ_r of our SPR imaging system) changes for air plugs and now corresponds to the intensity from the right side of the shifted resonance curve.

Finally, in order to validate the feasibility of such a singulated plug approach, we need to account for the effect it has on the observed kinetics of the bio-reaction. Although continuous flow conditions with a flow velocity (V of Figure 6.6) higher than a threshold value [14,16] ensures that the reaction involving the macromolecule is not diffusion limited, a switched flow condition incorporated with air plugs might affect this mass transport and alter the reaction kinetics. As mentioned earlier, Jennissen et al. [7] demonstrated that for a flow of air bubbles alternating with solvent plugs, a stationary or slow-moving nanofilm of liquid (~200 nm thickness from the wall boundary) is retained on a hydrophilic sensing surface. This liquid film is metastable and the analyte replenishment occurs through “vortex flow” mechanism upholding the exponential kinetics. Such flow mechanism rather improves the mass transport rate by drastically reducing the Nernst diffusion layer thickness and eliminating the mass transport limitations of the bio-reaction [7]. Since our sensing gold surface bears a highly hydrophilic dense brush of PEG, it must retain such a solvent nanofilm that upholds the bio-reaction kinetics during plug-train transportation. The SPR intensity for air plugs of Figure 6.7 is then a combined effect of this nanofilm and the overlying layer of air for another ~100 nm [15].

6.4 Summary

We demonstrated a novel droplet-based SPR sensing inside a microchip. In this chip, solution plugs of few hundred nanoliters or less can be synthesized and singulated by an inert, immiscible gas phase to form a short solvent stream in place of a long continuous one. The device is well-suited for multi-analyte and high throughput drug screening systems where the sample consumption and reagent cost are important. Using plug-train SPR method, one can characterize an SPR bio-reaction with acceptable accuracy and manifold reduction of bio-sample volumes as compared to the conventional. It also eliminates the effects of dispersive mixing that might be a source of error in parameter estimation. On a concluding note, the numerical technique for the conventional SPR bio-sensing used in this characterization analysis is based on method of least squares [18] which has been reported to be less reproducible [2,18]. While in this work we introduce the concept of droplet-based SPR characterization, more accurate and reproducible measurements would require SPR microchips that are tailored for more complex dual-slope type SPR measurement method.

6.5 References

1. Giancoli, D. In. *Physics for Scientists and Engineers*, Prentice-Hall: New Jersey, 1989.

2. Ghosh, T.; Mastrangelo, C. *Analyst*, 2012, 137, 2381-2385.

3. Ghosh, T.; Williams, L.; Mastrangelo, C. *Lab on a Chip*, 2011, 11, 4194-4199.

4. Chen, D.; Du, W.; Liu, Y.; Liu, W.; Kuznestov, A.; Mendez, F. E.; Philipson, L. H.; Ismagilov, R. F. *Proc. Natl. Acad. Sci.*, 2008, 105, 16843-16848.

5. Liu, Y.; Ismagilov, R. F. *Langmuir*, 2009, 25, 2854-2859.

6. Roach, L. S.; Song, H.; Ismagilov, R. F. *Anal. Chem.*, 2005, 77, 785-796.

7. Jennissen, H. P.; Zumbrink, T. *Biosens. Bioelectron.*, 2004, 19, 987-997.

8. Löfas, S.; Johnsson, B. *J. Chem. Soc*; *Chem. Commun.*, 1990, 21, 1526-1528.

9. Fagerstam, L. G.; Frostell-Karlsson, A.; Karlsson, R.; Persson, B.; Ronnberg, I. *J. Chromatogr.,* 1992, 597, 397-410.

10. O'Shannessy, D. J.; Bringham-Burke, M.; Soneson, K. K.; Hensley, P.; Brooks, I. *Anal. Biochem.*, 1993, 212, 457-468.

11. Thorsen, T.; Maerkl, S. J.; Quake, S. *Science,* 2002, 239, 580-584.

12. Azizi, F.; Mastrangelo, C. *Lab on a Chip*, 2008, 8, 907-912.

13. Chen, L.; Azizi, F.; Mastrangelo, C. *Lab on a Chip*, 2007, 7, 850-855.

14. Williams, L.; Ghosh, T.; Mastrangelo, C. *Anal. Chem.*, 2010, 82, 6025-6031.

15. Schasfoort, R. B. M.; Tudos, A. J. *Handbook of Surface Plasmon Resonance*; Royal Society of Chemistry, Cambridge, 2008.

16. Lahiri, J.; Isaacs, L.; Brzybowski, B.; Carbeck, J.; Whitesides, G. M. *Langmuir*, 1999, 15, 7186-7198.

17. Ghosh, T.; Xie, Y.; Mastrangelo, C. *Biomicrofluidics*, 2013, 7, 044122.

18. O'Shannessy, D. J.; Bringham-Burke, M.; Soneson, K. K.; Hensley, P.; Brooks, I. Anal. Biochem., 1993, 212, 457-468.

CHAPTER 7

CONCLUSION

As we arrive at the conclusive phase of this research work, we realize that the signal processing methods, their conceptualization, and implementation were eventually aimed at improving methods of kinetic characterization for what we broadly identify as macromolecular interactions of biological interest and otherwise. To give this research work a structure and basis, we have broken down the implementation strategy into several but discrete modules; SPR instrumentation, microfabrication technology for SPR biochips, and the bridging bio-chemistry and associated surface modification methods being the most important ones. While we have had a comprehensive discussion to each individual scheme and methodology in previous chapters, in this chapter, we will look beyond this work and try and conclude their ramifications on a broader scale and its future scope.

First, we discuss a critical aspect of all the experiments conducted for various SPR methods, the observed kinetic constants. Since the biochemical functionalization steps that have enabled the subsequent characterization of binding kinetics are the same irrespective of SPR measurement method, we need to analyze the effects of mass-transport, the diffusive versus convective considerations, and the possible influence of lateral interactions during the binding events on the sensor surface. This would give us a good idea of whether the measured constants are reflective of true kinetics.

7.1 Observed Kinetic Rate Constants

7.1.1 Continuous Flow

The two SLFT-SPR methods and the Dual-slope SPR methods fall in the category of continuous flow systems with a finite flow velocity through rectangular channels under the application of a finite flow pressure. In this section, we calculate the depletion zone and compare the diffusive versus convective fluxes to give us an estimate of whether our binding kinetics is mass-transport or reaction limited. Let us first have a look into the diffusion boundary layer.

7.1.1.1 Diffusive Depletion Layer δ

Typically in sensors, the target molecules (protein CA-II in our case) with a finite coefficient of diffusion D diffuse through the solution and reach the sensor surface. As a result, a depleted zone is formed with a thickness given by

$$\delta(t) = \sqrt{D \cdot t} \tag{7.1}$$

where $\delta(t)$ is time-dependent length of the depletion layer over the sensor surface that grows radially and indefinitely spanning the channel dimensions [1]. As this layer grows, diffusive flux of target molecules gets slower, impeding its collection by sensor. Convection, where the target molecules are moving with the flow velocity of the solution, somewhat stops this $\delta(t)$ from growing indefinitely by providing a steady flux of target molecules due to convection. As a result, a steady state depletion layer δ_s is formed. A ratio of the diffusive to the convective time, also denoted by Peclet number Pe_H

(references [25-27] of original reference [1]), gives us an idea of the mass-transport regime the sensor is operating in. Pe_H is given by the relation

$$Pe_H = \frac{\text{Diffusive Time}}{\text{Convective Time}} = \frac{Q}{D \cdot W} \tag{7.2}$$

where Q is the flow rate of the target molecules (Q = u.W.H) and u, W, and H are flow velocity, microchannel width, and height, respectively. For $Pe_H << 1$, diffusive flux trumps the convective flux, resulting in a diffusion-limited reaction with the depletion zone propagating indefinitely. Whereas for $Pe_H >> 1$, we have a steady state depletion layer δ_s, where the target molecules within this layer are captured by the sensor while the rest are swept away by convection [1]. In the case of our microsensor, the values of u, W, H, and D are 0.1 m/s, 200 μm, 20 μm, and 1×10^{-10} m^2/s, respectively, giving us Pe_H value of 2×10^4. This number is sufficiently large to ensure that we are not operating in a diffusion-limited regime of mass transport. With the above values, we can also estimate the length of our δ_s to approximately be around 1.6 μm, sufficiently less than the sensor length of 200 μm.

7.1.1.2 Reaction Rates and the Surface

A steady state depletion layer alone does not nullify the effects of mass-transport especially through the boundary layer to the surface or its bearing on the observed rate constants. We also need to analyze whether our kinetics is indeed reaction-limited or mass-transport limited by considering the concentration of target molecules c_0 and surface density of immobilized ligand b_m. Let us first define the kinetic rates. Assuming first-order Langmuir kinetics, the equilibrium dissociation constant K_D is given by the relation

$$K_D = \frac{k_{off}}{k_{on}} \tag{7.3}$$

where k_{on} and k_{off} are first-order observed kinetic on and off rates, respectively. For concentrated solutions ($c_0 >> K_D$), sensor surface is saturated by the target whereas $c_0 \leq K_D$ implies only a fraction of immobilized ligands are target bound. We have used concentrations of the target protein ranging in μM with observed $K_D \sim 10^{-5}$ M. Hence, we have a situation where only a fraction of surface receptors capture the target and we need to look further into the reactive flux at the surface to find whether these observed values are indicative of true kinetics.

Given the dense brush of functionalization-group-bearing PEG molecules that is grafted on the sensor surface for ligand immobilization [2] and consistent with values reported by authors [1,3], the surface density of ligands (b_m) in our case is assumed to be 10^{15} molecules/m^2 or more. The mass-transport flux within the depletion layer is given by

$$J_D \sim \frac{D \cdot (c_o - c_s) \cdot L \cdot W_S}{\delta_s} \tag{7.4}$$

where c_s, W_s, and L are surface concentration of target, sensor width, and length, respectively, and the initial reactive flux is given by

$$J_R \sim k_{on} \cdot c_s \cdot b_m \cdot L \cdot W_S \tag{7.5}$$

For our case where $Pe_S \sim L/\delta_s >> 1$ [1], a ratio of the two fluxes is given by an expression called Damkohler number

$$D_a = \frac{k_{on} \cdot \delta_s \cdot b_m}{D} \tag{7.6}$$

For our system where the kinetic on-rate is in the order on 10^3, this value turns out to be in the order of 10^{-3}. This means that $D_a << 1$ which according to authors [1,3] implies that our kinetics is indeed reaction-limited. In other words, the observed kinetics is also the true kinetics. However, since the initial reactive flux is proportional to the concentration ($c_s \sim c_o$), the on-rate tends to decrease with increase in time periods of reaction as compared to a less dense surface coverage of ligands [3]. This is primarily attributed to the effects of lateral interactions [3] between closely packed target molecules on surface which are subject to effects of steric hindrance and complications involving binding, unbinding, and then rebinding of target molecules to adjacent ligands. This might also be the reason why in the case of dual-slope SPR measurement (conducted for 10 times or more shorter periods), we have more accurate measurements, particularly for the on-rates.

While our measured values of on-rate are indeed in the same order with those measured previously [3], the off-rates are an order higher that the same report. While this can be attributed to a different chain length of both the presenting PEG molecule and the para-substituted group of the benzenesulfonamide ligand used, the value of the on-rate still being in the same order indicates that our surface density of ligands might be very high to induce repeated and rapid binding and unbinding and other more complex phenomenon that is happening on the surface. Therefore, the fact that the binding is reaction-limited (as indicated by calculations) is not entirely true as there are other effects that supplement the true kinetics. Generally speaking, the secondary reactions rates due to conformational changes of the protein on the sensor surface has also been left out of our assumption and derivation of rate constants, which further complicates the process of linking the observed rate estimation to the true kinetic measurements.

7.1.2 Singulated Plug Flow

In this kind of fluid flow inside the sensor cell, we have a situation where the target bearing and plain buffer solutions are separated and discretized by an immiscible air phase. These two solutions are alternated and transported over our SPR sensor surface yielding corresponding association and dissociation sensorgrams. The rate constants are then extracted from exponential fitting with the assumption of first-order Langmuir kinetics. While the flow velocity of plugs is in the same range as our previous experiments and measurements, from the above calculations, our reaction is not mass-tranport limited (through the diffusion layer) and the observed kinetics are expected to be the similar. Although the measured rate constants tell us a similar story as well, we would like to have a look at the diffusion layer from the perspective of Jennissen et al. [4].

The boundary layer which has been calculated to be around 1.6 μm for our previous cases now correspond to about 200~300 nm which reduces the effects of mass-tranport even further. This liquid nanofilm which is metastable replenishes the target molecules onto the surface by what has been described as a 'vortex flow' [4]. This kind of effect results in virtual absence of target depletion. The exponential kinetics persists for a time longer that the passage of air bubbles.

Since, in our case, the air bubble passes for a time shorter than both the fluid flow (both association and dissociation phases) and the assumed persistence time of 20~50 s [4], this might explain the higher spread in the kinetic off-rate values for the three different concentrations (see Table 6.1) as compared to the conventional SRM method used in all the exponentially fitted measurements. A plausible reason is that the kinetics is persisting beyond our assumed experimental times of only the association and dissociation flow phases. The anomalies that arise from the noninclusion of the air bubble flow times in exponential fitting and rate-estimation steps in our opinion somewhat makes the measured values less consistent and accurate.

7.2 Conclusive Remarks and Future Scope

7.2.1 Frequency Domain Signal-Locking SPR Schemes

The prime goal of introducing signal processing schemes that utilize frequency domain analysis was to introduce signal-to-noise (SNR) higher than the conventional step-response method (SRM). Frequency domain schemes were separated into large- and small-signal SLFT-SPR analysis and the improvements and drawbacks offered by the schemes have been discussed in detail in Chapters 3 and 4, respectively. In the following subsections, we will discuss the schemes and their improvements briefly. The benefits they might offer to related but dissimilar biosensing applications are also mentioned.

7.2.1.1 Large-Signal SLFT-SPR: Spectral Sweeping

While this scheme has been demonstrated to offer a 78% (100-fold) improvement in SNR compared to conventional SRM, it comes at the expense of 24-fold longer detection time. A 100-fold improvement, however, points to the fact that detection resolution has increased, offering a potential solution to more fine bio-molecular interactions. Nevertheless, these frequency-domain studies have utilized microfluidic channel dedicated to reference and unreferenced SPR sensing units enabled by the advancements in microfabrication technology. Hence, our implementation starategies are cleaner and more immune to dispersion issues that are common to the commercial SPR flow-cells otherwise. The SLFT schemes and the SPR technology itself are universal and therefore applicable to bio-interactions that involves all other class of bio-molecules and clinically relevant analytes.

7.2.1.2 Small-Signal SLFT-SPR: Multisine

Following the drawbacks of large signal sweeping scheme, efforts were made to improve the detection time of frequency domain schemes. The multisine scheme offered similar detection times while improving SNR by approximately 28%. The trade-off though comes in the form of complexity. It is interesting to note that for clinically critical interactions where complexity is less relevant, small-signal SLFT-SPR is the signal processing scheme of choice for kinetic characterization of bio-molecular interactions.

There is, however, another interesting thing to note. The multisine chip uses multi-plug-modulator (MPM) units that synthesize an analog concentration signal from a binary digital one. For physiological chemical signals that have their own characteristic waveforms, e.g., β–cell intracellular cytosolic Ca^{2+} oscillations, SPR chips using such MPMs can also find use in a viable and label-free study of such unique biological signals and corresponding cellular responses.

7.2.2 Other Schemes

We will lump the Dual-slope and Plug-Train SPR schemes in this section and discuss the drawbacks of conventional SRM they have aimed and addressed. In following individual subsections, we will talk about their implications and future scope.

7.2.2.1 Dual-slope SPR

This measurement scheme was aimed at improving the detection and characterization time of a bio-chemical interaction. The acquired data from testing the concept of dual-slope schematics showed a 10-fold faster method that is also more accurate than SRM. Although the SNR dropped by 35% for the method, the figure-of-merit (see Chapter 5) showed a 40% improvement. For interactions where time rather than SNR is of priority, like high-throughput screening, this is a method that is potentially implementable at a larger scale for screening and characterizing without compromising accuracy.

7.2.2.2 Plug-train SPR

Plug-train SPR scheme was introduced with the aim of reducing the bio-sample consumption in interaction and characterization studies from the order of µL and mL to the order of nL. The tailored SPR microchip could separate and discretize sample plugs into droplets and transport them though the microchannels without dispersion between adjacent plugs. This scheme is the first of its kind in label-free studies. While the goal is kinetic characterization of a protein-small molecule pair, it can be employed for droplet based cellular and other biological studies as well.

7.3 References

1. Squires, T. M.; Messinger,R. J.; Manalis, S. R. *Nature. Biotech*., 2008, 26, 417-426.

2. Uchida, K., Otsuka, H., Kaneko, M., Kataoka, K. & Nagasaki, Y. *Anal. Chem*., 2005, 77, 1075-1080.

3. Lahiri, J.; Isaacs, L.; Brzybowski, B.; Carbeck, J.; Whitesides, G. M. *Langmuir*, 1999, 15, 7186-7198.

4. Jennissen, H. P.; Zumbrink, T. *Biosens. Bioelectron*., 2004, 19, 987-997.

APPENDIX

DERIVATION OF AMPLITUDES OF COMPLEX FOURIER SERIES

We determine the first components of the complex Fourier series of Equation (3.8) for two limiting conditions as T→∞ (ω→0) and T→0 (ω→∞) while replacing the exponentials with simplified first term expansions. When T→0, the exponential solution becomes a plain square wave of frequency f_φ with corresponding first (or fundamental) complex Fourier series coefficients

$$C_1^{\infty}=\frac{1}{T}\int_0^{T/2} a\cdot e^{-j\frac{2\pi t}{T}}dt=-j\frac{a}{\pi},\quad C_{-1}^{\infty}=\frac{1}{T}\int_0^{T/2} a\cdot e^{+j\frac{2\pi t}{T}}dt=+j\frac{a}{\pi} \tag{1}$$

The first component of the complex Fourier series as T→∞ is

$$c_1^{\infty}(t)=-\frac{ja}{\pi}e^{j\frac{2\pi t}{T}}+\frac{ja}{\pi}e^{-j\frac{2\pi t}{T}}=\frac{2a}{\pi}\sin\left(\frac{2\pi t}{T}\right)=c_1^{\infty}\cdot\sin\left(\frac{2\pi t}{T}\right) \tag{2}$$

The amplitude $c_1^{\alpha} = 2a/\pi$ of the sinusoidal component will be used later on to find the magnitude of the transfer function. For the case when T→0, the complex Fourier coefficients at the fundamental are

$$C_{-1}^{0}=\frac{1}{T}\int_0^{T/2} a\left(1-\left[\frac{1-e^{-\beta_1}}{1-e^{-(\beta_1+\beta_2)}}\right]\cdot e^{-\alpha_1 t}\right)\cdot e^{+j\frac{2\pi t}{T}}dt+\frac{1}{T}\int_{T/2}^{T} a\left(1-\left[\frac{\left(1-e^{-\beta_1}\right)\cdot e^{-\beta_1}}{1-e^{-(\beta_1+\beta_2)}}\right]\right)\cdot e^{-\alpha_2(t-\frac{T}{2})}\cdot e^{+j\frac{2\pi t}{T}}dt \tag{3}$$

$$C_1^0=\frac{1}{T}\int_0^{T/2} a\left(1-\left[\frac{1-e^{-\beta_1}}{1-e^{-(\beta_1+\beta_2)}}\right]\cdot e^{-\alpha_1 t}\right)\cdot e^{-j\frac{2\pi t}{T}}dt+\frac{1}{T}\int_{T/2}^{T} a\left(1-\left[\frac{\left(1-e^{-\beta_1}\right)\cdot e^{-\beta_1}}{1-e^{-(\beta_1+\beta_2)}}\right]\right)\times e^{-\alpha_2(t-\frac{T}{2})}\cdot e^{-j\frac{2\pi t}{T}}dt \tag{4}$$

Taking the limit of Equations (3) and (4) as T→0, we obtain

$$C_{-1}^0=C_1^0=-\frac{\alpha_1\alpha_2 aT}{(\alpha_1+\alpha_2)\pi^2} \tag{5}$$

and the fundamental component of the complex Fourier series is

$$c_1^0(t)=-\frac{\alpha_1\alpha_2 aT}{(\alpha_1+\alpha_2)\pi^2}\cdot e^{j\frac{2\pi t}{T}}-\frac{\alpha_1\alpha_2 aT}{(\alpha_1+\alpha_2)\pi^2}\cdot e^{-j\frac{2\pi t}{T}}=-\frac{2\alpha_1\alpha_2 aT}{(\alpha_1+\alpha_2)\pi^2}\cos\left(\frac{2\pi t}{T}\right)=c_1^0\cos\left(\frac{2\pi t}{T}\right) \tag{6}$$

Therefore, the cosine amplitude at the fundamental is

$$c_1^0=-\frac{2\alpha_1\alpha_2 aT}{(\alpha_1+\alpha_2)\pi^2} \tag{7}$$